ISSN 1580-2949
UDK 669+666+678+53 MTAEC9, 43(3)111–176(2009)

MATER. TEHNOL.	LETNIK VOLUME 43	ŠTEV. NO. 3	STR. P. 111–176	LJUBLJANA SLOVENIJA	MAY–JUNE 2009

VSEBINA – CONTENTS

UDK 54:504
Review article/Pregledni članek

ISSN 1580-2949
MTAEC9, 43(3)113(2009)

ENVIRONMENTAL CATALYSIS FROM NANO- TO MACRO-SCALE

OKOLJSKA KATALIZA OD NANO- DO MAKROVELIKOSTI

Adrián Manuel Tavares da Silva

Laboratório de Catálise e Materiais (LCM), Laboratório Associado LSRE/LCM, Departamento de Engenharia Química, Faculdade de Engenharia, Universidade do Porto, Rua Dr. Roberto Frias, 4200-465 Porto, Portugal
adrian@fe.up.pt

Prejem rokopisa – received: 2008-09-25; sprejem za objavo – accepted for publication: 2009-03-31

In today's highly sensitive ecosystem, environmental protection is a great challenge to be faced by industry, with regulations becoming more restrictive in the future. Advanced oxidation processes (AOPs) – or technologies (AOTs) – are promising end-line solutions for waste water treatment, involving liquid-phase oxidation of pollutants by means of highly reactive species, such as hydroxyl radicals. In general, installation costs of AOPs are comparable with the ones associated to biological treatments; however, operating costs of AOPs are higher due to the use of costly chemicals. Development of highly active heterogeneous catalysts is a key approach to scale-up cost-effective environmental technologies, minimizing the needs in chemicals and increasing the level of treatment obtained. This paper is an overview of some different steps involved in the field of environmental catalysis engineering to develop suitable materials from a nano-scale point to a macro-scale application.

Keywords: environmental protection; heterogeneous catalysts; advanced oxidation processes (AOPs);

V današnjem občutljivem ekosistemu je varovanje okolja pomemben izziv, ki ga srečuje industrija, še posebej zaradi predpisov, ki bodo v prihodnosti še bolj omejujoči. Napredni oksidacijski procesi (AOP) in tehnologije (AOT) so obetajoče končne rešitve za obdelavo odpadnih voda in temeljijo na oksidaciji nečistoč z visoko reaktivnimi snovmi, kot so hidroksilni radikali.V splošnem so stroški AOP-naprav podobni tistim za biološko obdelavo, vendar so obratovalni stroški AOP višji zaradi uporabe dragih kemikalij. Razvoj visokoaktivne heterogene katalize je ključni pogoj za napredek cenovno učinkovite okoljske tehnologije, ker minimizira porabo kemikalij in poveča kakovost obdelave. Ta članek je pregled različnih stopenj na področja inženirstva okoljske katalize, ki ima za cilj razviti primerne materiale z nano- do makroobmočjem uporabe.

Ključne besede: varovanje okolja, heterogena kataliza, napredni oksidacijski procesi (AOP)

1 INTRODUCTION

The treatment of effluents is one of the major social, economical and political problems of our days. As consequence, many researchers have focused their scientific interests in environmental issues. Scientific journals with high impact factors, as well as traditional and new congresses include now environmental themes. This was a crucial step in order to alert industry stakeholders to the importance of reducing the industrial impact on the environment, assuring a good quality of life. The objective of the so-called *green chemistry* is mainly directed to emerging technologies by designing environmentally benign processes [1]. However, operation issues, deep research, long time consuming and high economical investment are some shortcomings found at industrial level when applying this concept to processes already installed in traditional industries. Consequently, the treatment of pollutants by remedial end-line technologies is still important.

Conventional biological processes have associated significant disadvantages, such as inhibition of microorganisms by certain pollutants, impossibility to treat high concentrations of organic compounds and production of sludge, which is another source of pollution. AOPs are alternatives in this domain. In brief, the Fenton process consists in the chemical oxidation of pollutants by means of hydrogen peroxide (H_2O_2) and iron acting as catalyst, based in the Fenton reaction known for over 100 years [2]; ozonation is based in the strong oxidant properties of ozone; photocatalysis uses the photonic activation of the catalyst by light irradiation producing reactive electron-holes; and in catalytic wet oxidation (CWO) the pollutant molecules are oxidized with pure oxygen or air at elevated temperatures (130–250 °C) and pressures (5–50 bar). Other AOPs such as sonolysis, which consists on the ultrasonically induced acoustic cavitation, or the electrochemical oxidation, which produces large amounts of hydroxyl radicals directly in water, are at an earlier stage of development. Each technology requires a different catalytic material as well as the optimization of their catalytic properties. Different metal oxides (e.g., Zn, Mn, Fe, Co, Ni, Cr, and Bi oxides) and noble metals (e.g., Ru, Pt, Pd, Rh and Ir) supported typically on CeO_2, Al_2O_3, ZrO_2, TiO_2 or carbon materials have been used in CWO studies [3,4] and few of them applied in ozonation [5]. TiO_2-based materials are the preferred photocatalysts [6] and iron ions are the base of the Fenton reaction [7,8].

Actually, the sustainable technological implementation of AOPs as new solutions at the macro-scale depends on the understanding of fundamental catalytic processes taking place at the nano-scale. Development of active, selective and economic catalysts, which permit to

increase the process efficiency and decrease the consumption of chemicals, is one of the main challenges [9]. The present paper does not intend to give an extensive survey on the published work regarding catalytic materials and reactor configurations that has been used in AOPs, since this information can be found in many reviews of the Fenton process [8,10], ozonation [5], photocatalysis [10–15] and CWO [3,4,10,16–23], but rather to give an introductory background on the catalysis engineering steps and tools to develop heterogeneous catalysts, with the final aim of applying these materials in industrial-scale reactors. In contrast with CWO, the ozonation and the Fenton processes are relatively simple and have been widely installed for the treatment of effluents [5,7]. Photocatalysis differs from the other AOPs since a light-irradiation is used and, as consequence, the main concepts involved are also different when. Therefore, in this paper, particular emphasis is given to CWO and photocatalysis as two examples of AOPs with different complexity.

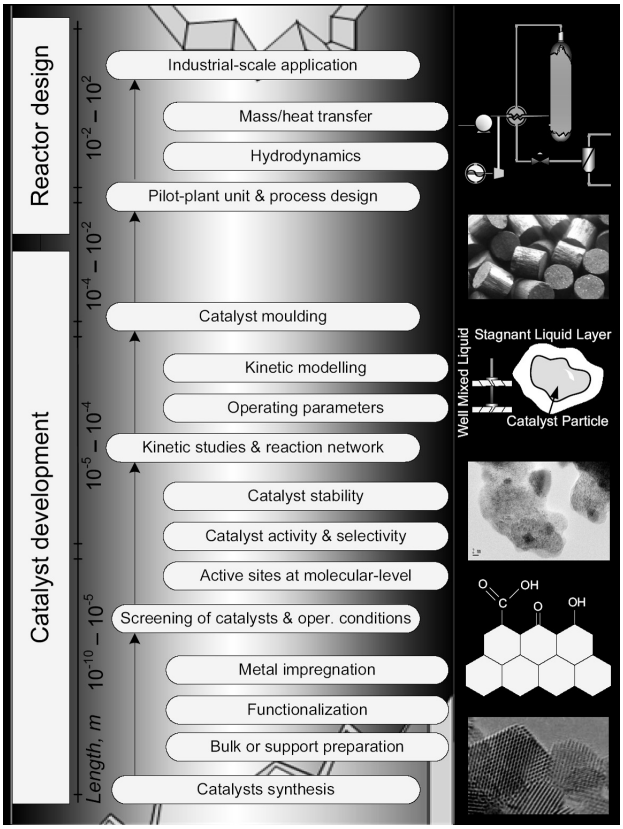

Figure 1: Schematic diagram representing different levels of catalyst development and application. Figures at the right side from bottom to top: (i) HRTEM micrograph of nanosized ceria particles (≈ 3 to 8 nm); (ii) representation of a functionalized carbon surface; (iii) HRTEM micrograph of Pt nanoparticles (dark spots ≈ 2–4 nm) supported on Ce-Ti-O; (iv) scheme of a particle of catalyst in a liquid media; (v) example of a shaped catalyst (6.4 × 6.4) mm; (vi) WO Zimpro diagram.

Slika 1: Shematični grafikon, ki predstavlja različne stopnje razvoja in uporabe katalizatorjev. Slike od desne spodaj navzgor: (i) HRTEM-mikroposnetek nanoziranih delcev cerijevega oksida (≈ 3 – 8 nm); (ii) funkcionalizirana površina ogljika; (iii) HRTEM-posnetek nanodelcev Pt (temne točke ≈ 2 – 4 nm) na Ce-Ti-O-podlagi; (IV) shema delca katalizatorja v tekočem mediju; (V) primer oblikovanega katalizatorja (6.4 × 6.4) nm; (VI) WO Zimpro-diagram

Environmental catalysis engineering can be considered as an interdisciplinary integration of fundamental and applied knowledge on materials, chemistry, physics and engineering. The different levels of catalyst development are strongly linked with basic concepts of all these areas and they cannot be isolated if the aim is to produce sustainable development of catalytic reactors. In a catalytic point of view, at the nano-scale the reactivity of the active sites is influenced by the surrounding environment at a supramolecular level. This environment drives the local adsorption/desorption of reactants and products; for instance, local pH around the active site can be different from the bulk pH depending on the characteristics of the catalytic cavities. For this reason, adequate tuning of catalysts at the nano-scale scale level allows enhancement of the catalytic properties. The nano-scale differs from the molecular level since the later refers to the direct interaction between the active site and these molecules. The nano-sized catalytic materials should be assembled at the micro-scale with the aim of obtaining optimal spatial distribution and catalyst composition in a final macro-structured catalyst (e.g., pellets, membranes, monoliths, foams) [24]. Optimization of catalytic properties and reactor design involves testing and modelling at different levels (reaction and kinetic studies under different operating conditions, mass/heat transfer and hydrodynamic investigations, simulation and experimental work in pilot-units and final scale-up to industrial level). In order to provide an integrative point of view, the multidisciplinary strategy for development of catalysts was divided in seven main stages, as shown in **Figure 1**: catalyst synthesis; catalyst screening and operating conditions; kinetic studies and reaction network; catalyst moulding; pilot-plant unit and process design; industrial-scale application. The length associated to each step is only indicative and although they are sequentially presented and described in the next sections, in practice there are overlaps between the different steps when optimizing catalytic materials/processes.

2 CATALYST SYNTHESIS

In general, the chemical processes can be classified according to the number and type of phases (liquid, gas and solid) or to the nature of the catalyst (heterogeneous or homogeneous). Gas-liquid reactions with solid catalysts are one of the largest chemical commercial applications, including oxidations, since the use of homogeneous catalysts requires its removal from the wastewater with a posterior recovery step. The concept of heterogeneous catalysts is normally associated to solids or mixtures of solids which accelerate chemical fluid reactions without changes in the solids. During

many years (essentially until 1970's), development and preparation of heterogeneous catalysts was considered more as alchemy than science, consuming many efforts, money and time without guaranty of the final results [25]. Nowadays, the relation between catalysis and other emerging sciences, such as analytical or solid state chemistry, makes possible to reduce the wide number of variables in preparing heterogeneous catalysts to a series of elementary steps. A heterogeneous catalyst is characterized mainly by the relative amounts of different components (active species, physical and/or chemical promoters, and supports), shape and size, pore volume and distribution, and surface area. The nature of the active species is always the most important factor. Various research projects worldwide investigate possible applications of active and stable heterogeneous catalysts in AOPs for the oxidation of various pollutants.

The first steps in heterogeneous catalytic ozonation date back to 1970s [26], but only now interesting perspectives are reappearing [5]. In the Fenton process the formation of sludge, a source of pollution and the reason of catalyst loss, is the main shortcoming of using iron in the typical homogeneous form. Iron-based heterogeneous catalysts, or solid sources of iron, such as minerals, are some alternatives [8]. Attention has been also paid to new heterogeneous catalysts for CWO and photocatalysis. Catalysts able to oxidize typical refractory end products of biological processes have been well accepted.

According to the most common preparation procedures, the catalysts can be classified as [25]: *bulk catalysts or supports* where the catalyst is generated as a new solid phase (e.g., precipitation, sol-gel) and *impregnated catalysts* where the active phase is introduced or fixed on a pre-existing solid (e.g., impregnation, ion exchange, adsorption, deposition-precipitation and chemical- or physical-vapour deposition). The formation and *precipitation* of a crystalline solid occurs by supersaturation with physical (e.g., variations in temperature) or chemical (e.g., addition of bases or acids) perturbations of a solution, formation of stable small particles by nucleation and growth by agglomeration of those particles. The *sol-gel* method consists on the transformation of a solution into a hydrated solid precursor (hydrogel). This method has gained importance due to the better control of different properties such as texture and homogeneity. *Impregnation* is based in the contact between the solid support and a certain volume of solution, which contains the precursor of the active phase. The method is called *wet impregnation* when an excess of solution is used and *incipient wetness impregnation* if the volume is equal or slightly less than the pore volume of the support. The *ion exchange* method is based on the replacement of ions on the surface of a support by electrostatic interactions. *Adsorption* consists in the controlled attraction of a precursor contained in an aqueous solution by charged sites on the support. In the *deposition-precipitation* method, slurries are formed and the precipitation occurs in interaction with a support surface by addition of an alkali solution. The prepared solids are separated from the mother liquor with filtration, decantation, centrifugation, etc., usually washed with distilled water (or specific organic solvents) for complete removal of impurities and submitted to thermal treatments (e.g., *drying* and *calcination-heating*). After calcination, modification of the nature and/or structure of the phases and stabilization of mechanical properties occur.

Thorough chemical, textural and structural analysis of catalytic materials is possible nowadays due to several available techniques. Electron microscopy constitutes a family of very powerful catalyst characterization techniques. Scanning electron microscopy (SEM), transmission electron microscopy (TEM) or high resolution TEM (HRTEM) are analytical techniques used to identify structural constitution of heterogeneous catalysts, including shape, atomic structure and dispersion of active nanoparticles supported on high surface area materials (e.g., Figure1-iii showing Pt-nanoparticles supported on Ce-Ti-O), which are key information in catalysis. When coupled with other techniques, such as energy-dispersive X-ray spectroscopy (EDXS) or selected-area electron-diffraction (SAED), catalyst composition data can be obtained in diverse phases of the sample, since it is possible to analyze selected areas at the nano-size scale. New devices have been coupled with microscopes in order to increase the analytical potentialities. For instance, the high-angle annular dark-field detector (HAADF) and the field emission gun (FEG) are appropriate to identify some metals (e.g., gold) at the nano-scale in catalytic materials. X-ray diffraction (XRD) is a common technique used to identify the structure of materials as well as to determine crystallite sizes with the Scherrer equation. X-ray photoelectron spectroscopy (XPS) is frequently used to analyze oxidation states. Textural characteristics (BET surface area, micropore, mesopore and macropore constitution) are determined from the nitrogen adsorption isotherm obtained at 77 K and using specific calculation methods such as t-method, Stoeckli and Dubinin equations. Temperature-programmed desorption (TPD) has gained special relevance in the chemical analysis of surface oxygen groups on carbon materials, since CO and CO_2 are formed and released when applying heating ramps [27]. By means of the deconvolution of the TPD spectra, it is possible to determine the amounts of the diverse surface groups (carboxylic acids; carboxylic anhydrides; lactones; phenols; carbonyl or quinones). This makes possible to finely tune the surface chemistry of functionalized carbon materials (representative image on **Figure 1-ii**) which provides a proper control of chemical reactivity. The referred techniques are only few examples among many other important methods that are used to characterize heterogeneous catalysts.

3 CATALYST SCREENING AND OPERATING CONDITIONS

In AOPs the appropriate catalyst will be the one that operating in amenable reaction conditions shows the highest level of pollutant degradation to carbon dioxide and water or to less toxic/refractory compounds. Many parameters should be evaluated and several materials and compositions must be tested in order to increase the probability of identifying a suitable candidate for the process. Catalyst deactivation must be investigated as well, being normally due to sintering, poisoning of active sites, dissolution of active components to the liquid phase (leaching) or fouling of the catalyst surface as a result of deposition of reaction intermediates. Examination of fresh and used catalysts allows to identify possible changes on the catalyst during the reaction, essential for understanding the catalyst deactivation. Therefore, an initial idea of catalyst activity/stability may be obtained in batch reactor experiments by recycling the catalyst for a small number of cycles. Experiments that are more definitive may require operation with a continuous reactor over hundreds or possibly thousands of hours of operation. The level of pollutants degradation to be achieved with a certain technology is defined by process economic considerations, where the cost of the catalyst replacement is considered as part of the global economical analysis. Novel methods have been developed for monitoring *in situ* in which way the metal sites interact chemically with the surrounding molecules, interconnecting classical studies with advanced analysis of the chemical events taking place at the atomic/molecular level. Sum Frequency Generation (SFG) is one example [28].

The activity of catalysts depends on the operating conditions used. Catalyst loading, solution pH and substrate concentration/nature are variables that should be considered among all the different catalytic-AOPs. Other parameters are specific for each process. Of importance is the oxygen partial pressure and the temperature in CWO, the light intensity in photocatalysis and the ratio $Fe:H_2O_2$ in the Fenton process. The ozonation process is strongly dependent on the media pH. At low pH the direct and selective reaction of molecular ozone with pollutants occurs, while at high pH ozone is mainly decomposed in hydroxyl radicals which in turn attack the pollutants [5]. In CWO, the increase of temperature leads to a consequent increase in the oxidation rate. Regarding possible effects of oxygen partial pressure and catalyst loading, a hypothetical behaviour of the total organic carbon (TOC) conversion in a generalized reaction system at constant temperature is represented in **Figure 2**. Without catalyst and increasing the oxygen partial pressure the conversion obtained will be small if the pollutant is of difficult oxidation by non-catalytic WO. If the experiment is performed without oxygen but in the presence of a catalyst, some conversion can be achieved depending on the nature of the catalytic material. Increasing both oxygen and catalyst loading, a plateau of maximum efficiency can be observed in a region where changes in the correspondent values do not affect the global conversion. Moreover, for higher oxygen partial pressures decrease in conversion is represented as well, in order to account for the possible occurrence of over-oxidation by the catalyst, as referred in the literature [29]. At a constant oxygen partial pressure, decrease in conversion with higher amounts of catalyst represents the eventual acceleration of the *termination* step mechanism by the catalyst [30].

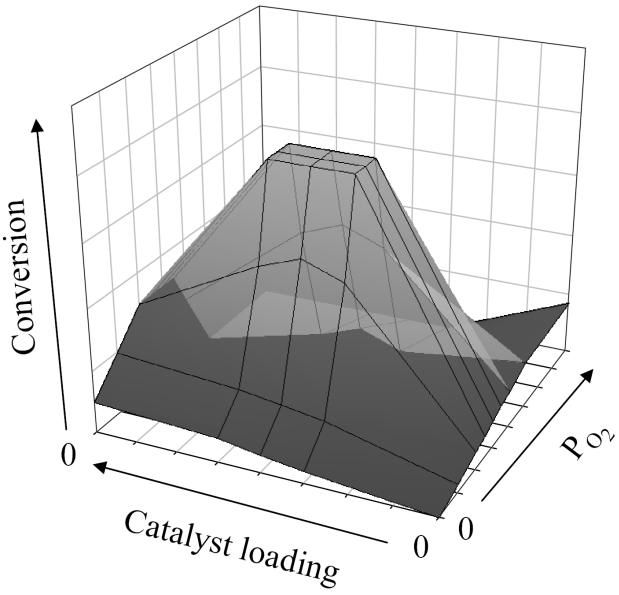

Figure 2: Conversion of total organic carbon as a function of catalyst loading and oxygen partial pressure (P_{O2}), in CWO.
Slika 2: Popolna organska konverzija na CWO kot funkcija obremenitve katalizatorja in parcialnega pritiska kisika (P_{O2})

Regarding photocatalysis, it is quite well established that the reaction rate is proportional to the radiant flux and to the mass of catalyst in slurry conditions, up to a certain loading for which all the particles are fully illuminated (usually between 0.6–2.5 g/L). For higher mass of catalyst, scattering effects can decrease the efficiency of the process [12]. In contrast to CWO, in photocatalysis heating is not required since the process is based in a photonic activation of the catalyst. In fact, increase of temperature can have a negative effect in the activity, since the adsorption of pollutants decreases and tends to decelerate the reaction. Thus, photocatalytic reactors operate at normal temperature and pressure. This advantage together with the possibility of using solar energy makes this technology very promissing. Development of immobilized photoactive materials in the visible-light region (> 400 nm) is the main challenge.

4 KINETIC STUDIES AND REACTION NETWORK

Multiphase reactions often consist of multiple reaction pathways with series of parallel reactions networks. Identification of intermediates is usually an essential

issue, normally requiring both experimental analysis and postulates from the available information. In AOPs the strong oxidation media leads to the formation of several intermediates. The difficulty in the development of a reaction network increases in complex reactions when many compounds are involved, which is of special importance when using industrial effluents. For this reason, besides Langmuir-Hinshelwood expressions, kinetic models based in lumped parameters grouping pollutants with similar reactivity have been widely used for AOPs [16,31,32]. Moreover, in general, the mechanisms are not well understood but it is quite consensual that free radicals participate actively. For this reason, the normal strategy when studying AOPs is to oxidize as much as possible the pollutants and look to the organic pollutants obtained at the end of the experiments, which are usually more resistant to oxidation than those degraded along the process.

The kinetic parameters are generally obtained in slurry operation batch-experiments for AOPs. **Figure 3** shows the typical concentration profiles of a general gas-liquid-solid system with external mass transfer and intraparticle diffusion resistances for the oxidant gas (O) and the pollutant (P). The local temperature is assumed to be constant throughout the different phases and the liquid backmixed. For the reactants the steps can be described as: (A) transport of O from the gas bulk to the gas-liquid interface; (B) transport of O from the gas-liquid interface to the liquid bulk; (C) transport of O and P from the liquid bulk to the catalyst surface; (D) intraparticle diffusion of the reactants into the catalyst pores; (E) adsorption of the reactants on the active catalyst sites; (F) surface reactions of O and P to yield reaction products; and (G) desorption of the products into the liquid bulk. Therefore, before the reaction at the active catalyst sites, different transport and reaction processes take place. In order to model the intrinsic reaction kinetics, the laboratory reactor should be selected and operated with the aim of conducting the experiments under conditions where interparticle and intraparticle concentration and temperature gradients are absent. With mechanically agitated reactors, it is possible to eliminate or reduce the magnitude of these resistances in a gas-liquid-solid catalyzed system and, therefore, it becomes easier to obtain intrinsic reaction rates directly or derived from the experimental data. Continuous fixed-bed reactors have been also used for this purpose in CWO [33]; however, elimination of these gradients may be difficult.

For slightly soluble gas oxidants in water (e.g., oxygen), the transport of the oxidant in a gas phase constituted by two or more components (e.g., oxygen and nitrogen) is faster than in the liquid. The gas phase resistance can be then neglected, being the liquid film resistance the controlling mass transfer. Different experimental procedures can be considered in order to eliminate the concentration gradients on the system; (1) For the gas-liquid mass transfer resistance the preferred approaches are to improve the gas-liquid contacting or to increase the concentration of reactant in the gas phase. The first case can be obtained by means of some reactor specifications such as impeller rotational speed, design, size, location or gas sparger design, vessel baffles and other internals; (2) Concerning the liquid-solid mass transfer resistance, the elimination of this phenomenon is associated with the amount of catalyst, catalyst particle size, impeller diameter and location, baffles and other internals. The increase of the impeller rotation speed decreases the liquid-solid resistance, having, however, little effect once the speed attains the minimum value required for complete and uniform solids suspension; (3) The internal diffusion resistance can be reduced with the amount of catalyst as well as with the particle diameter since, consequently, the effectiveness factor increases [34–35].

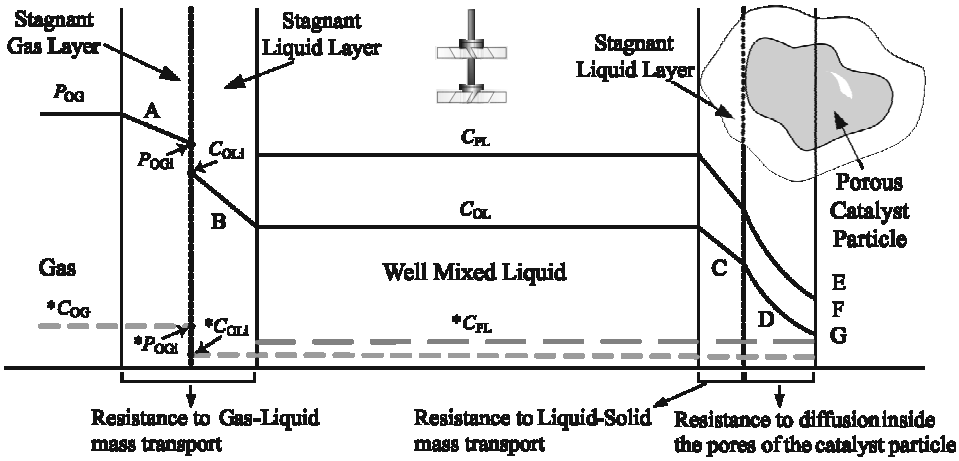

Figure 3: Schematic representation of typical concentration profiles for the gas (C_O) and the liquid pollutant (C_P) in a gas(G)-liquid(L)-solid(S) catalytic system with and without(*) external mass transfer and intraparticle diffusion resistances (i = interface).

Slika 3: Shematična predstavitev tipičnih koncentracijskih profilov za plinski (C_O) in tekoči onečiščevalec (C_P) v tekočem (L) in v trdnem katalitskem sistemu z zunanjim prenosom mase in brez njega(*) ter difuzijska odpornost med delci (1 – mejna površina)

CWO experiments are conducted in stainless steel (or titanium) high-pressure autoclaves equipped with thermocouples and mechanically driven impellers for proper control of temperature and agitation velocity, respectively. In contrast, typical batch photocatalytic reactors consist of a glass external cylindrical reaction vessel, where is placed the reaction mixture, with magnetic agitation, and an inner double-wall compartment immersed inside the liquid housing the lamp and acting as a cooling water jacket. This compartment is made of glass or quartz depending on the type of irradiation that is studied (UV or UV/VIS). Therefore, batch reactors in slurry conditions are used to perform kinetic studies in both CWO and photocatalysis. However, the reactors are quite different in what respect configuration and construction materials.

5 CATALYST MOULDING

The optimal catalyst composition defined by slurry screening tests can differs when the experiments are performed with shaped catalysts. In this context, the different steps of catalyst development should be always strongly connected. The solid catalysts are typically used as a powder (slurry), or as irregularly shaped granule, table, sphere, or extrudate. Usually, the catalysts used in slurry have average particle diameters between 50 μm to 450 μm and the larger pellet catalysts used in fluidized and fixed-bed processes between 0.8 mm to 10.0 mm (an image of a shaped catalyst is shown in Figure1-v). Structured catalysts, such as monoliths, membranes, foams and fibre catalysts are new attractive alternatives [24]. Shaped catalysts can be produced by traditional processes such as press and extraction, or using new technologies as powder injection moulding (PIM). Some studies should be done to optimize the heating rate, sintering temperature, time and atmosphere composition. In particular for photocatalysis, the use of typical pellets is not feasible since the semiconductor catalyst has to be fully irradiated. For this reason, most of the known systems use fine powdered catalyst dispersions/suspensions, requiring a final step of filtration. As solution, photocatalytic materials can be immobilized onto glass or other supports as a film. Since these coatings are still not mechanically robust for the traditional and complex waste waters treatments, they are actual motive of intensive research [13].

6 PILOT PLANT UNIT & PROCESS DESIGN

AOPs can be implemented in different three-phase reactors. Most used configurations are mechanically agitated reactors in slurry operation, bubble columns and packed-bed reactors. The complexity in modelling multiphase reactors with solid catalysts lies mainly in the fluid flow patterns, which depend on the reactor category. Prior to the intrinsic reaction that occurs at the catalyst surface, the reactants have to diffuse from the gas and liquid phase to the active catalyst sites. In this context, the scale-up of a reaction system also involves evaluation of heat and mass transfer as well as gas-liquid hydrodynamics. Several models have been developed using various parameters such as interface mass transfer coefficients, intraparticle effective diffusion coefficients, axial dispersion coefficient, flow regimes, liquid hold-up, pressure drop and catalyst wetting [23–24]. These parameters depend on the hydrodynamic regime of the reactor and the physical properties of the phases (gas, liquid and solid). Interface mass transfer coefficients or external diffusion involve the resistances that are inherent to the reactor for transport from gas to liquid, liquid to solid, gas to solid and from dynamic to static liquid. The intraparticle diffusion or internal diffusion of reactants depends on the particle shape. The flow regime describes the flow pattern of liquid and gas throughout the reactor. The liquid hold-up consists of the interparticle and intraparticle fraction, of the total reactor volume, occupied by the liquid phase. The pressure drop depends on the liquid hold-up as the latter determines the effective void fraction available for the gas phase. The catalyst wetting deals with the average fraction of the external particle surface covered by the liquid. Many studies have been conducted at laboratorial scale to consolidate the knowledge in AOPs, but the bridge between laboratory and commercial scale is still a difficult task due to this high number of variables involved in the design of multiphase catalytic reactors.

Other specific issues should be also considered. For instance, in CWO experiments, it was found that heavy polymers are formed when some pollutants, such as phenol, are oxidized in slurry reactors. This phenomenon can be attributed to the high liquid-to-solid ratio in the slurry reactor, once these polymers can be formed through oxidative coupling. Afterwards, the polymers can be irreversibly adsorbed on the catalyst surface and progressively block the active sites. In this context, reactors with low liquid-to-catalyst volumetric ratio, such as packed-beds operating in trickle-bed regime, may be better options [36,37]. Moreover, catalyst stability should be addressed in continuous reaction application, taking as base the stability results obtained in batch operation. In fact, for a fresh catalyst, it is not unusual to show an initially high level of activity during short time testing. Nevertheless, sometimes, this is followed by a gradual or rapid decline with extended exposure, which may continue until some measure of activity reaches zero, or achieves a steady-state level caused by the deactivation of the catalyst.

Most of the studies performed in continuous operation deal with small-scale reactors. Relatively few studies have been published in the field of CWO in large-scale packed-bed systems, where mass transfer limitations are involved [38]. Therefore, experimental data, description of mass- and heat-transfer processes, reactor

simulation (e.g., using Computational Fluid Dynamics – CFD) and many other studies concerning continuous operation on CWO are object of research [39,40] being tested laboratorial pilot-scale reactors with lengths between 15–350 cm and diameters between 0.1 cm and 10 cm [36,38,41,42,43].

Photocatalytic reactors differ in several aspects of design when compared with typical reactors. Selection of radiation sources (including solar light), respective design according to the radiation implemented, materials of construction and the need of other devices (such as reflectors, windows and cleaning setup) should be considered in their design [13]. Typical photocatalytic reactors consist of inner walled glasses housing the lamps in contact with the waste waters contained in an external reaction vessel. Other configurations consist of external or distributed light sources. Most of the reactors use powders as catalysts (slurry annular, open upflow, integrated flow membrane with filtration system, swirl flow, taylor vortex and turbulent slurry reactors) or, less common, immobilized photocatalysts in solid matrix (falling film, fiber optic cable, multiple tube, packed bed, rotating disk and spiral glass tube reactors). Examples of solar reactors are the parabolic trough reactor, the parabolic collecting reactor, the double skin sheet reactor, the tubular reactor and the solar pond [13].

The deposition of photoactive films on the internal surfaces of the photoreactors is gaining more importance due to the increased control on the preparation of such materials. The liquid-phase processing methods that have been used specially to synthesize thin films, usually nanocrystalline, are (co-)precipitation and sol–gel methods while among the gas phase methods sputtering, spray pyrolysis deposition, chemical and physical vapour deposition are used. More investigation is needed regarding nano-adherence stability of crystalline films when applied over a rigid inert surface and explicit application of nano-films to photocatalytic reactors. Mechanical characterization of the films can be carried out by depth-sensing nanoindentation using Atomic Force Microscopes (AFM).

7 INDUSTRIAL-SCALE APPLICATION

Examples of commercial WO processes are schematized in **Table 1** [19–20]. As it can be observed, the WO technology has earned some place in the treatment of different waste waters. In particular, Zimpro (from

Table 1: Schematization of WO commercial processes
Tabela 1: Shematika komercialnih WO-procesov

Process	N° Plants	Waste examples	Reactor	*T*/°C	*P*/bar	Catalyst
Zimpro	200 20 50	sewage sludge spent activated carbon industrial	bubble column (20 min – 4 h)	250–270 280–325 150–320	85–120 200 10–220	None (or homogeneous copper)
Kenox	n.s.	pulp & paper, metal finishing,petrochemical, food processing	recirculation reactor	204–260*	31–83	None (or impregnated in the static mixer)
Wetox	n.s.	n.s.	stirred tanks	207–247	40	None
VerTech	n.s.	sewage sludge	below-ground deep shaft	< 275*	< 110*	None
Oxyjet	n.s.	pharmaceutical and phenolic chemical wastes	jet mixer and tubular reactor (+ jet reactor)	< 300	n.s.	None (or in a jet reactor)
WPO	n.s.	n.s.	n.s. (H_2O_2 as oxidant)	90–130	1–5	Fe^{2+}
Ciba-Geiby	3	pharmaceutical, pulp & paper, petrochemical, hazardous waste landfill	n.s.	300	n.s.	Cu^{2+}
Loprox	n.s.	Paper mill waste streams, municipal sewage sludge	Single or multi-stage bubble column	120–200	50–20	Fe^{2+}
Orcan	n.s.	Textile	n.s.	120	3	Fe^{2+}
ITECP**	n.s.	n.s.	n.s.	n.s.	n.s.	Bromide, nitrate and manganese ions
Athos	n.s.	municipal and industrial sludge	n.s.	240	44	Cu^{2+} (heterogeneous optional)
Osaka gas	n.s.	coal gasifier coke ovens cyanide sewage sludge	slurry bubble column	250	70	ZrO_2 or TiO_2 with noble or base metals
NS–LC	n.s.	phenol, glucose, acetic acid, etc	monolith	220	40	Pt–Pd/ TiO_2–ZrO_2
Kurita	n.s.	spent resins, ammonia	n.s.	< 170	n.s.	Supported Pt

n.s.: not specified; *variable along the reactor; ***IT Enviroscience catalytic process.*

USFilter, U.S.) is well established at an industrial level (WO diagram shown in **Figure 1**-vi). Treatment of sludge has been one of the main applications of WO and temperature ranges from 90 °C to 300 °C and pressures up to 220-bar have been used. Different reactor configurations have been developed, such as bubble column, tubular, stirred tanks, monolith and recirculation reactors. The commercial processes are essentially based in non-catalytic WO (five systems) or in homogeneous catalysts (six processes). The use of non-catalytic systems limits the application of the technology, increases considerably the operating conditions, and, therefore, the capital costs. Only few processes (three) involving heterogeneous catalysts, which are mainly based in expensive materials (Pt and Pd) are commercially developed. Regarding the use of photocatalysis for waste waters treatment, several companies are including this technology in their commercial portfolios. Commercial worldwide interest is clear, but many photocatalytic systems are still under development. Some cases of success are the solar plant in Almeria, Spain, and the systems commercialized by Purifics Environmental Technologies Inc., Canada [13,15]. Effective immobilization of catalysts that can operates under both artificial and solar light seems to be the main challenges for sustainable development of industrial-scale photoreactors. Therefore, the development of active and stable heterogeneous catalysts for industrial-scale application became still a key factor for enhancing the efficiency of AOPs.

8 FINAL REMARKS

Several criteria should be considered when selecting a given process for the treatment of waste waters. The development of catalytic materials is based on a methodical sequence of scientific and technological approaches to achieve a successful actual application. Identification of active phases by screening reactivity tests combined with the analysis of catalyst stability are the first steps in order to proceed with further kinetices and reaction network studies, which are particular of each reactional system, and consequently, of each type of waste water. In this domain, powerful analytical tools should be used especially for catalyst characterization and deep understanding of the catalytic reaction events. The integration of different AOPs have to be considered as a common strategy in laboratorial studies since better solutions can be obtained in an efficient-economic basis regarding both capital and operating costs when scaling-up these technologies. The catalyst powders should be transformed in suitable and mechanical robust forms for mass/heat transfer investigation and, eventually, hydrodynamic studies. In this task valuable computational tools can be used to simulate the catalytic processes, such as CFD, but kinetic data can be still only obtained with experimental work. Final testing in real conditions is achieved after the scale of these technologies up to an industrial level.

Acknowledgments

The author acknowledges the *Fundação para a Ciência e Tecnologia (FCT)*, Portugal, for the financial support by the project POCI/N010/2006.

9 REFERENCES

[1] G. Centi, S. Perathoner, Catal. Today, 77 (**2003**), 287–297
[2] H. J. H. Fenton, J. Chem. Soc., 65 (**1894**), 899–910
[3] Y. I. Matatov-Meytal, M. Sheintuch, Ind. Eng. Chem. Res., 37 (**1998**), 309-326
[4] F. Stüber, J. Font, A. Fortuny, C. Bengoa, A. Eftaxias, A. Fabregat, Top. Catal., 33 (**2005**), 3–50
[5] L. F. Liotta, M. Gruttadauria, G. Di Carlo, G. Perrini, V. Librando, J. Hazard. Mater., in press
[6] X. Chen, S. M. Mao, Chem. Rev., 107 (**2007**), 2891–2959
[7] P. Bautista, A. F. Mohedano, J. A. Casas, J. A. Zazo, J. J. Rodriguez, J. Chem. Technol. Biotechnol. 83 (**2008**), 1323–1338
[8] J. Pignatello, E. Oliveros, A. MacKay; Crit. Rev. Env. Sci. Technol., 36 (**2006**), 1–84
[9] C. Comminellis, A. Kapalka, S. Malato, S.A. Parsons, I. Poulios, D. Mantzavinos, J. Chem. Technol. Biot., 83 (**2008**), 769–776
[10] S. Parsons, Advanced Oxidation Processes for Water and Wastewater Treatment, IWA Publishing, Cornwall, UK, 2004
[11] I. K. Konstantinou, T. A. Albanis, Appl. Catal. B-Environ. 49 (**2004**), 1–14
[12] J.-M. Herrmann, Top. Catal. 34 (**2005**), 49–65
[13] H. de Lasa, B. Serrano, M. Salaices (Editors). Photocatalytic Reaction Engineering, Springer Science+Business Media, USA, 2005
[14] M. Pera-Titus, V. García-Molina, M. A. Baños, J. Fiménez, S. Esplugas, Appl. Catal. B-Environ., 47 (**2004**), 219–256
[15] A. Mills, S-K. Lee, J. Photoch. Photobio. A., 152 (**2002**), 233–247
[16] J. Levec, A. Pintar, Catal. Today, 124 (**2007**), 172–184
[17] V. S. Mishra, V. V. Mahajani, J. B. Joshi, Ind. Eng. Chem. Res., 34 (**1995**), 2–48
[18] S. Imamura, Ind. Eng. Chem. Res., 38 (**1999**), 1743–1753
[19] F. Luck, Catal. Today, 53 (**1999**), 81–91
[20] S. T. Kolaczkowski, P. Plucinski, F. J. Beltran, F. J. Rivas, D. B. McLurgh, Chem. Eng. J., 73 (**1999**), 143–160
[21] S. K. Bhargava, J. Tardio, J. Prasad, K. Föger, D. B. Akolekar, S. C. Grocott, Ind. Eng. Chem. Res., 45 (**2006**), 1221–1258
[22] A. Cybulski, Ind. Eng. Chem. Res., 46 (**2007**), 4007–4033
[23] F. Larachi, Top. Catal., 33 (**2005**), 109–134
[24] G. Centi, S. Perathoner, Cattech, 7 (**2003**), 78–89.
[25] M. Campanati, G. Fornasari, A. Vaccari, Catal. Today, 77 (**2003**), 299–314
[26] C. G. Hewes, R. R. Davison, AIChE Symp. Ser. 69 (**1972**), 71
[27] J. L. Figueiredo, M. F. R. Pereira, M. M. A. Freitas, J. J. M. Órfão, Carbon, 37 (**1999**), 1379–1389
[28] G. Rupprechter, C. Weilach, Nanotoday, 2 (**2007**), 20–29
[29] Z. P.G. Masende, B.F.M. Kuster, K. J. Ptasinski, F. J. J. G. Janssen, J. H. Y. Katima, J. C. Schouten, *Catal. Today*, 79–80 (**2003**), 357–370
[30] S. S. Lin, D. J. Chang, C. Wang, C. C. Chen, Water Res., 37 (**2003**), 793–800
[31] A. M. T. Silva, R.M. Quinta-Ferreira, J. Levec, Ind. Eng. Chem. Res., 42 (**2003**), 5099–5108
[32] S. H. Lin, C. D. Kiang, Ozone-Sci. Eng., 27 (**2005**), 225–232

[33] A. Eftaxias, Catalytic wet air oxidation of phenol in a trickle bed reactor: kinetics and reactor modelling. PhD Thesis, Rovira I Virgili University, Tarragona, Spain (2002)
[34] P. L. Mills, P.A. Ramachandran, R.V. Chaudhari, Reviews in chemical engineering, Eds. N. R. Amundson, D. Luss, University of Houston, Freud Publishing House LTD, London, England (1992)
[35] H. S. Fogler, Elements of chemical reaction engineering, Ed. G. Osbourne, Prentice-Hall, London, UK (1986)
[36] J. Guo, M. Al-Dahhan, Chem. Eng. Sci., 60 (**2004**), 735–746
[37] A. Alejandre, F. Medina, X. Rodriguez, P. Salagre, Y. Cesteros, J.E. Sueiras, Appl. Catal. B-Environ., 30 (**2001**), 195–207
[38] A. Singh, K. K. Pant, K. D. P. Nigam, Chem. Eng. J., 103 (**2004**), 51–57
[39] D. Nemec, J. Levec, Chem. Eng. Sci., 60 (**2005**), 6958–6970
[40] R. J. G. Lopes, A. M. T. Silva, R. M. Quinta-Ferreira, Ind. Eng. Chem. Res., 46 (**2007**), 8380–8387
[41] A. Fortuny, C. Bengoa, J. Font, F. Castells, A. Fabregat, J. Hazard. Mater., B64 (**1999**), 181–193
[42] A. Pintar, G. Berčič, J. Levec, Chem. Eng. Sci., 52 (**1997**), 4143–4153
[43] A. Quintanilla, J. A. Casas, J. A. Zazo, A. F. Mohedano, J. Rodríguez, Appl. Catal. B-Environ., 62 (**2006**), 115–120

UDK 669.71:669.018.9:621.762.5
Original scientific article/Izvirni znanstveni članek

ISSN 1580-2949
MTAEC9, 43(3)123(2009)

PRESSURELESS SINTERING AND CHARACTERIZATION OF B_4C, TiC AND TiB_2-PARTICLE-REINFORCED $TiAl_3$-MATRIX COMPOSITES

SINTRANJE IN KARAKTERIZACIJA KOMPOZITOV NA OSNOVI $TiAl_3$, OJAČANIH Z DELCI B_4C, TiC IN TiB_2

Varužan Kevorkijan[1], Srečo Davor Škapin[2]

[1]Independent Researching plc, Betnavska cesta 6, 2000 Maribor, Slovenia
[2]Jožef Stefan Institute, Jamova 39, 1000 Ljubljana, Slovenia
varuzan.kevorkijan@siol.si

Prejem rokopisa – received: 2009-02-10; sprejem za objavo – accepted for publication: 2009-03-21

Dense (>95 % of theoretical density) $TiAl_3$-based composites reinforced with the volume fractions of B_4C or TiC 10–50 % and 10–30 % of TiB_2 particles were successfully prepared by combining pressureless reaction synthesis and reaction sintering. The first step was formation of $TiAl_3$ from the elemental powders by reaction between solid Ti and liquid Al (at 800 °C/1h and 1250 °C/3h in a static atmosphere of Ar with the volume fraction of H_2 4 %). The reaction product obtained with a nominal composition of 88% $TiAl_3$-10%Al-2 % Ti, was milled and subsequently blended with the ceramic powders. The green compacts made from the blended powder mixture were reaction sintered at 1300 °C for 2 h in an Ar + 4 % H_2-rich environment using a vacuum furnace. The morphology of the $TiAl_3$ powders and the microstructure of the as-sintered composites were studied by scanning electron microscopy and X-ray diffraction analysis. The mechanical properties were measured by tensile tests performed at room temperature. In the case of reactive systems ($TiAl_3$-B_4C and $TiAl_3$-TiC), densification proceeds via formation of various secondary bonding phases, whilst in non-reactive system ($TiAl_3$-TiB_2) the process seems to proceed by infiltration of molten aluminium into pores. In this respect, densification of $TiAl_3$-TiB_2 samples with more than 30 % of ceramic particles was incomplete. Regarding the room temperature tensile properties of the composites, superior improvement was observed in $TiAl_3$-B_4C and $TiAl_3$-TiC samples with the volume fraction of ceramic particles 50 %. However, in $TiAl_3$-TiB_2 samples the improvement was significantly lower due to the lack of chemical affinity (wetting) between ceramic reinforcement and $TiAl_3$ matrix.

Key words: aluminium titanates, reaction synthesis, intermetallic matrix composites (imcs), ceramic particulate reinforcement, reaction sintering, metallographic characterization

Z reakcijskim sintranjem smo pripravili goste (>95 % teoretične gostote) kompozitne materiale na osnovi spojine $TiAl_3$, ojačane z anorganskimi delci s prostorninskimi deleži B_4C in TiC 10–50 % ter 10–30% TiB_2. V prvi fazi smo sintetizirali spojino $TiAl_3$ iz prahov elementov Ti in Al z reakcijo med trdnim Ti in tekočim Al pri 800 °C/1h in kasnejšim segrevanjem pri 1250 °C/3h v zaščitni atmosferi Ar s 4 H_2. Tako pripravljen vzorec, ki je vseboval 88 % $TiAl_3$, 10 % Al in 2 % Ti smo zmleli ter mu primešali keramične delce v določenem razmerju in dobro homogenizirali. Te izhodne mešanice smo enoosno stisnili in sintrali v pri 1300 °C 2 uri v zaščitni atmosferi Ar/H_2. Morfologijo izhodnih delcev $TiAl_3$ in mikrostrukturo pripravljenih vzorcev smo analizirali z elektronsko vrstično mikroskopijo in energijsko disperzijsko analizo ter rentgensko praškovno difrakcijo. Mehanske lastnosti smo določali z nateznim preizkusom pri sobni temperaturi. Med sintezo vzorcev na osnovi sistemov $TiAl_3$-B_4C in $TiAl_3$-TiC je zgoščevanje potekalo s tvorbo vmesnih faz, v sistemu $TiAl_3$ – TiB_2 pa z infiltracijo tekočega Al v pore in po mejah med zrni. V vzorcih $TiAl_3$ –TiB_2 z več kot 30 % TiB_2 je bilo takšno zgoščevanje nepopolno, zato so vzorci porozni. Glede na mehanske lastnosti pripravljenih kompozitnih materialov pri sobni temepraturi kažejo največje izboljšanje le-teh materiali s prostorninskim deležem 50 % B_4C in TiC. V sistemu $TiAl_3$-TiB_2 so bile izmerjene lastnosti nekoliko slabše zaradi odsotnosti kemijske reakcije med anorganskimi delci in $TiAl_3$ matrico.

Ključne besede: aluminij titanati, reakcijska sinteza, kompoziti z intermetalno matrico, diskontinuirna ojačitev s keramičnimi delci, reakcijsko sintranje, metalografske preiskave

1 INTRODUCTION

Titanium aluminide alloys based on the equilibrium solid phases of the Ti-Al system and their composites reinforced with ceramic particles have been considered and are being developed for high-temperature applications in the automotive, aerospace, and power-generation industries. Such intermetallics based-matrix composites (IMCs) reinforced with ceramic particles generally achieved specific strength and specific stiffness, creep strength, toughness, and high-temperature strength resistance remarkably better than their as non-reinforced intermetallic counterparts [1,2]. Members of this class of advanced materials are of interest as potential high-temperature materials due to their high melting point, low density, good oxidation resistance, and high modulus of elasticity. Ultimately, bringing these attractive intermetallic materials into use largely depends upon the availability of practical processing routes.

Titanium aluminide IMCs reinforced with various ceramic particles (B_4C, TiC, TiB_2) can be effectively produced by powder processing, starting from commercial titanium aluminide powders blended with ceramic particulates [3]. Although this method offers near-net shapes with very little post-fabrication machining required, it is at the same time very expensive for

commercial application due to the high cost of titanium aluminide powders. Essentially, it is of great significance to develop an effective technique for preparation of titanium aluminide powders starting from cost-effective raw materials (e.g. by the exothermic reaction of liquid aluminium with solid titanium) and their conventional densification to fully dense alloys and composites [4]. Since such reactive synthesis and sintering aims at the formation of one or more aluminides, a prior knowledge of the formation of specific aluminide(s) and their microstructural development is particularly important for further commercialization of the process [5].

Among all the equilibrium solid phases of the Ti-Al system, only TiAl and Ti_3Al have been extensively used for alloys production and as a matrix in composites. This is because the Ti rich compounds Ti_3Al and TiAl exist over a wide range of composition while $TiAl_3$ exists as a very narrow range of compounds (an intermediate phase that appear as a vertical line in the binary phase diagram at some stoichiometric ratio of mole fractions of the elements) and any change in the definite composition of the mole fraction of elements (e.g. by oxidation) leads to its decomposition [6].

In the early stages of the development of titanium aluminide alloys and composites, the single step elemental powder metallurgical route has gained particular attention because near-net shape titanium aluminide alloy products could be fabricated by the consolidation and forming of blended Ti and Al elemental powders, followed by a subsequent reactive sintering process [7–11]. However, due to the large difference between the partial diffusion coefficients of Ti and Al, the synthesis of titanium aluminide alloys via reactive sintering follows the mechanism that Al atoms move faster into the Ti lattice then vice versa, thus leading during reactive sintering to the formation of Kirkendal diffusion pores [12–14]. Hot isostatic pressing (HIP) and refining of the Ti and Al reactants through cold deformation, such as extrusion and rolling of the Ti and Al powder mixture billet prior to reactive sintering, have been reported to be effective in eliminating the porosity of reactively sintered TiAl and Ti_3Al alloys. However, their high cost and low productivity make these techniques unsuitable for commercial use.

In the current attempt to optimize the cost and quality of IMCs, a two stage composite fabrication process was considered. The first step in composite production was the cost-effective synthesis of titanium aluminide powders from liquid aluminium and solid titanium, while the second step was the reactive sintering of the cold compacted as-received titanium aluminide powders blended with ceramic particles (B_4C, TiB_2 and TiC) to composite samples. The main expectation was that porosity due to Kirkendal diffusion could be reduced below 5 % by refining the microstructure with ceramic particulate reinforcement and by selecting from the titanium aluminides the most reactive constituents, such as $TiAl_3$.

$TiAl_3$ was found to be attractive for at least two reasons: (i) it is the main product of the reaction between liquid aluminium and solid titanium, which is one of the most economical ways of production of titanium aluminides, and (ii) it is also a reactive, non-stable phase (Daltonides) which could react with ceramic reinforcement, enabling formation of fully dense composite structures.

Hence, in the present paper we report the fabrication and characterization of titanium aluminide-based IMCs made by a pressureless two-step procedure: (i) the reactive synthesis of titanium aluminide powders with nominal composition 25Ti : 75Al by reactive synthesis from liquid aluminium and titanium powder in combination with milling and, (ii) reactive sintering of cold compacted 25Ti : 75Al powders blended with ceramic particles (B_4C, TiB_2 and TiC) to fully dense composite samples.

2 EXPERIMENTAL

$TiAl_3$ powder was synthesized by high temperature reaction synthesis from the elemental powders. As a first step, a homogeneous powder mixture of titanium (purity 99.5 % and average particle size 30 μm) and aluminium (purity 99.7 % and particle size 100 μm) with a composition corresponding to stoichiometric $TiAl_3$, 25 % mole fractions of Ti and 75 % Al, was prepared in a planetary mill. After room temperature uniaxial and cold isostatic compaction of the mixtures, the green pellets obtained were heated in a vacuum furnace (800 °C/1h and 1250 °C/3h), in a static atmosphere of Ar + 4 % H_2. This was followed by cooling the pellets to room temperature and subsequent milling of the reaction products in an attrition mill. The milling time was 4 h, and the grinding media-to-powder ratio was 2:1.

Finally, composites were formulated by blending the synthesized $TiAl_3$ powder with commercial ceramic powders (B_4C, TiC and TiB_2) in appropriate amounts to create IMC-based matrices with the volume fractions (10, 20, 30, 40 and 50) % of B_4C, TiC or TiB_2 discontinuous reinforcement.

The powder blends were thoroughly mixed in a planetary mill and subsequently cold compacted. In all cases, reaction sintering of the compacts was conducted at 1300 °C for 2 h in an Ar + 4 % H_2-rich environment using a vacuum furnace.

The as-synthesized composite samples were cut, machined and polished in accordance with standard procedures.

Microstructural characterization of titanium aluminide powders, as well as sintered composites, was performed by optical and scanning electron microscopy (OM and SEM with EDS), whereas X-ray diffraction (XRD) measurements were applied to the samples to identify the phases and their crystal structures.

The specimens for OM observation were electrolytically polished in a solution of 95 % CH_3COOH and

5 % $HClO_4$, and then etched in a solution of 5 % HNO_3, 15 % HF, and 80% H_2O. The main grain sizes were measured by the linear intercept method.

The specimens for XRD were abraded with SiC paper and were then subjected to diffraction using CuK_a radiation.

Quantitative determination of the volume percentage of titanium aluminide and secondary phases involved in the matrix, ceramic particles and retained porosity was performed by analysing optical and scanning electron micrographs of polished composite bars using the point counting method and image analysis and processing software.

Composite density measurements were carried out in accordance with Archimedes' principle, applying distilled water as the immersion fluid.

The initial density of the green compacts was calculated from the mass and geometry of the samples.

The tensile properties (tensile strength, 0.2 % tensile yield strength and elongation) of the composite specimens were determined in accordance with the ASTM test method, E8M-96. The tensile tests were conducted on cylindrical tension-test specimens 3.5 mm in diameter and 16 mm gauge length using an automated servo-hydraulic tensile testing machine with a crosshead speed of 0.254 mm/60 s.

3 RESULTS AND DISCUSSION

3.1 Morphology and chemical composition of laboratory prepared titanium aluminide powders

The morphology of laboratory prepared $TiAl_3$ powders, obtained by milling the pelletized products of reactive synthesis, is presented in **Figure 1**. As evident, the $TiAl_3$ powder obtained is non-agglomerated, with well shaped individual particles of particle size mostly below 10 μm.

The morphology of the raw titanium powder, **Figure 2**, is very similar with the morphology of synthesized $TiAl_3$. The main difference is in the average particle size,

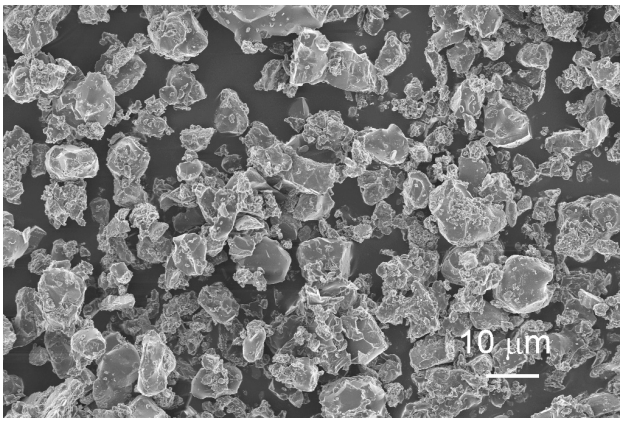

Figure 1: SEM micrograph of $TiAl_3$ after milling
Slika 1: SEM-posnetek $TiAl_3$-delcev po mletju

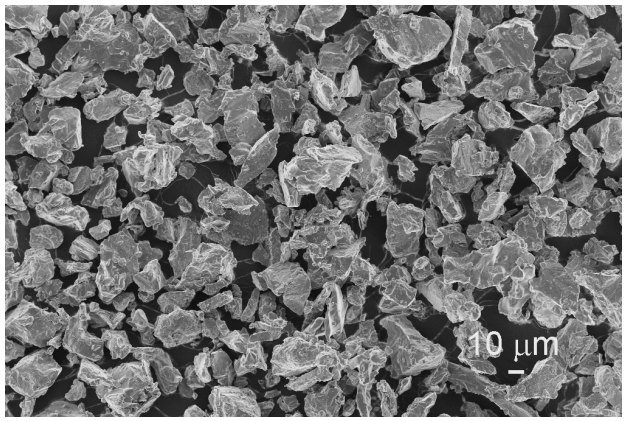

Figure 2: SEM micrograph of as-received commercial Ti powder
Slika 2: SEM-posnetek komercialnega Ti-prahu

which in the case of the as-received titanium powder is about three times larger.

The typical phase composition in synthesized $TiAl_3$ is reported in **Table 1**.

Table 1: Phase composition in laboratory prepared $TiAl_3$ powder
Tabela 1: Fazna sestava laboratorijsko pripravljenega $TiAl_3$ prahu

Phase	Volume fraction (*f*/%)
$TiAl_3$	87 ± 5
Al	10 ± 1
Ti	2 ± 0.2
Other phases	1 ± 0.1

3.2 Microstructural development in IMCs

Generally, the microstructure of IMCs consists of an intermetallic matrix (based on an ordered intermetallic compound or a multiphase combination of intermetallic compounds), the ceramic particulate reinforcement and the interfacial region with secondary phases formed during reactive sintering by chemical reactions proceeding between the ceramic reinforcement, $TiAl_3$ and/or non-reacted Al and Ti. As minor phases, solidified Al inclusions and individual titanium particles are also involved in the composite microstructure.

3.2.1 B_4C-Ti_3Al samples

Reactive sintering of B_4C-TiAl and B_4C-Ti_3Al composite samples resulted in specimens with densities higher than 95 % of T. D. As in densification, the boron carbide particulate reinforcement reacted with the intermetallic matrix forming numerous secondary phases (TiB_2, TiC, Al_3BC), well detectable in the microstructure of sintered samples – **Figure 3**.

In the B_4C-Ti_3Al and B_4C-TiAl samples intensive chemical reactivity between the composite constituents was observed during high temperature densification due to the fact that boron carbide reacts with both molten aluminium and solid titanium [15,16].

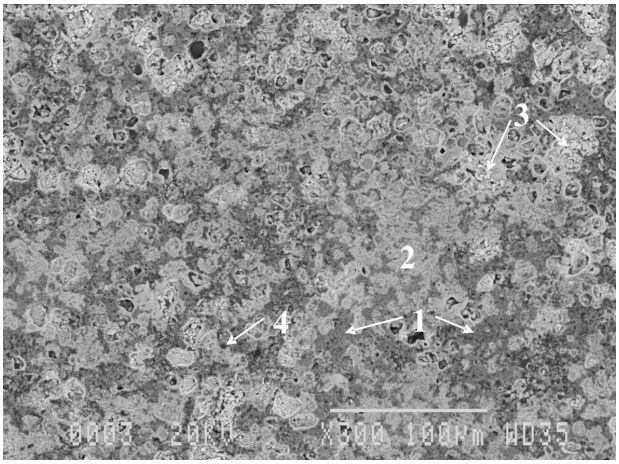

Figure 3: SEM micrograph of sintered $TiAl_3$-40 % B_4C composite sample with various phases identified by XRD: (1) Al, Al_4C_3, Al_3BC (2) AlTi, AlB_2, (3) TiB_2 and (4) B_4C

Slika 3: SEM posnetek sintranega $TiAl_3$-40 % B_4C-vzorca kompozita z različnimi fazami, identificiranimi z XRD: (1) Al, Al_4C_3, Al_3BC (2) AlTi, AlB_2, (3) TiB_2 in (4) B_4C

Boron carbide reacts at high temperature (1300 °C) with aluminium, forming mainly Al_3BC/Al_4C_3 and some AlB_2 (Reaction 1):

$$5B_4C_{(s)} + 19Al_{(l)} = 2Al_3BC_{(s)} + Al_4C_{3(s)} + 9AlB_2 \quad (1)$$

However, boron carbide also reacts with solid titanium particles producing secondary TiC and TiB_2:

$$B_4C_{(s)} + 3Ti_{(s)} = 2TiB_{2(s)} + TiC_{(s)} \quad (2)$$

Moreover, from thermodynamic point of view, boron carbide could also react with $TiAl_3$ causing its decomposition. The possible overall stoichiometric reaction between boron carbide and particulate $TiAl_3$ is the following:

$$64B_4C_{(s)} + 57TiAl_3 = 38TiB_{2(s)} + 19TiC_{(s)} + 18Al_3BC_{(s)} + 9Al_4C_{3(s)} + 81AlB_{2(s)} \quad (3)$$

3.2.2 TiB_2-$TiAl_3$ samples

TiB_2 is stable at 1300 °C in contact with both $TiAl_3$ and aluminium. Because of that, dense composite samples, **Figure 4**, are obtained only if a sufficient amount of elemental aluminium is present in the system as a liquid phase. The experimental findings suggest that the necessary amount of aluminium is about one third of the volume fraction of ceramic reinforcement. Sintering of $TiAl_3$-TiB_2 composites with a larger amount of ceramic reinforcement (>30 %) and without proper addition of elemental aluminium resulted in samples with a huge fraction of Kirkendall diffusion pores, as it is shown in **Figure 5**.

3.2.3 TiC-Ti_3Al samples

In this system, the best results of pressureless reactive sintering were experimentally obtained. Almost all the sintered samples, including these with a high amount (50 %) of ceramic reinforcement, had a retained porosity below 5 %, among which many were fully dense.

As in the case of B_4C, TiC may also react with $TiAl_3$ and elemental aluminium. The products of these reactions are various Ti-Al-C phases (e.g. Ti_3AlC, Ti_3AlC_2 and Ti_2AlC) and Al_4C_3. The presence of these phases was confirmed by SEM-EDS at the matrix-reinforcement interface of the fabricated composites, **Figures 6, 7**.

3.3 Mechanical properties

The results of room temperature tensile tests on the composite samples are listed in **Table 2**. As a result of matrix reinforcement, significant improvements in Young's modulus, tensile strength and ultimate tensile

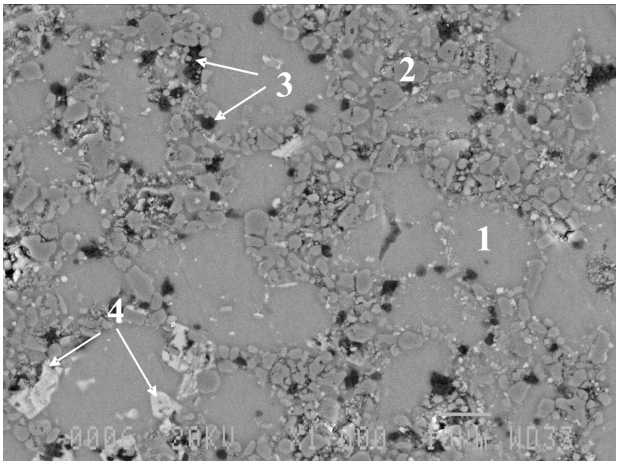

Figure 4: Microstructure of a pressureless sintered $TiAl_3$-30 %TiB_2 -10 % Al composite. The microstructural constituents are: (1) Al_3Ti, (2) TiB_2 (3) Al and (4) traces of Al_2O_3

Slika 4: Mikrostruktura $TiAl_3$-30 % TiB_2 -10 % Al-kompozita, sintranega pri atmosferskem tlaku. Mikrostrukturni gradniki so: (1) Al_3Ti, (2) TiB_2 (3) Al in (4) sledovi Al_2O_3

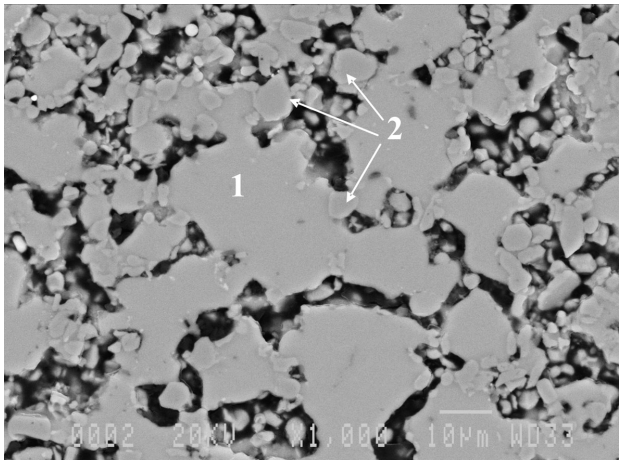

Figure 5: Scanning electron micrograph of pressureless sintered $TiAl_3$-50 % TiB_2 composite with a significant number of Kirkendall diffusion pores: (1) Al_3Ti and (2) TiB_2

Slika 5: SEM-posnetek $TiAl_3$-50 % TiB_2 kompozita sintranega pri atmosferskem tlaku s številnimi Kirkendallovimi porami: (1) Al_3Ti in (2) TiB_2

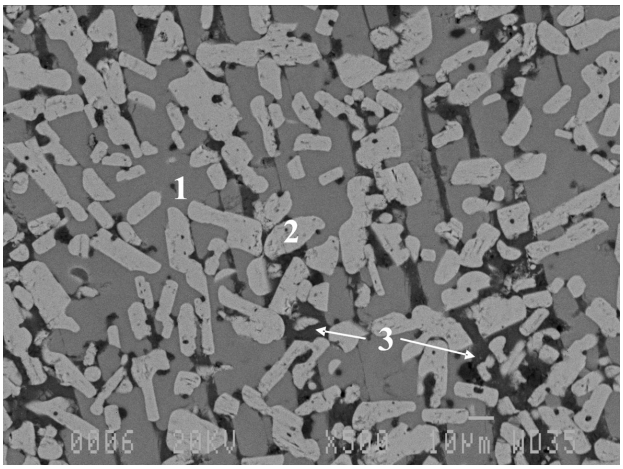

Figure 6: SEM micrograph of a $TiAl_3$-30 % TiC composite: (1) $TiAl_3$ matrix, (2) Ti-Al-C phase and (3) Al

Slika 6: SEM-posnetek $TiAl_3$-30 % TiC kompozita: (1) $TiAl_3$ matrica, (2) Ti-Al-C faza in (3) Al

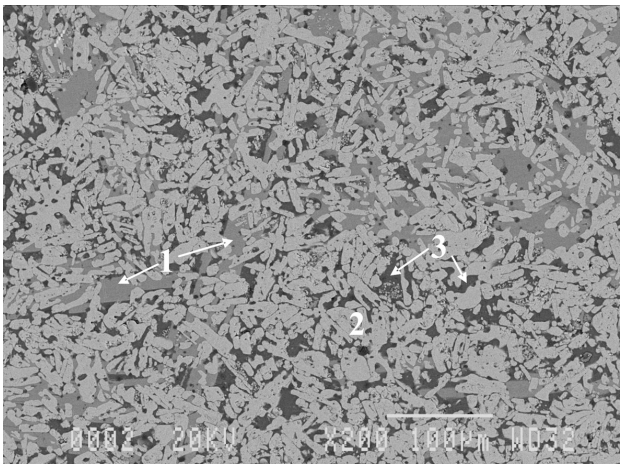

Figure 7: Microstructure developed in $TiAl_3$-40 % TiC: (1) $TiAl_3$, (2) Ti-Al-C and (3) Al with up to 5 % of Ti

Slika 7: Mikrostruktura $TiAl_3$-40 % TiC-kompozita: (1) $TiAl_3$, (2) Ti-Al-C in (3) Al z do 5 % Ti

strength of the fabricated composites were observed. At the same time, the highest improvement of tensile properties caused by reinforcement was observed in samples reinforced with TiC and B_4C and less in samples reinforced with TiB_2. Comparing the mechanical properties of composite samples with various volume fractions of ceramic particles in the matrix, it was found that Young's modulus, tensile strength and ultimate tensile strength increase while elongation decreases with an increasing fraction of ceramic reinforcement.

4 CONCLUSION

A $TiAl_3$ sintering mixture (87 % $TiAl_3$, 10 % Al and 1 % Ti) for composite fabrication was routinely reaction synthesized from the elements – (solid titanium particles and molten aluminium) with an almost 100 % reaction yield. Reaction synthesis was performed at moderate temperature (1300 °C) for 2 h under a flowing atmosphere of Ar + 4 % H_2. The reaction product was milled in a conventional planetary mill, resulting in particulates with an average particle size of 10 μm.

Table 2: Average room temperature tensile properties of various laboratory prepared $TiAl_3$-B_4C, TiC, TiB_2 composite samples

Tabela 2: Povprečne vrednosti mehanskih lastnosti (dobljene pri sobni temperaturi) kompozitov na osnovi $TiAl_3$, ojačanih z B_4C, TiC, TiB_2

Volume fraction of ceramic reinforcement in $TiAl_3$ matrix φ/%	Retained porosity in sintered samples %	E/GPa	Tensile strength σ/MPa	0.2 % tensile yield strength σ/MPa	Elongation in 50 mm Δl/%
10-B_4C	1.4±0.1	187±20	332±33	274±27	0.8±0.08
20-B_4C	2.2±0.2	207±22	352±35	298±30	0.6 ±0.06
30-B_4C	3.1±0.3	228±23	377±38	324±32	0.5±0.05
40-B_4C	3.9±0.4	241±24	394±40	346±35	0.3±0.03
50-B_4C	4.6±0.5	249±25	423±42	368±37	0.2±0.02
10-TiC	1.1±0.1	218±22	374±37	329±33	0.5±0.05
20-TiC	1.7±0.2	241±24	409±41	366±37	0.4±0.04
30-TiC	1.9±0.2	270±27	453±45	400±40	0.3±0.03
40-TiC	2.1±0.2	297±30	489±49	431±43	0.3±0.03
50-TiC	2.4±0.2	321±31	513±51	467±47	0.2±0.02
10-TiB_2	3,9±0.4	149±15	298±30	209±21	0.7±0.07
20-TiB_2	4,6±0.5	167±17	318±32	229±23	0.5±0.05
30-TiB_2	5,0±0.5	188±19	331±33	248±25	0.4±0.04

Dense (>95 % of theoretical density) $TiAl_3$-based composites reinforced with 10–50 % of B_4C or TiC and 10–30 % of TiB_2 particles were successfully prepared by combining pressureless reaction synthesis and reaction sintering.

Irrespective of the ceramic reinforcement applied, dense composite samples reinforced with 10 % to 30 % of ceramic particulates were successfully obtained, revealing the significant industrial potential of this fabrication method. The retained porosity in sintered samples was less than 5 %.

The highest chemical affinity between ceramic reinforcement and matrix was observed in the $TiAl_3$-TiC and $TiAl_3$-B_4C systems, while $TiAl_3$-TiB_2 was chemically inert. The sintering of $TiAl_3$-TiC and $TiAl_3$-B_4C samples proceeds via formation of various secondary phases involved in the process of densification. Accordingly, $TiAl_3$-TiC and $TiAl_3$-B_4C samples with as much as 50 % of ceramic reinforcement were successfully pressurelessly sintered. On the other hand, sintering in $TiAl_3$-TiB_2 was achieved by the liquid phase (molten aluminium). Hence, in $TiAl_3$-TiB_2 samples with more than 30 % of ceramic particulates, under the applied sintering conditions Kirkendall diffusion pores were not reduced below 10 %.

Regarding the room temperature tensile properties of the composite samples, the highest improvement was obtained in $TiAl_3$-TiC and $TiAl_3$-B_4C samples with the highest amount (50 %) of ceramic reinforcement, while

in $TiAl_3$-TiB_2 samples the improvement was rather moderate. Generally, the improvement of tensile strength, tensile yield strength and modulus was found to correlate with amount of ceramic reinforcement in the matrix, irrespective of the sort of reinforcement. However, quite the opposite behaviour was found regarding elongation, where the introduction of ceramic particles into the intermetallic matrix led in all specimens to a significant reduction of ductility and toughness.

Acknowledgment

This work was supported by funding from the Public Agency for Research and Development of the Republic of Slovenia, as well as the Impol Aluminium Company from Slovenska Bistrica, Slovenia, under contract No. 1000-07-219308

5 REFERENCES

[1] *Gamma Titanium Aluminide 1999*, Y. W. Kim, D. M. Dimiduk, M. H. Loretto, eds., TMS, Warrendale, PA, 1999, 3

[2] S. Djanarthany, J. C. Viala, J. Bouix: *Mater. Chem. Phys.*, 72 (**2001**), 301

[3] C. M. Ward-Close, R. Minor, P. J. Doorbar: *Intermetallics*, 4 (**1996**), 217

[4] E. K: Y. Fu, R. D. Rawlings, H. B. McShane, *J. Mater.Sci.*, 36 (**2001**), 5542

[5] M. Sujata, S. Bhabgava, S. Sangal, *J. Mater. Sci. Lett.*, 16 (**1997**), 1175

[6] G. Sauthoff, Basic of thermodynamics and phase transitions in complex intermetallics, edited by E. B. Ferre, World Scientific, London, 2008, 147

[7] G. X. Wang, M. Dahms, *JOM*, 5 (**1993**), 52

[8] M. Dahms, F. Schmeizer, J. Seeger, B. Wildhagen, *Mater. Sci. Technol.*, 8 (**1992**), 359

[9] S. Kazuhisa, F. Tsutomu, M. S. Kim, K. Masaki, *Powder Metall.*, 41 (**1994**), 146

[10] J. B. Yang, K. W. Teoh, W. S. Hwang, *Mater. Sci. Technol.*, 13 (**1997**), 695

[11] F. Wenbin, H. Lianxi, H. Wenxiong, W. Erde, L. Xiaoqing, *Mater. Sci. Eng.*, A 403 (**2005**), 186

[12] G. X. Wang, M. Dahms, *Powder Metall.*, 24 (**1992**), 219

[13] F. J. J. Van Loo, G. D. Rieck, *Acta Metall.*, 21 (**1973**), 61

[14] M. Dahms, *Mater. Sci. Eng. A*, 110 (**1989**), 5

[15] G. Arslan, F. Kara, S. Turan, *J. Eur. Ceram. Soc.*, 23 (**2003**), 1243

[16] J. Jung, S. Kang, *J. Am. Ceram. Soc.*, 87 (**2004**), 47

UDK 669.14.018.8:621.785.3
Original scientific article/Izvirni znanstveni članek

ISSN 1580-2949
MTAEC9, 43(3)129(2009)

MAGNETIC CHARACTERISTICS OF ISOTHERMALLY AGED Cr-Ni-Mo-BASED ALLOYS WITH DIFFERENT δ-FERRITE CONTENTS

MAGNETNE LASTNOSTI IZOTERMNO ŽARJENIH ZLITIN Cr-Ni-Mo Z RAZLIČNO VSEBNOSTJO δ-FERITA

Borivoj Šuštaršič[1], Benjamin Podmiljšak[2], Paul McGuiness[2], Jelena V. Tuma[1]

[1] Institute of Metals and Technology, Lepi pot 11, 10000 Ljubljana, Slovenia
[2] Jožef Stefan Institute, Jamova cesta 39, Ljubljana, Slovenia
borivoj.sustarsic@imt.si

Prejem rokopisa – received: 2009-02-27; sprejem za objavo – accepted for publication: 2009-03-04

We have investigated the influence of δ-ferrite content in Cr-Ni-Mo stainless-steel cast alloys on the magnetic characteristics. Samples of cast alloys with mass fractions 9-11 % of Ni, 18-21 % of Cr and 1.8-2.5 % of Mo, with three characteristically different δ-ferrite contents, were prepared with careful selection of appropriate amounts of alloying elements and a controlled solidification procedure. The samples were then aged in the operating temperature region (290 – 350 °C) for different periods of time (up to two years). The δ-ferrite content was determined with three different methods: i.e., empirically on the basis of chemical composition, magnetic-induction-based and metallographically. The magnetic-induction-based determination of δ-ferrite content showed that it does not change with ageing temperature and time. It confirms that only the internal ferrite structure is changed during ageing because of the spinodal decomposition.

The absolute magnetic properties were determined with a hysteresisgraph and a vibrating-sampling magnetometer (VSM). The results showed that the magnetic properties depend on the chemical composition (δ-ferrite content), the ageing temperature and the time. The chemical composition has the biggest influence, but the influence of the ageing temperature and time is insignificant and the scatter of the results is relatively large. The determination of the absolute magnetic properties is a destructive method and the mechanical preparation of the samples can influence the magnetic properties. Therefore, the method is not appropriate for the *in-situ* observation of the kinetics of spinodal decomposition. Measurements with the VSM are more appropriate than with the hysteresisgraph because much smaller samples with any geometry can be used.

Keywords: Cr-Ni-Mo based stainless steel, isothermal ageing, magnetic properties, influence of δ-ferrite

Raziskovali smo vpliv vsebnosti delta ferita na magnetne lastnosti Cr-Ni-Mo nerjavnih jeklenih litin. Izdelali smo tri različne litine v območju sestav z masnimi deleži med 9 in 11 % Ni, 18 in 21 % Cr in od 1,8 do 2,5 %Mo. Skrbno smo izbrali primerno vsebnost posameznih legirnih elementov in kontrolirali pogoje strjevanja, da smo dobili litine z različno, karakteristično vsebnostjo δ-ferita (s približno 4, 15 in 30 prostorninskimi deleži). Vzorce litin smo različno dolgo (do dveh let) izotermno žarili v temperaturnem območju (med 290 in 350 °C), ki je karakteristično za obratovanje uparjalnikov nuklearnih elektrarn. Vsebnost δ-ferita različno staranih vzorcev smo določevali na tri različne načine: empirično na osnovi kemijske analize, na osnovi merjenja magnetne indukcije in metalografsko. Meritve vsebnosti δ-ferita na metalografskih vzorcih so pokazale, da se le-ta ne spreminja s časom in temperaturo izotermnega žarjenja. To potrjuje predpostavko, da se med izotermnim žarjenjem ne spreminja vsebnost δ-ferita temveč le njegova notranja struktura zaradi spinodalnega razpada.

V vzorcih preiskovanih litin smo določili tudi absolutne magnetne lastnosti z merilnikom magnetne histereze in vibracijskim magnetometrom (VSM). Rezultati meritev so pokazali, da so magnetne lastnosti odvisne tako od sestave (vsebnosti δ-ferita) kot tudi temperature in časa izotermnega žarjenja. Največji vpliv ima vsebnost δ-ferita. Vpliv temperature in časa izotermnega žarjenja je manjši z opaznim raztrosom merjenih vrednosti. Določevanje magnetnih lastnosti je porušitvena metoda, saj moramo vzorec materiala izrezati iz elementa ali konstrukcije, ki jo preiskujemo. Mehanska izdelava preizkušanca lahko vpliva na magnetne lastnosti. Zato ta metoda ni najprimernejša za opazovanje sprememb *in-situ* med izotermnim žarjenjem oziroma spinodalnim razpadom. Magnetne meritve z VSM so primernejše, ker zahtevajo precej manjše vzorce poljubne oblike.

Ključne besede: nerjavna jekla na osnovi Cr-Ni-Mo, izotermno žarjenje, magnetne lastnosti, vpliv vsebnosti δ-ferita

1 INTRODUCTION

High-alloyed Cr-Ni-based stainless-steel cast alloys are frequently used in thermoelectric installations such as conventional and nuclear power plants (NPPs)[1,2]. Many years of exploitation of mechanical equipment in these objects have shown that the toughness of these alloys decreases with the operating time and temperature[3-7]. These alloys have a characteristic two-phase microstructure consisting of austenite and δ-ferrite[8–10]. The δ-ferrite content depends on the chemical composition of the alloy and on metallurgical factors: i.e., manufacturing technology and the exploitation conditions. Therefore, in alloys with a chemical composition the allowed ranges of content of alloying elements completely different microstructures can form. The result of this could be different mechanical properties of a material and it different behavior during its exploitation. Actually, our investigations have already confirmed that the Charpy impact energy and the resistance to stable crack growth of such alloys depend strongly on the δ-ferrite content[11,12].

Extensive investigations in the past indicate for the change of properties of these alloys the spinodal decomposition of δ-ferrite is responsible. Investigations also showed that the austenite phase does not play a

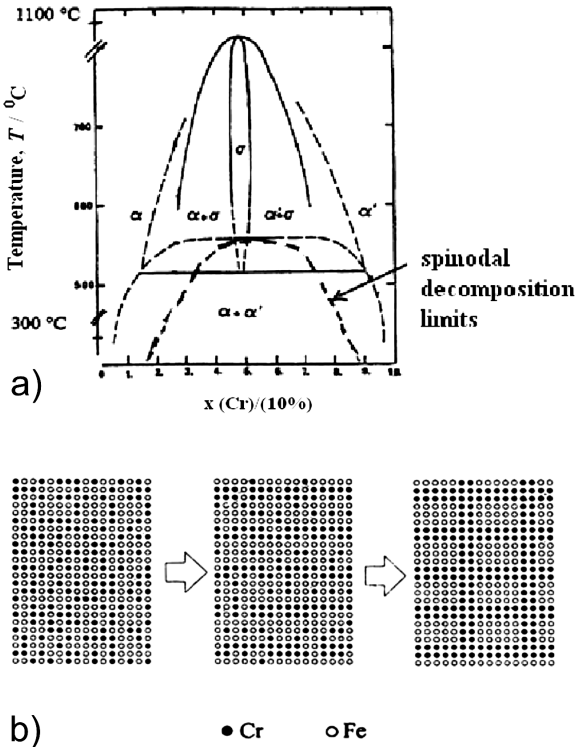

Figure 1: Schematic presentation of: a) quasibinary Fe-Cr-Ni-Mo phase diagram and b) redistribution of Fe and Cr atoms during spinodal decomposition[13]

Slika 1: Shematična predstavitev: a) kvazibinarni diagram Fe-Cr-Ni-Mo in b) prerazporeditev atomov Fe in Cr med spinodalnim razpadom[13]

significant part in this process. Spinodal decomposition in these types of alloys one can understand as it is schematically shown in **Figure 1**, and it is clear that the final result of spinodal decomposition is coherent, two-phase structure with different Cr-to-Ni ratios, even in a relatively low-temperature range (300 – 350 °C). This temperature range is similar to the operating-temperature range of vital parts of, for example, the coolant system[6]. The formation of two phases with the same crystal structure but different lattice parameters causes high internal elastic stresses, resulting in significant hardness increase and toughness decrease.

Besides the microstructural investigations, mechanical testing and analyses of isothermally aged materials[11,12] the aim of our work was also to find out if microstructural and related mechanical changes can be monitored and connected to a change of magnetic properties. One of the most useful non-destructive methods for the determination of δ-ferrite content is based on magnetic induction, because in two-phase systems (for example, ferrite-austenite) ferrite is the ferromagnetic phase. The amount of this phase is almost linearly proportional to the measured magnetic induction and therefore the method became a standard *in-situ* checking procedure for thermoelectric installations[9,14–15], especially when new reparative welds or parts are introduced during service. However, publications in the context of changes of the absolute magnetic properties (the hysteresis loops) of these types of alloys during isothermal annealing could not be found. Therefore, some investigations and analyses were performed relating to the change of the magnetic properties of thermally degraded material.

2 EXPERIMENTAL

The samples of a Cr-Ni-Mo-based cast alloy, CF-8M-type (ASTM A351), were prepared with a standard casting procedure. Twenty-kg batches of melts of the selected chemical composition were prepared in an inductive melting furnace and then cast into metal moulds under a controlled casting and solidification conditions. The solidification rate was controlled with the selection of an appropriate type of mould and melt/mould preheating. Cooled, cast ingots of each chemical composition (see **Table 1**), designated as alloys ***A***, ***B*** and ***C***, were cut and ground into parallel slices, approx. 10 mm thick. The actual chemical compositions of the prepared alloys were determined with optical and ion-coupled-plasma atomic emission spectroscopy (OES and ICP-AES).

On the basis of well-known empirical correlations (**equation (1)** and **(2)**) the Cr and Ni equivalents, as well as the δ-ferrite content were calculated[16]. Such a calculation shows that the alloy CF-8M inside the allowed chemical composition can practically contain from 0 to 90 volume fractions of δ-ferrite.

$$CR = \frac{w(Cr_{eq})}{w(Ni_{eq})} = \\ = \frac{w(Cr) + 1.5W(Si) + 1.4w(Mo) + w(Nb) - 4.99}{w(Ni) + 30w(C) + 0.5w(Mn) + 26(w(n) - 0.02) + 2.77} \quad (1)$$

$$F = -68.768 + 157.909CR - 133.171CR^2 + 47.1849CR^3 \quad (2)$$

Table 1: Nominal and actual chemical composition of the prepared alloys
Tabela 1: Nazivna in dejanske kemične sestave pripravljenih zlitin

Alloy designation	Chemical composition in mass fractions (w/%)								Cr and Ni equivalent	
	C	Si	Mn	P	S	Ni	Cr	Mo	Cr_{eq}	Ni_{eq}
CF-8M	<0.08	<2.0	<1.5	<0.04	<0.04	9–12	18–21	2-3	15.8–23.2	11.3–17.4
A	0.06	0.43	1.59	0.03	0.01	11.9	18.0	1.84	16.2	16.8
B	0.07	0.67	1.04	0.03	0.01	11.0	21.7	2.03	20.6	15.9
C	0.06	1.68	0.67	0.03	0.01	9.0	20.8	2.46	21.8	13.4

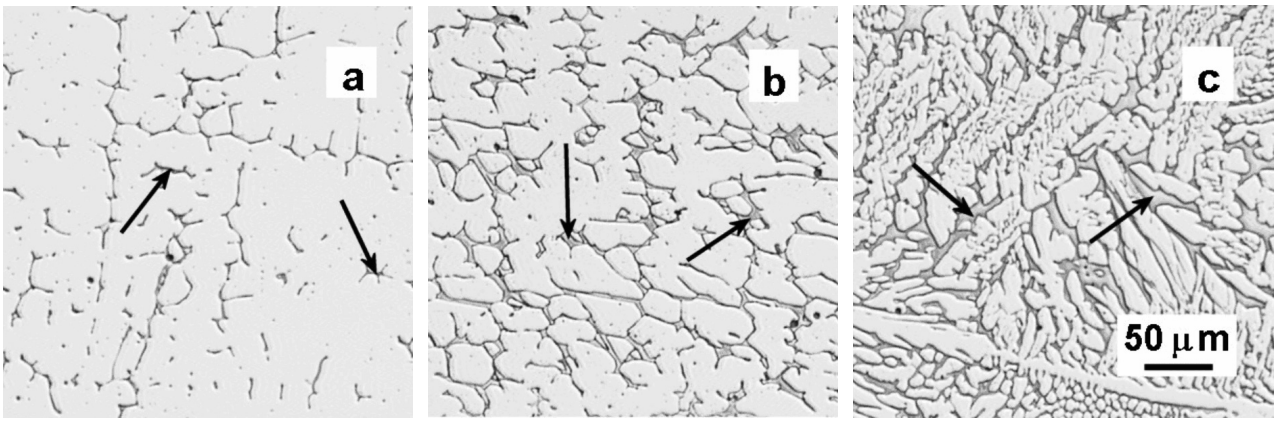

Figure 2: Micrographs of as-cast microstructures of investigated steels: **a)** alloy ***A*** with approx. 18Cr-12Ni, **b)** alloy ***B*** with 22Cr-11Ni and **c)** alloy ***C*** with approx 21Cr-9Ni, light-grey areas represent austenite, dark-grey areas marked with arrows are islands of δ-ferrite; LM, original magnification 200-times, selective etching of δ-ferrite (KOH : $K_3[Fe(CN)_6]$: H_2O=0.25 : 0.25 : 0.50).

Slika 2: Posnetki mikrostrukture preiskovanih jekel: **a)** zlitina ***A*** z 18 % Cr in 12 % Ni, **b)** zlitina ***B*** s približno 22 % Cr in 11 % Ni in **c)** zlitina ***C*** s približno 21 % Cr in 9 % Ni, svetla področja predstavljajo austenit, temna področja označena s puščicami pa so otočki δ-ferita; optični mikroskop, originalna povečava 200-krat, selektivno jedkanje na δ-ferit (KOH : $K_3[Fe(CN)_6]$: H_2O=0,25 : 0,25 : 0,50).

At the characteristic ingot positions the samples for metallographic investigations were cut and the average δ-ferrite content of each slice was determined magnetically and metallographically. Typical microstructures visible under a light microscope (LM) are presented in **Figures 2 a**, **b** and **c**.

A determination of the δ-ferrite content based on the magnetic induction (**Figure 3 a**) was performed with two instruments: i.e., an older one regularly used at NPPs and a new, digital one, the Feritscope MP-30 Fischer GmbH, Germany (**Figure 3 b**), with the appropriate calibration samples. The measured values obtained with different methods/instruments are shown in **Table 2**. It is clear that the differences in the measured values are relatively large. But the range of measured values obtained with one measuring method seems acceptable. The magnetically obtained values strongly depend on the sample surface and its shape, and therefore only the flat, polished surfaces of metallographic samples were used.

Slices of prepared alloys were then put into the laboratory batch furnaces and artificially aged (isothermally annealed) at elevated temperatures for different periods of time. The selected temperatures of ageing were 290, 320 and 350 °C and the time of 24 h, 1 and 6 months, and finally one and two years. After each ageing temperature/time cycle samples for microstructure characterization and mechanical testing were prepared. The average δ-ferrite content was again determined with an induction-based method on the polished metallographic samples.

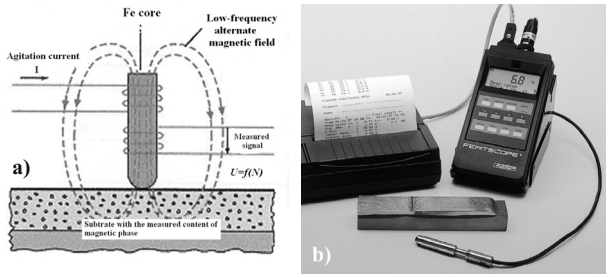

Figure 3: Determination of δ-ferrite content based on the magnetic induction: a) schematic presentation and b) modern digital ferritemeter (Ferritescope MP-30, Fischer GmbH, Germany)[17]

Slika 3: Določevanje vsebnosti δ-ferita na osnovi magnetne indukcije: a) shematični prikaz in b) moderen digitalni feritmeter (Ferritescope MP-30, Fischer GmbH, Nemčija)[17]

Table 2: Initial δ-ferrite content, determined with different methods/ instruments

Tabela 2: Začetna vsebnost δ-ferita, določena na različne načine

Alloy designation	δ-ferrite content in volume fractions (φ/%)			
	Calculated*	Metallographically	Ferritmesser (NPP)	Ferritescope MP-30
A	2.1	1.2–6.3	1.5–2.5	3.5–4.7
B	14.9	14.0–18.3	10.0–12.0	14.6–19.2
C	38.8	28.5–34.0	26.0–28.0	27.9–32.9

* equations **(1)** and **(2)**

For the determination of the absolute magnetic properties with a hysteresisgraph (permagraph RE3, Magnet Physic Dr. Steingroever) cylinders dimensions of (ϕ 10 × 12) mm were used. For measurements with a vibrating-sampling magnetometer (VSM) small plates with dimensions of approx. (1.5 × 1.5 × 1.5) mm were used. The VSM has become a widely used instrument for determining the magnetic properties of a large variety of materials in the subzero and elevated temperature regions[18]. The investigated material was placed into a uniform magnetic field and mechanically vibrated, resulting in some magnetic flux change. The induced voltage in the pick-up coils is proportional to the magnetic moment of the sample.

3 RESULTS AND DISCUSSION

Figure 4 shows the results of the δ-ferrite content determined with Ferritescope, depending on the temperature and the time of isothermal ageing of the prepared alloys. It is clear that the δ-ferrite content is virtually independent of the ageing time and temperature. A slight trend for a decrease in the δ-ferrite content can be noticed, but only for alloy *C* at all temperatures and for alloy *B* at the highest temperature (350 °C). But it is in the range of the scatter of the measured results. Therefore, we can conclude that the induction-based method is not an appropriate method for monitoring of the kinetics of thermal degradation of the selected material. It seems an appropriate result and conclusion because during spinodal decomposition the changes occur at the nano-level, connected with small fluctuations of chemical composition and the cell parameters. However, the Ferritscope detects the average magnetic induction of much larger local regions (approx. 1 mm^2 and 1 mm^3, respectively), made up of ferromagnetic (ferrite) and nonmagnetic (austenite) grains. The method can, therefore, only serve as a control for the initial content of the chemical composition (δ-ferrite content), as well as an *in-situ* checking procedure for new welds and the replaced structural elements of thermoelectric installations during maintenance. As an example, **Figure 5** shows the change in δ-ferrite content across the but-weld of thin plates made of 316 L stainless steel at two different locations.

The hysteresis loop is the basic magnetic characteristic for ferromagnetic materials. From such a loop it is possible to read the remanence B_r, the coercivity H_c, the saturation magnetization B_s and the permeability μ. These properties are composition and structure sensitive; therefore, one can expect that it would be possible to monitor the kinetics of the spinodal decomposition.

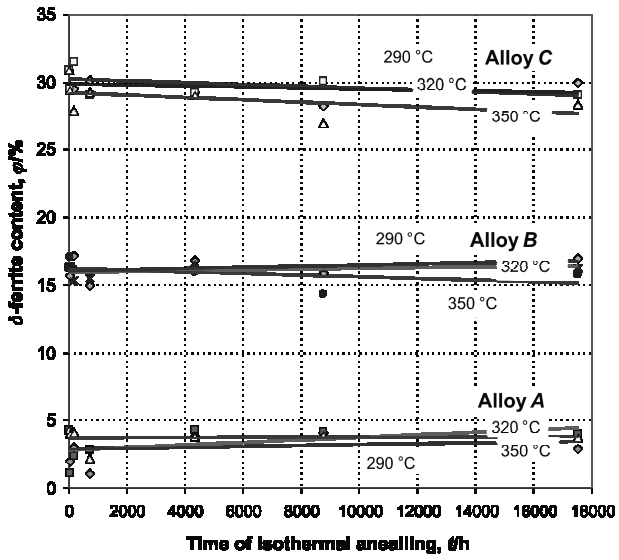

Figure 4: Average δ-ferrite content vs. time and temperature for isothermal annealing of all the prepared alloys, determined with the Feritscope MP-30 (Fischer GmbH, Germany)

Slika 4: Povprečna vsebnost δ-ferita v zlitinah *A*, *B* in *C* v odvisnosti od časa in temperature izotermnega žarjenja, določena s feritmetrom (Feritscope MP-30, Fischer GmbH, Nemčija)

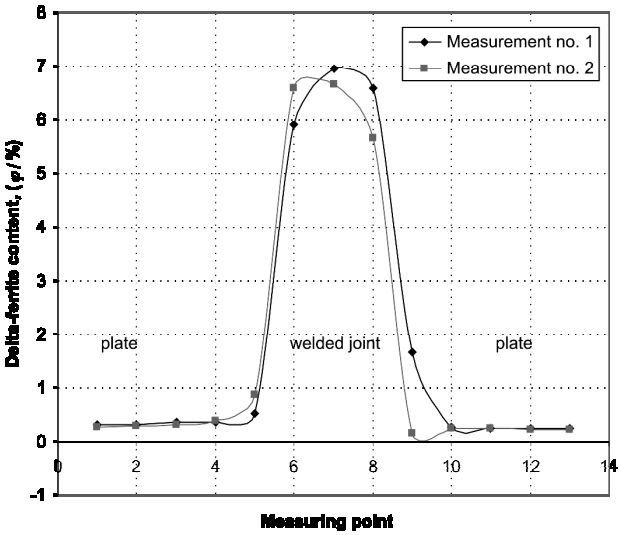

Figure 5: Change of δ-ferrite content across but-welded joint of thin plates made of 316 L stainless steel at two different measuring locations

Slika 5: Sprememba vsebnosti δ-ferita vzdolž zvarnega spoja dveh tankih plošč iz nerjavnega jekla vrste 316 L, merjena na dveh različnih lokacijah

The investigated material can be treated as a composite material with a different volume content of magnetic phase (δ-ferrite). Correspondingly, it is expected that the hysteresis curves of the investigated alloys change size and shape with an increased content of δ-ferrite. **Figure 6** shows the hysteresis loops of the original non-aged state of all three prepared alloys. As expected, alloy *C,* with the largest content of magnetic phase, has the narrowest and most upright hysteresis curve, with higher B_r, B_s and lower H_c in comparison

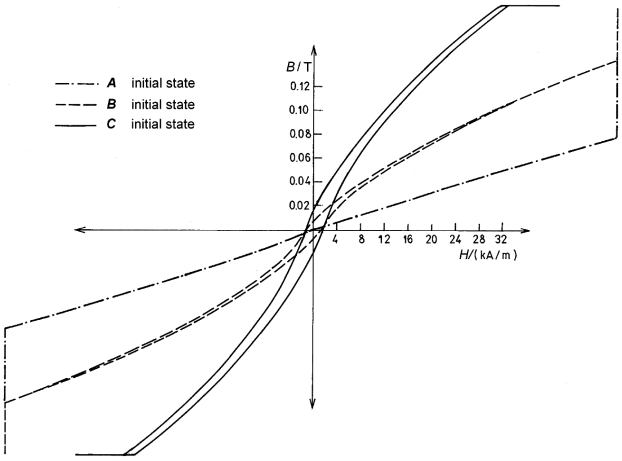

Figure 6: Hysteresis loops determined by Remagraph RE3, sample dimensions (ϕ 10 × 12) mm, original non-aged state of material

Slika 6: Histerezne zanke, ugotovljene z napravo Remagraph RE3, dimenzije vzorcev (ϕ 10 × 12) mm, originalno nežarjeno stanje materiala

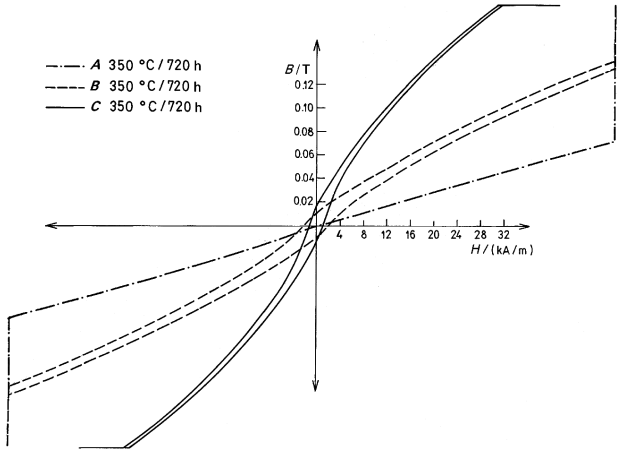

Figure 7: Hysteresis loops determined by Remagraph RE3, sample dimensions (ϕ 10 × 12) mm, aged 720 h at 350 °C

Slika 7: Histerezne zanke, ugotovljene z napravo Remagraph RE3, dimenzije vzorcev (ϕ 10 × 12) mm, izotermno žarjeno 720 h pri 350 °C

with alloy *B,* which has a lower content of ferromagnetic phase. Alloy *A* has a very low content of ferromagnetic phase and therefore shows an almost linear relation for the applied field vs. the induction (paramagnetic). **Figure 7** shows the hysteresis loops for alloys aged at 350 °C for 720 h. Its shapes and sizes are similar, and the differences in the magnetic properties compared to the original non-aged alloys are negligible. Therefore, the selected instrument is not the most appropriate for monitoring the spinodal decomposition of the selected alloys.

The hysteresis loops were then determined with the VSM. This method enables the use of smaller samples without any limits in terms of geometry and surface quality. The magnetic properties of the prepared materials were measured at 20 °C and 300 °C. The influence

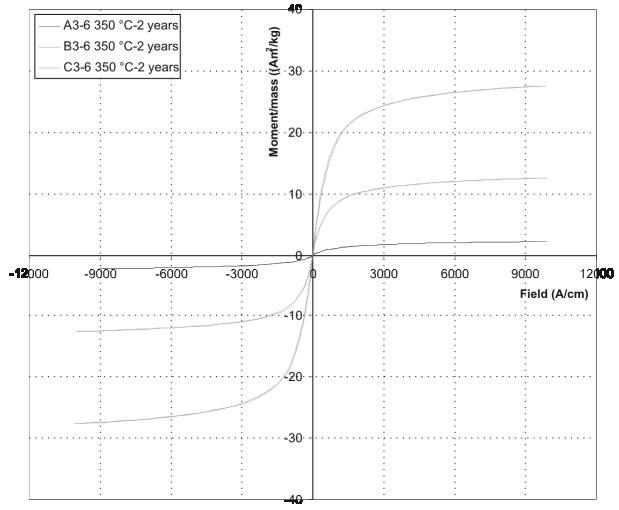

Figure 8: Typical hysteresis loops determined with the VSM, obtained for alloys *A*, *B* and *C* and aged 2 years at 350 °C

Slika 8: Tipične histerezne zanke, ugotovljene z VSM na zlitinah *A*, *B* in *C*, izotermno žarjene dve leti pri 350 °C

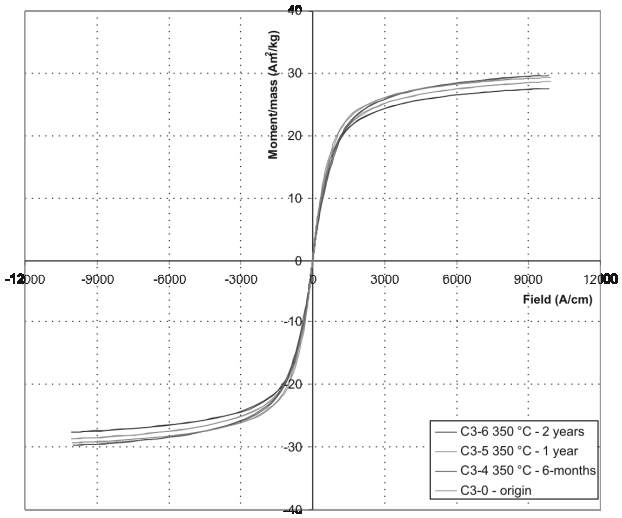

Figure 9: Typical hysteresis curves obtained with the VSM for alloy *C,* aged at 350 °C for different periods of time

Slika 9: Tipične histerezne zanke, ugotovljene z VSM pri zlitini *C*, različno dolgo časa izotermno žarjeni pri 350 °C

of the internal stresses had to be taken into account and any cutting/mechanical machining must be avoided or carefully carried out. **Figure 8** shows the room-temperature hysteresis loops of alloys aged at 350 °C for two years. The differences in the hysteresis curves are evident and they are similar to those obtained with the permagraph.

Figure 9 shows the room-temperature hysteresis loops of alloy ***C*** aged at 350 °C for different periods of time. It is clear that with increased ageing time the saturation magnetization decreases, but the changes are relatively small (approx. 27–29 emu/g). Also, the changes in the coercivity and the remanent induction are

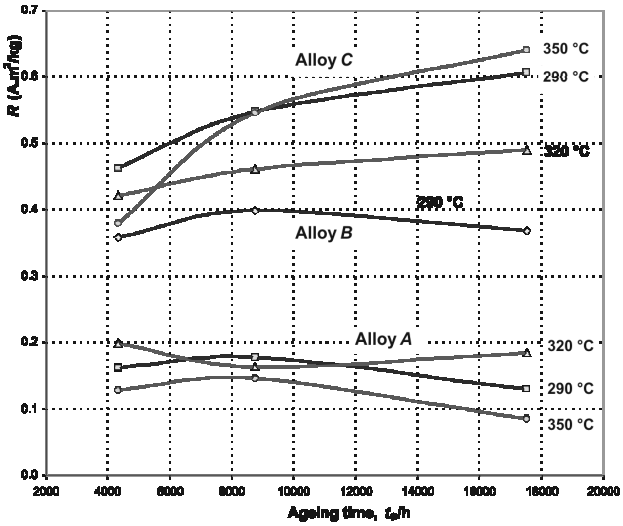

Figure 10: Average room-temperature remanent induction *R* vs. ageing time obtained for cast alloys with two different δ-ferrite content, aged at (290, 320 and 350) °C

Slika 10: Povprečna remanentna indukcija *R* določena pri 20 °C v odvisnosti od časa izotermnega žarjenja zlitin z različno vsebnostjo δ-ferita, žarjeno pri (290, 320 in 350) °C

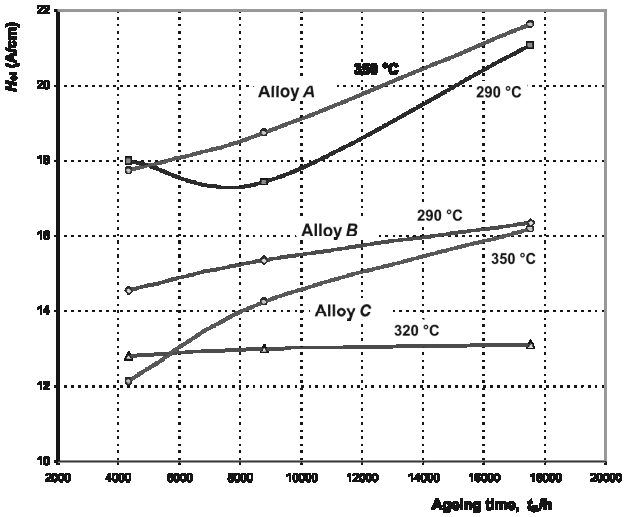

Figure 11: Average room-temperature **c**oercivity vs. ageing time obtained for the investigated cast alloys, aged at (290, 320 and 350) °C

Slika 11: Povprečna koercitivnost, izmerjena pri 20 °C, v odvisnosti od časa izotermnega žarjenja zlitin z različno vsebnostjo δ-ferita, žarjeno pri (290, 320 in 350) °C.

very small and are close to the limits of the sensitivity of the VSM. The remanent induction (***R***) and the coercivity ($\boldsymbol{H}_{ci}$) were read from the measured hysteresis curves and put into the diagrams in order to show the intrinsic properties vs. the ageing conditions for the individual alloys.

Figure 10 shows the room-temperature *R* of the alloys ***A***, ***B*** and ***C,*** aged up to two years at (290, 320 and 350) °C. Its change for non-magnetic alloy ***A*** is almost negligible, but it increases significantly for alloy ***C***, which has the highest content of ferromagnetic phase. The alloy ***B*** shows an almost negligible change, similar to alloy ***A***.

Figure 11 shows the room-temperature coercivity of alloys ***A***, ***B*** and ***C*** aged up to two years at selected temperatures. In this case the alloys show an increase of coercivity with ageing time. Surprisingly, alloy ***C*** at 320 °C does not show this increase.

Inconsistencies are noticed in the obtained results and shown in **Figures 10** and **11**. However, it is obvious that the change in the remanent induction and the coercivity are connected with structural changes. Therefore, we can also conclude that the kinetics of the spinodal decomposition can be monitored from the change in the absolute magnetic properties, but probably a more suitable instrument, specially designed for measurements of low coercivity soft magnetic materials, should be used.

4 CONCLUSIONS

The magnetic-induction-based determination of the δ-ferrite content showed that it does not change significantly with ageing temperature and time. It confirms that only the internal ferrite structure is changed, during ageing, because of the spinodal decomposition. Therefore, it can be concluded that magnetic induction is not appropriate method to observe spinodal decomposition in SS cast alloys. It can only serve as information or control for either the initial materials' content of δ-ferrite or as checking procedure during the maintenance of thermo-energetic objects.

The kinetics of spinodal decomposition can be monitored by a change in the absolute magnetic properties. However, these methods are destructive, as well as stress and temperature sensitive. The scatter of the results is relatively large and, therefore, sometimes they are inconsistent. The changes in the magnetic properties are also relatively small and so an appropriate measuring instrument has to be chosen.

5 REFERENCES

[1] K. H. Herter et al: Leak-before-break behaviour of piping comparison of testing with calculation, VGB PowerTech, 11 (**2001**), 84–92

[2] L. Skanberg: PWSCC observations Ringhals 3 and 4 safe ends, SMiRT-16 Conference, Swedish Nuclear Power Inspectorate, August 2001

[3] A. Trautwein, W. Gysel: Influence of long-time aging of CF8 and CF8M Cast steel at temperatures between 300 and 500 °C on impact toughness and structural properties, ASTM Symposium on Stainless Steel and Related Alloys, ASTM Special Technical Publication, 756 (1980), 165–189

[4] J. Kwon, J-c. Park, J. Lee, W. Lee, Y-w Park: An investigation of the degradation characteristics for casting stainless steel, CF8M, under high temperatures, Nuclear Engineering and Design, 198 (**2000**), 227–240

[5] Rodney Fordham: The PWR Nuclear Power Station Risk Problem, http://www.cabinet-office.gov.uk, July 2001, 1–6

[6] C. E. Jaske: Process Equipment Fitness for Service Assessments Using API RP 579, Clarion Technical Conferences, Houston, Texas, November 2001, http://www.clarion.org/

[7] S. R. Doctor: Overview of V. C. Summer hot leg loop a nozzle to pipe dissimilar metal weld, SMiRT-16 Conference, U. S. Department of Energy Pacific Northwest National Laboratory, August 2001

[8] A. Mitra et al: Evaluation of magnetic phases in cold worked and weldments of AISI 304 stainless steel, 15-th World Conference of Non Destructive Testing, Rome, Italy, Oct. 2000

[9] M. Vasudevan et al.: Delta ferrite prediction in stainless steel welds using neural network analysis and comparison with other prediction methods, Journal Materials Processing Technology, 142 (**2003**), 20–28

[10] J. Janovec, B. Šuštaršič, J. Medved, M. Jenko: Phases in austenitic stainless steels, Mater. Tehnol., 37 (**2003**) 6, 307-312

[11] B. Šuštaršič, N. Gubeljak, J.V. Tuma: Effect of delta ferrite content on the mechanical properties of cast stainless steel. Rev. Int. Ing. Syst. Prod. Mechan., Metz, France, 10 (**2004**), 48–54.

[12] J. V. Tuma, B. Šuštaršič, F. Vodopivec: The effect of ageing temperature and time on the mechanical properties of Fe-NiCrMo alloys with different contents of delta ferrite, Nucl. Eng. Des., 238 (**2008**) 7, 1511–1517

[13] C. Pokor, C. Pages, B. Marini: Thermal Ageing of cast duplex stainless steels of PWR; material assessment on the removed cast elbows, presentation at CEA-EDF-IMT meeting in the frame of CEA-IMT bilateral collaboration, Saclay, France, January 2008

[14] Determination of Ferrite Content in Austenitic Stainless Steel Castings, International standard ISO/FDIS 13520:2002(E)

[15] Standard practice for steel casting, austenitic alloy, estimating ferrite content thereof, ASTM A800/A800M-01, 2003[16] ISO/FDIS 13520; Determination of ferrite content in austenitic stainless castings, 2002

[16] International standard EN ISO 8249:2000E; Welding-determination of ferrite number (FN) in austenitic and duplex ferritic Cr-Ni stainless steel weld materials, Brussels, 2000

[17] Measurement of the ferrite content in austenitic and duplex steel, feritscope MP 30, Helmut Fischer GmbH&Co, Germany, commercial catalogue, http://www.helmut-fischer.de

[18] B. C. Dodril, B. J. Kelly: Measurement with VSM permanent magnet materials, Lake Shore Cryotronics, Inc., 1999, 1–6

UDK 669.14.018.8:620.191
Original scientific article/Izvirni znanstveni članek

ISSN 1580-2949
MTAEC9, 43(3)137(2009)

THE OXIDATION OF DUPLEX STAINLESS STEEL AT MODERATELY ELEVATED TEMPERATURES

OKSIDACIJA DUPLEKSNEGA NERJAVNEGA JEKLA PRI ZMERNO POVIŠANIH TEMPERATURAH

Črtomir Donik, Aleksandra Kocijan, Irena Paulin, Monika Jenko

Institute of Metals and Technology, Lepi pot 11, SI-1000 Ljubljana, Slovenia
crtomir.donik@imt.si

Prejem rokopisa – received: 2009-03-17; sprejem za objavo – accepted for publication: 2009-05-04

The surface oxidation of DSS 2205 duplex stainless steel was studied by X-ray photoelectron spectroscopy (XPS). Two different techniques were used to produce thin oxide layers on polished and sputter-cleaned duplex stainless-steel samples. These samples were exposed to a 10^{-5} mbar pressure of pure oxygen inside the vacuum chamber and oxidized with an oxygen plasma from room temperature up to 300 °C. The experiments were made with the alloy after a controlled oxidation with oxygen atoms created in an inductively coupled plasma. The experiments were performed in the temperature interval from room temperature up to 300 °C. The compositions of the modified oxidized surfaces were determined from the XPS survey scans, and the chemistry of selected elements from the higher-energy-resolution scans of the appropriate peaks. Various Fe/Cr oxidized layers and various oxide thicknesses were observed and correlated with the temperature. It was found that all the techniques produced oxide layers with various traces of metallic components and with the maximum concentration of chromium oxide and iron oxide in layers close to the oxide-layer–bulk-metal interface.

Key words: duplex stainless steel, oxidation, plasma oxidation, XPS, stainless steel

Z rentgensko fotoelektronsko spektorskopijo (XPS) smo raziskovali površinsko oksidacijo dupleksnega nerjavnega jekla DSS 2205. Z željo, da bi dobili tanke oksidne plasti na atomsko čistih površinah, smo jih oksidirali na dva načina. Vzorci so bili izpostavljeni ali atmosferi čistega kisika v pripravljalni komori pri tlaku 10^{-5} mbar in nato analizirani z XPS ali oksidirani v kisikovi plazmi pri temperaturah od 22 °C do 300 °C. Vse tanke plasti smo preučili z XPS- tehniko za določitev sestave oksidnih plasti na površini. Posebej smo nato pri večji energijski ločljivosti posneli še elemente za natančno določitev spreminjanja skozi oksidno plast, t. i. XPS-globinski profil. Ugotovili smo, da so nastale pri različnih pogojih različne oksidne plasti Fe/Cr različnih debelin v povezavi s temperaturo in načinom oksidacije. Opazili pa smo tudi, da je skoraj pri vseh temperaturah oksidacije ostal tudi delež neoksidiranih kovinskih elementov na površini.

Ključne beside: dupleksno nerjavno jeklo, oksidacija, plazemska oksidacija, XPS, nerjavno jeklo

1 INTRODUCTION

Stainless steel is one of the most widely used materials and has a large variety of applications. Therefore, it is exposed to a wide range of conditions. Since it is an alloy, various oxides can be formed on its surface, and they can change the mechanical, chemical and physical properties of the material. Steel's corrosion resistance originates in the Cr-rich oxide layer that acts as a barrier against ion diffusion between the alloy and the ambient phase.[1–4] Custom steel grades are designed for specific applications by optimizing their properties using specific alloy compositions. The study was on mass fractions 22 % chromium, 5–6 % nickel, 3 % molybdenum, 2 % manganese, nitrogen-alloyed duplex stainless steel (DSS 2205, also known as W.Nr. 1.4462), with high general, localized and stress corrosion resistance properties in addition to high strength and excellent impact toughness. Duplex stainless steels contain two equilibrium phases, i.e., ferrite and austenite. This type of stainless steel is increasingly used because of its several superior properties. It also has better corrosion resistance and erosion-fatigue properties as well as a lower thermal expansion coefficient and higher thermal conductivity than plain austenitic stainless steel. Its yield strength is about twice as high as that of austenitic stainless steels and this allows the designer to save material and makes the alloy more cost competitive in comparison to the 316L or 317L stainless steels. Alloy 2205 is particularly suitable for applications in the temperature interval from –50 °C to 300 °C. Temperatures outside this interval may also be considered, but there are some restrictions, particularly for welded structures.[5,6]

The oxidation and corrosion resistance of stainless steel has already been the subject of many studies. The corrosion resistance of stainless steel is known to be based on the Cr_2O_3 chromium oxide at the surface that is considered to act as a protective layer against corrosion due to its low diffusion constants for oxygen and metal ions.[7,8] The oxide layer formed on stainless-steel surfaces is usually not uniform in terms of the depth. Double or even triple layers can be formed on the surface, depending on the alloy composition, on the oxidizing conditions (oxidizing atmosphere, time, and temperature), and also on the different duplex stainless-steel iron phases.[9,10] Oxide films may theoretically consist of various iron and chromium oxides as well as their

mixtures. Several authors have studied the formation of thin oxide layers on stainless steels, being oxidized in air or oxygen at various pressures and various temperatures. The oxidation in air showed that at most temperatures a duplex oxide layer was formed; the outer layer, α-Fe_2O_3, was formed on the top of the inner oxide layer, an iron-chromium oxide. Under reduced oxygen partial pressures a fine chromium-rich oxide grows through the iron oxide layer that was formed initially. At very low oxygen pressures (below 10^{-3} Pa) and temperatures above 350 °C, chromium predominates throughout the oxide layer [11–15]. At low temperatures, on the other hand, i.e., up to 400 °C, only iron oxide is formed on the surface of stainless steels. This is not true, however, for all the FeCr alloys. Hultquist et al. [16], e.g., reported that a significant fraction of oxidized Cr was detected by the X-ray photoelectron spectroscopy (XPS) of FeCr alloys that were exposed to air at temperatures between 25 °C and 180 °C.

The aim of the present study was to examine the initial phases of oxide growth on the 2205 duplex stainless steel as a function of temperatures up to 300 °C. The oxide layers were produced by the controlled exposure of polished duplex stainless-steel samples to oxygen atoms. X-ray photoelectron spectroscopy (XPS) was applied to measure the depth distributions of the oxide films formed on the surface by the sputter depth profiling. To our knowledge, this is the first report on the depth distribution of oxide-layer compositions on DSS 2205 for the conditions specified in this paper. The results of an ongoing study of the oxidation in air will be described in a subsequent paper.

2 EXPERIMENTAL

Duplex 2205 stainless steel (DSS) was obtained from the Acroni, d. o. o., steel plant, which certified the alloy as 2205 duplex stainless steel with the composition as given in **Table 1**.[2]

The samples were mounted in resin, ground with emery papers up to No. 4000, and then polished with 1-μm diamond paste. Metallographic samples of approximately (8 × 8 × 1) mm were thus prepared. These samples were then mounted onto sample holders for the XPS examinations, using UHV-compatible double-sided sticky tape.

The oxidation was achieved in an experimental reactor for the passivation of metals. The reactor was a glass tube with a length of 40 cm and a diameter of 4 cm. It was evacuated from one side with a two–stage rotary pump with a pumping rate of 16 m^3h^{-1}. The ultimate pressure in the system was about 4 Pa and the residual atmosphere consisted mainly of water vapour. The other end of the reactor was connected to a source of neutral oxygen atoms. The source was a low-pressure oxygen plasma created by an inductively coupled RF generator operating at a frequency of 27.12 MHz and with a variable output power. The applied experimental procedure is described in detail elsewhere.[17–22] In our case the RF power was fixed at about 250 W. The plasma was characterized with a double Langmuir probe and a Fibre Optics Catalytic Probe (FOCP).[17,21,23,24] The Langmuir probe was placed in the centre of the plasma. At the applied pressure of 75 Pa the electron temperature was about 4 eV, while the electron density was about $7 \cdot 10^{15}$ m^{-3}. The FOCP was mounted in the experimental reactor for the passivation of metals close to the samples.[24] At a pressure of 75 Pa the O-atom density reached its peak value of about $1 \cdot 10^{22}$ m^{-3}. The neutral gas kinetics temperature in the passivation reactor was close to room temperature.

The samples were mounted on a heatable holder, heated to the appropriate temperature and kept in the passivation reactor for 100 s. In this period they received a dose of neutral oxygen atoms of about $1.5 \cdot 10^{24}$ m^2.

The XPS depth profiles of the oxide layers were measured with a VG Microlab 310F AES/SEM/XPS. Mg K_α radiation at 1253.6 eV with an anode power of 200 W (the anode voltage was 12.5 kV and the emission current 16 mA) was applied in all the XPS measurements. A 3-keV, 1-μA Ar^+ ion beam scanned over an (8 × 8) mm area was applied for the sputter depth profiling with an incidence angle of 60° (measured with respect to the sample normal). The approximate sputtering rate under the conditions applied here was 1 nm/min for SiO_2. This was not inconsistent with some calibration measurements performed on metallic and oxide-type samples as well as with some reference data for the sputtering rates of Fe and Cr and their oxides.[13,25–29]

The spectra were acquired using the Avantage 3.41v software supplied by the manufacturer. CasaXPS software[30] was used to process the data. The XPS spectra were fitted to determine the different chemical states' contributions to the total peak intensity.

3 RESULTS AND DISCUSSION

Figure 1 shows high-resolution XPS scans of the Cr $2p_{3/2}$ and Fe $2p_{3/2}$ transitions with the corresponding metallic and oxide components before sputtering the DSS 2205 that was prepared at 22 °C. In the case of Cr $2p_{3/2}$ four peaks were used for the fitting, i.e., the metallic peak and the three oxide peaks, CrO_3, Cr_2O_3 and $Cr(OH)_3$. The binding-energy differences of the compo-

Table 2: Chemical composition of the duplex stainless steel in mole fractions *x*/%

Cr	Ni	Mn	Si	P	S	C	Mo	N	Fe
23.96	4.82	1.48	0.85	0.05	0.00	0.13	1.83	0.67	66.21

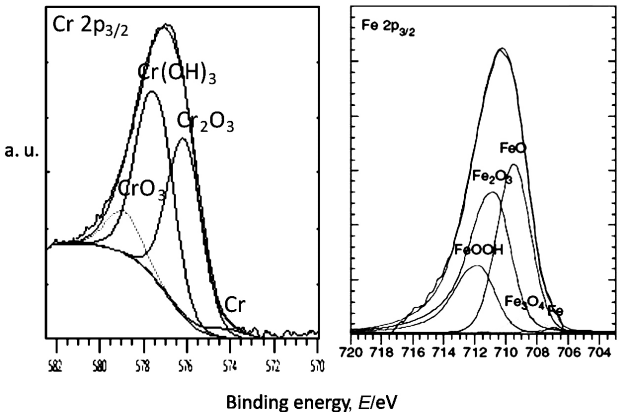

Figure 1: Examples of fitted Cr $2p_{3/2}$, Fe $2p_{3/2}$ XPS spectra
Slika 1: XPS-spektra Cr $2p_{3/2}$, Fe $2p_{3/2}$ z oksidnimi komponentami

nents were fixed at the values obtained from references [7,13,31,32] and the full widths at half maximum (FWHM) for the three oxide peaks were fixed to be the same. The FWHM applied for the metallic component was taken from the Cr peak, being measured after the surface oxides were removed. The expected presence of the three oxides was based on previous work. The Fe $2p_{3/2}$ was fitted with five peaks in a similar way.[6,26,33–39]

Figure 2 shows the Cr $2p_{3/2}$ and $2p_{1/2}$ transitions after various sputtering times for the sample prepared at 22 °C. At each depth the $2p_{3/2}$ peak was fitted as discussed above (see Figure 1). The total Cr oxide concentration was approximated by adding the areas of the three oxide-peak components. The intensities of the oxide components were reduced by sputtering and eventually only the metallic component remained. The Fe data were processed similarly.

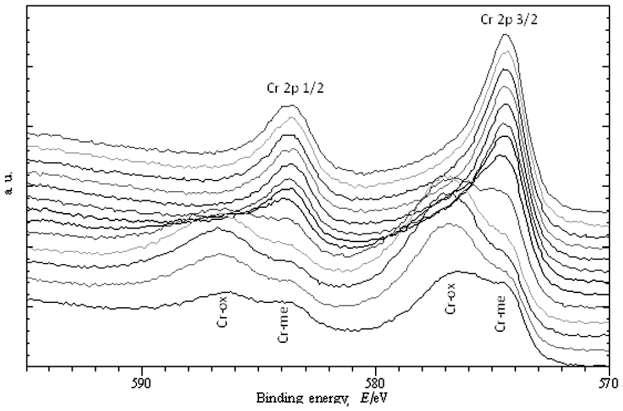

Figure 2: Set of high-resolution XPS spectra of Cr 2p transitions used for constructing the Cr depth profiles in **Figure 3**. The bottom spectrum is from the surface before sputtering, and the spectra above it belong to spots of increased depth from the original surface. The spectra have been offset in intensity for clarity.
Slika 2: Visoko ločljivi XPS-spektri Cr 2p vrha, ki smo jih uporabili za izdelavo globinskih profilov v XPS **sliki 3**. Spodnji spekter je na površini vzorca pred jedkanjem, zgornji spekter pa je po seriji jedkanj. Spektri so zamaknjeni po intenziteti za boljši pregled.

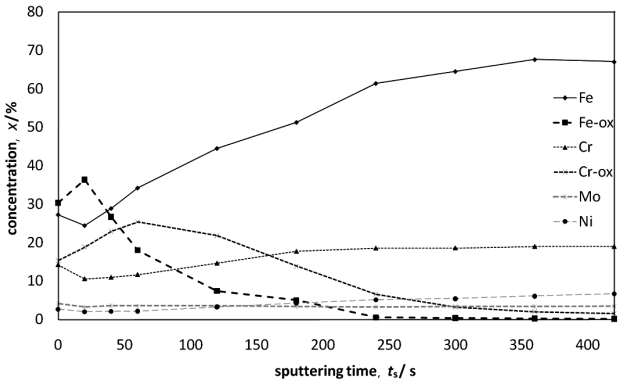

Figure 3: XPS depth profile of DSS at 200 L exposure in the preparation chamber
Slika 3: XPS; globinski profil DSS pri izpostavljenosti 200 L v pripravljalni komori

Figure 3 shows an XPS depth profile of the oxide layer after the oxidation of the DSS 2205 with an exposure to 200 L (Langmuir) of oxygen in the preparation chamber. The stoichiometry of the oxide was, in the best case, an approximation because of the ion-sputtering-induced effects, such as the reduction of the oxidation state.

XPS depth profiles were also measured with the DSS 2205 after much longer exposures to oxygen, i.e., up to 8000 L (**Figure 4**), without obtaining substantially different results. This suggested that an increase in the pressure and/or different atmospheric conditions, e.g., humidity, were needed to produce a thicker oxide layer.

The profiles in **Figures 3 and 4** showed that these oxide layers were ill-defined with slowly changing concentrations of oxidized and unoxidized metals from the surface of the oxide layer towards the interior of the sample. Also, large fractions of unoxidized metals were present at the very surface of the oxide layers. These concentrations might be partially overestimated since the estimations of oxide-layer thicknesses obtained from the profiles in **Figures 3 and 4** were 2–3 nm, i.e., of the order of the probing depth of the applied XPS in the

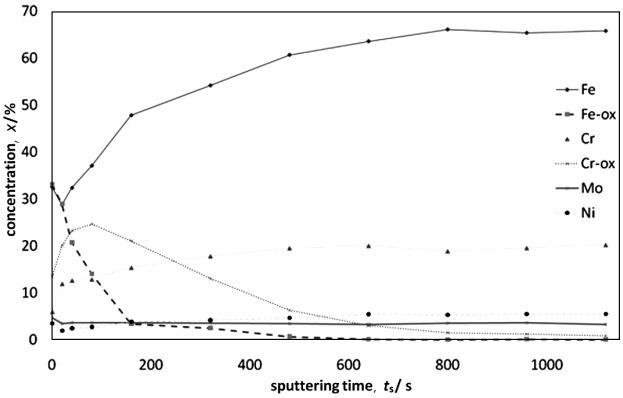

Figure 4: XPS depth profile of DSS at 8000 L exposure in the preparation chamber
Slika 4: XPS; globinski profil DSS pri izpostavljenosti 8000 L v pripravljalni komori

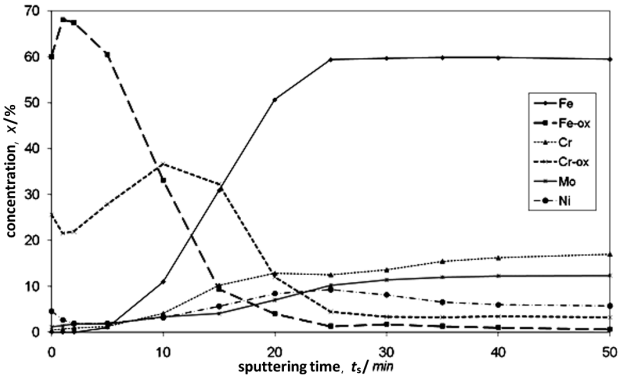

Figure 5: XPS depth profile of DSS oxidized at 22 °C
Slika 5: XPS; globinski profil DSS po oksidaciji v plazmi pri 22 °C

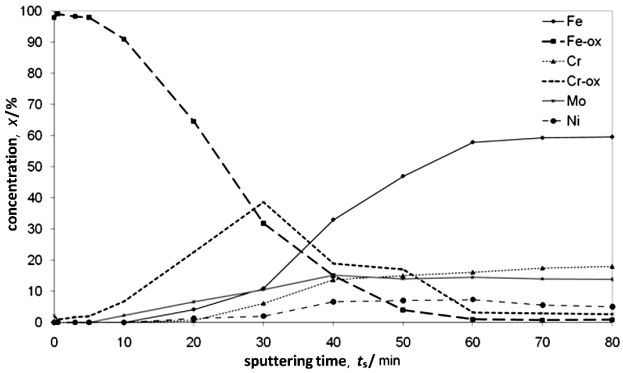

Figure 7: XPS depth profile of DSS oxidized at 300 °C
Slika 7: XPS; globinski profil DSS po oksidaciji v plazmi pri 300 °C

analysis, so there existed some possibility that unoxidized metals from the bulk influenced the measurements. Even in those poorly defined oxide layers, two-oxide structures could already be detected: a higher concentration of iron oxide at, and close to, the surface, with chromium oxide being the predominant oxide at greater depths, in contrast to the layer of the bulk interface.

The stoichiometry of the oxide was, in the best case, an approximation due to ion-sputtering-induced effects, such as the reduction of the oxidation states.[16,27,28,40] However, valid comparisons could be made between the relative oxidation degrees at various temperatures. The formation of an oxide film with an inner region, essentially consisting of chromium oxide, and an outer region, mainly consisting of iron oxide, was also observed in the samples that were heated up to 300 °C. A. P. Greeff et al.[41] found that the formation of Fe_2O_3 on the FeCrMo steel was, in the interval between room temperature and 300 °C, more rapid than that of the initially formed Cr_2O_3, and it was eventually formed on the top of the Cr-oxide. This is in agreement with our results. The concentration of the unoxidized metallic species in the topmost part of the oxide layer was much lower than the concentration of their oxidized counterparts, while there was virtually no unoxidized chromium or iron in the oxide layer. **Figure 6** shows a different metal-oxide distribution for the sample that was

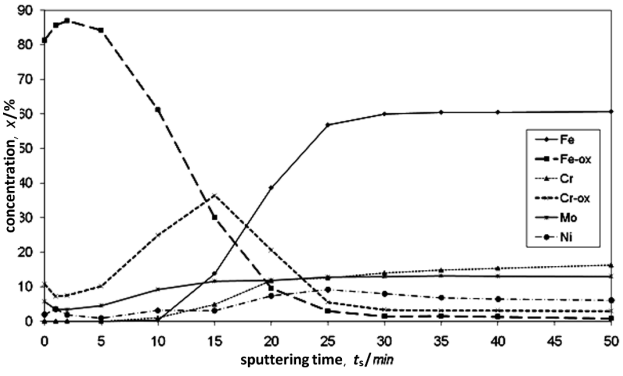

Figure 6: XPS depth profile of DSS oxidized at 150 °C
Slika 6: XPS; globinski profil DSS po oksidaciji v plazmi pri 150 °C

oxidized at a higher temperature of 150 °C (423 K). The concentration of iron oxides close to the surface was, in this case, much higher than that in the sample oxidized at 22 °C (**Figure 5**), being about mole fraction x = 85 % compared to the previous value of about mole fraction of x = 70 %, and it showed the segregation of iron oxides at the surface. On the other hand, the concentration of chromium oxides was about x = 10 %, compared to x = 25 %, showing the reduced surface segregation of Cr (oxides) at 150 °C . The thickness of the oxide layer was also somewhat greater than that formed with plasma oxidation at room temperature and very much thicker than that formed with just pure oxygen. In both cases, the amount of chromium oxides increased at the interface between the surface oxides and the underlying steel. **Figure 7** shows the XPS depth profile of DSS oxidized at 300 °C (573 K). The further increase of iron oxides and the further reduction of chromium oxides in the oxide film were quite dramatic compared to the depth profiles of the samples being oxidized at lower temperatures, as well as the increased thickness of the oxide layer itself. Other effects observed in the sputter depth profiles at 22 °C and 150 °C (**Figures 5 and 6**) remained unchanged, i.e., the increased concentration of chromium oxides at the interface of the oxide layer and steel substrate. A comparison of **Figures 5, 6 and 7** makes it clear that the total oxide layer was thicker, and the ratio of the iron oxides to chromium oxides increased with increasing oxidation temperature (up to 300 °C). However, it was observed that the amount of chromium oxides increased at the interface of the surface oxide layers and substrate to approximately $x \approx 35$ % in all cases. It is known, as a general rule, that iron oxide is the predominant surface oxide in stainless steels at temperatures up to 400 °C,[9] and this research showed the actual temperature dependence of this predominant species within the mentioned temperature range. The composition and oxidation behaviour of the various grains was known to be very similar, and the XPS analysis was made on a 1 mm × 2 mm area that was much greater than the grain size.

An enrichment with Mo throughout the oxide layer was observed at all temperatures. The oxide layer of DSS had a duplex structure of Fe oxides, predominantly Fe_2O_3, on the outer side and Cr oxides, predominantly Cr_2O_3, on the inner side of layer, with an enrichment of Mo underneath the Cr oxide layer. This enrichment of Mo might be explained by the assumption that Mo oxidizes less readily than Fe or Cr. The Gibbs free energies for the formation of Fe_2O_3, Cr_2O_3 and MoO_3 at 700 K (427 °C) are – 979 J/mol, – 1209 J/mol and – 799 J/mol, respectively, and they correspond to – 744,8 J/mol, – 807,5 J/mol and – 535,5 J/mol O_2. From the viewpoint of thermodynamics, the oxidation of Mo is the least favourable. Furthermore, according to Mathieu and Landolt [5], the presence of Mo at the oxide/metal interface could influence the oxide growth in two ways: Mo could reduce the activity of Fe at the phase boundary or it could form a diffusion barrier for Fe and Cr ions between the oxide and the metal.

In summary, the oxidation of DSS 2205 with atomic oxygen revealed two important factors that influenced the growth and composition of the oxide layers that were formed at various temperatures, i.e., the segregation of the alloying elements to the surface and the influence of atomic oxygen on the oxidation process.

4 CONCLUSIONS

Two different types of oxide layers were obtained. The first one was very thin, of the order of 2–5 nm, obtained with exposure to oxygen at 10^{-5} mbar, independent of the total exposure time, even when the exposure times differed by two orders of magnitude. The second one was of the order of a few tenths of nm, obtained by exposure to plasma oxidation, also at higher temperatures. A more detailed analysis showed that despite the great similarities between the samples that were oxidized either with oxygen or with plasma there were also differences in certain numerical parameters (e.g., the ratios of unoxidized versus oxidized iron, or metal in general) that allowed us to denote the plasma-oxidized sample as a more "thoroughly" oxidized. A common characteristic of all the examined layers was a double-oxide stratification, with the regions closer to the surface that contained higher concentrations of iron oxide, and those more towards the interior, exhibiting higher concentrations of chromium oxide. The compositions of the oxide films formed on the DSS 2205 by exposure to plasma oxygen atoms are presented from room temperature to 300 °C. Different oxide layers were formed on the surface, depending on the temperature during the atomic oxidation. Small increments of temperature above room temperature resulted in increased amounts of Fe oxides and reduced amounts of Cr oxides on the surface, while almost pure Fe oxides were formed at 300 °C. There was an enrichment of chromium oxides at the interface between the surface oxide and the bulk material at all the temperatures. Due to this Cr enrichment at the interface, the upper part of the bulk material consisted of the so-called chromium-depleted layer. This study also provided important results about the behaviour of the DSS 2205 that was treated with oxygen atoms from relatively low temperatures up to just 300 °C. To examine this advanced exposure a chamber with the possibility of increasing the exposure pressure, measured in mbars, could be used. Another possibility for further studies is to use ARXPS for more accurate depth profiling of the thinnest oxide layers.

5 REFERENCES

[1] G. Betz, G. K. Wehner, L. Toth, Journal of Applied Physics 45 (**1974**), 5312–5316

[2] ASM specialty handbook: Stainless Steels, 1996, 32–34

[3] M. Veljkovic, J. Gozzi, Journal of Pressure Vessel Technology-Transactions of the ASME 2007, 129, 155–161 10.1115/1.2389034

[4] S. Ohkido, Y. Ishikawa, T. Yoshimura, POSAP analysis of the oxide alloy interface in stainless-steel, 1994, Chapter, 261–265

[5] H. J. Mathieu, D. Landolt, Corrosion Science 26 (**1986**), 547–559

[6] C. Palacio, H. J. Mathieu, V. Stambouli, D. Landolt, Surface Science 295 (**1993**), 251–262

[7] C. M. Abreu, M. J. Cristobal, X. R. Novoa, G. Pena, M. C. Perez, Surface and Interface Analysis 2008, 40, 294–298 10.1002/sia.2796

[8] H. Asteman, K. Segerdahl, J. E. Svensson, L. G. Johansson, M. Halvarsson, J. E. Tang, p. trans tech, In: Oxidation of stainless steel in H2O/O-2 environments – Role of chromium evaporation, 2004, Chapter, 775–782

[9] A. Vesel, A. Drenik, M. Mozetic, A. Zalar, M. Balat-Pichelin, M. Bele, In: AES investigation of the stainless steel surface oxidized in plasma, 2007, Chapter, 228–231

[10] A. Vesel, M. Mozetic, A. Drenik, N. Hauptman, M. Balat-Pichelin, Applied Surface Science 255 (**2008**), 1759–1765 10.1016/j.apsusc.2008.06.017

[11] Y. Ishikawa, K. Odaka, Reduction of outgassing from stainless surfaces by surface oxidation, 1990, Chapter, 1995–1997

[12] Y. Ishikawa, T. Yoshimura, Journal of Vacuum Science & Technology a-Vacuum Surfaces and Films 13 (**1995**), 1847–1852

[13] A. Kocijan, C. Donik, M. Jenko, Corrosion Science 49 (**2007**), 2083-2098 10.1016/j.corsci.2006.11.001

[14] S. Shibagaki, A. Koga, Y. Shirakawa, H. Onishi, H. Yokokawa, J. Tanaka, Thin Solid Films 303 (**1997**), 101–106

[15] G. J. Stokkers, A. Vansilfhout, G. A. Bootsma, T. Fransen, P. J. Gellings, Corrosion Science 23 (**1983**), 195–204

[16] G. Hultquist, M. Seo, N. Sato, Oxidation of Metals 25 (**1986**), 363–372

[17] U. Cvelbar, M. Mozetic, A. Ricard, Characterization of oxygen plasma with a fiber optic catalytic probe and determination of recombination coefficients, ed. by Editor, City, 2005, Chapter, 834–837

[18] U. Cvelbar, M. Mozetic, Journal of Physics D-Applied Physics 2007, 40, 2300–2303 10.1088/0022–3727/40/8/s09

[19] U. Cvelbar, K. Ostrikov, A. Drenik, M. Mozetic, Applied Physics Letters 92 (**2008**), 133505 10.1063/1.2905265

[20] A. Drenik, U. Cvelbar, K. Ostrikov, M. Mozetic, Journal of Physics D-Applied Physics 41 (**2008**), 115201 10.1088/0022-3727/41/11/115201

[21] M. Mozetic, A. Zalar, U. Cvelbar, D. Babic, AES characterization of thin oxide films growing on Al foil during oxygen plasma treatment, 2004, Chapter, 986–988

[22] M. Mozetic, U. Cvelbar, A. Vesel, N. Krstulovic, S. Milosevic, Ieee Transactions on Plasma Science 36 (**2008**), 868–869 10.1109/tps.2008.925383

[23] U. Cvelbar, M. Mozetic, I. Poberaj, D. Babib, A. Ricard, Characterization of hydrogen plasma with a fiber optics catalytic probe, 2005, 12–16
[24] M. Mozetic, Characterization of reactive plasmas with catalytic probes, 2007, Chapter, 4837–4842
[25] J. R. Lince, S. V. Didziulis, D. K. Shuh, T. D. Durbin, J. A. Yarmoff, Surface Science 277 (**1992**), 43–63
[26] D. Mandrino, M. Godec, M. Torkar, M. Jenko, Surface and Interface Analysis 40 (**2008**), 285–289 10.1002/sia.2718
[27] N. S. McIntyre, F. W. Stanchell, Journal of Vacuum Science & Technology 16 (**1979**), 798–802
[28] A. Zalar, Thin Solid Films 124 (**1985**), 223–230
[29] A. Kocijan, I. Milosev, D. K. Merl, B. Pihlar, Journal of Applied Electrochemistry 34 (**2004**), 517–524
[30] N. Fairley, http://www.casaxps.com/
[31] A. Maetaki, M. Yamamoto, H. Matsumoto, K. Kishi, Surface Science 445 (**2000**), 80–88
[32] A. Kocijan, I. Milosev, B. Pihlar, Journal of Materials Science-Materials in Medicine 15 (**2004**), 643–650
[33] Dj. Mandrino, M. Jenko A study of oxide layers on electrical steels prepared with different thermal treatments, 2001, Chapter, 157–161
[34] Dj. Mandrino, M. Godec, P. Skraba, B. Sustarsic, M. Jenko, AES, XPS and EDS analyses of an iron-based magnetic powder and an SMC material, 2004, Chapter, 912–916
[35] Dj. Mandrino, M. Lamut, M. Godec, M. Torkar, M. Jenko, Surface and Interface Analysis 39 (**2007**), 438–444 10.1002/sia.2534
[36] J. Baltrusaitis, D. M. Cwiertny, V. H. Grassian, Physical Chemistry Chemical Physics 9 (**2007**), 5542–5554 10.1039/b709167b
[37] C. R. Brundle, T. J. Chuang, K. Wandelt, Surface Science 68 (**1977**), 459–468
[38] A. P. Grosvenor, B. A. Kobe, M. C. Biesinger, N. S. McIntyre, Surface and Interface Analysis 36 (**2004**), 1564–1574 10.1002/sia.1984
[39] E. Paparazzo, Journal of Electron Spectroscopy and Related Phenomena 154 (**2006**), 38–40 10.1016/j.elspec.2006.09.004
[40] C. Leygraf, G. Hultquist, Surface Science 61 (**1976**), 69–84
[41] A. P. Greeff, C. W. Louw, H. C. Swart, Corrosion Science 42 (**2000**), 1725–1740

UDK 621.791.05
Original scientific article/Izvirni znanstveni članek

ISSN 1580-2949
MTAEC9, 43(3)143(2009)

OPTIMIZATION OF WELD BEAD GEOMETRY IN TIG WELDING PROCESS USING GREY RELATION ANALYSIS AND TAGUCHI METHOD

OPTIMIZACIJA GEOMETRIJE TIG-VARKOV Z GREYJEVO ANALIZO IN TAGUCHIJEVO METODO

Ugur Esme[1], Melih Bayramoglu[2], Yugut Kazancoglu[3], Sueda Ozgun[4]

[1]Mersin University Tarsus Technical Education Faculty Department of Mechanical Education, 33140 Mersin-Tarsus, Turkey
[2]Cukurova University Engineering and Architecture Faculty, Department of Mechanical Engineering, 01330 Balcali-Adana, Turkey
[3]Izmir University of Economics, Sakarya cad. 156, Balcova-Izmir, Turkey
[4]Mersin University Vocational School of Gulnar, 33400 Gulnar-Mersin, Turkey
uesme2003@hotmail.com

Prejem rokopisa – received: 2009-01-26; sprejem za objavo – accepted for publication: 2009-02-17

This study investigated the multi-response optimization of tungsten inert gas welding (TIG) welding process for an optimal parametric combination to yield favorable bead geometry of welded joints using the Grey relational analysis and Taguchi method. Sixteen experimental runs based on an orthogonal array of Taguchi method were performed to derive objective functions to be optimized within experimental domain. The objective functions have been selected in relation to parameters of TIG welding bead geometry; bead width, bead height, penetration, area of penetration as well as width of heat affected zone and tensile load. The Taguchi approach followed by Grey relational analysis to solve the multi-response optimization problem. The significance of the factors on overall quality characteristics of the weldment has also been evaluated quantitatively by the analysis of variance method (ANOVA). Optimal results have been verified through additional experiments. This shows application feasibility of the Grey relation analysis in combination with Taguchi technique for continuous improvement in product quality in manufacturing industry.

Keywords: TIG welding; Grey relation analysis; Tensile test

Predstavljeni so rezultati optimizacije odgovorov pri varjenju v inertni atmosferi z volframovo elektrodo (TIG) za dosego optimalne geometrije varka z uporabo analize po Greyju in Taguchijevi metodi. Šestnajst eksperimentalnih varkov je bilo nanesenih v ortogonalni razporeditvi po Taguchijevi metodi, da bi določili parametre, ki jih je treba eksprimentalno optimirati. Ti parametri, izbrani v povezavi s parametri TIG-varjenja, so: geometrija varka, širina varka, višina varka, penetracija, površina penetracije, širina toplotne zone in natezna obremenitev. Taguchijevemu približku je sledila Greyjeva racionalna analiza zaradi optimizacije več odgovorov pri problemu optimizacije. Pomen dejavnikov za karakteristike splošne kakovosti zvarov je kvantitativno ocenjen z analizo po meodi variance (ANOVA). Optimalne rezultate smo verificirali z dodatnimi poskusi. To kaže na možnost uporabe Greyjeve analize v kombinaciji s Taguchijevo tehniko za stalno rast kakovosti v predelovalni industriji.

Ključne besede: TIG-varjenje, Greyjeva analiza, natezni preizkus

1 INTRODUCTION

In today's manufacturing world, quality is of vital importance. Quality can be defined as the degree of customer's satisfaction as provided by the procured product. The product quality depends on the desired requirements gained in the product that suits its functional requirements in various areas of application.

In the field of welding, weld quality mainly depends on the mechanical properties of the weld metal and heat affected zone (HAZ), which in turn is influenced by metallurgical characteristics and chemical compositions of the weld.

Moreover, these mechanical-metallurgical features of the weldment depend on the weld bead geometry, which are directly related to welding process parameters. In other words, weld quality depends on welding process parameters [1].

Tungsten inert gas (TIG) welding is a multi-objective and multi-factor metal fabrication technique. Several process parameters interact in a complex manner resulting direct or indirect influence on weld bead geometry, mechanical properties and metallurgical features of the weldment as well as on the weld chemistry. Basically, TIG weld quality is strongly characterized by the weld bead geometry as shown in **Figure 1**.

Bead geometry variables; heat affected zone, bead width, bead height, penetration and area of penetration are greatly influenced by welding process parameters; welding speed, welding current, shielding gas flow rate and gap distance and also it plays an important role in

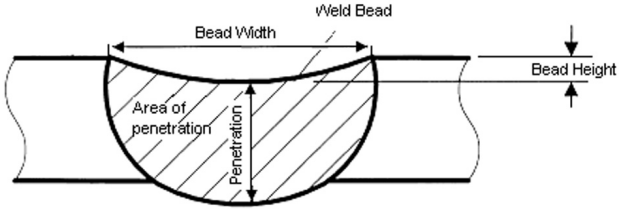

Figure 1: Weld bead geometry
Slika 1: Geometrija varka

determining the mechanical properties of the weld such as Tensile load.

It is necessary to find an optimal process condition capable of producing desired weld quality. However, this optimization should be performed in such a way that all the objectives should fulfill simultaneously. Such an optimization technique is called multi-response optimization.

Literature shows that work has been explored on various aspects of modeling, simulation and process optimization in TIG welding. In this study, detailed analysis has been made to establish relationships between welding parameters and weld bead geometry and weld quality leading to an optimal process.

Saurav Datta and et al. [1] developed a grey-based Taguchi method for multi-response optimization of bead geometry in submerged arc bead-on-plate welding process. Jackson and Shrubsall [2] performed optimization, neural networks and regression analysis in submerged arc welding process. Xie Yan-Min and et al. [3] used grey relational analysis for optimizing the square hole flanging process parameters with considerations of the multiple response characteristics. Lin and Lin [4] studied on the use of the grey-fuzzy logic based on orthogonal array for optimizing the electrical discharge machining process with multi-response characteristics. Murugan et al. [5], developed mathematical models using a five-level factorial technique to predict the weld bead geometry for depositing 316L stainless steel onto structural steel IS2062. Gunaraj and Murugan [6] determined the main and interaction effects of process control variables on important bead geometry parameters including bead volume quantitatively and represented the results graphically in submerged arc welding process.

The Taguchi method is very popular for solving optimization problems in the field of production engineering, Yang et al. [7], Rowlands et al. [8]. The method utilizes a well-balanced experimental design (allows a limited number of experimental runs) called orthogonal array design, and signal-to-noise ratio (S/N ratio), which serve the objective function to be optimized (maximized) within experimental domain. However, traditional Taguchi method cannot solve multi-objective optimization problem. To overcome this, the Taguchi method coupled with Grey relational analysis has a wide area of application in manufacturing processes. This approach can solve multi-response optimization problem simultaneously [1,9].

Planning the experiments through the Taguchi orthogonal array has been used quite successfully in process optimization by Chen and Chen [10], Fung and Kang [11], Tang et al. [12], Vijian and Arunachalam [13], Yang [14] as well as Zhang et al. [15]. Therefore, this study applied a Taguchi $L_{16}(4^4)$ orthogonal array to plan the experiments on TIG welding process. Four controlling factors including welding speed (V), welding current (I), shielding gas flow rate (F) and gap distance (G) with four levels for each factor were selected. The Grey relational analysis is then applied to examine how the welding process factors influence the bead geometry; bead width (BW), bead height (BH), penetration (P), area of penetration (AP) and heat affected zone (HAZ), as well as tensile load (TL). An optimal parameter combination was then obtained. Through analyzing the Grey relational grade matrix, the most influential factors for individual quality targets of TIG welding process can be identified. Additionally, the analysis of variance (ANOVA) was also utilized to examine the most significant factors for the bead geometry in TIG welding process.

2 GREY RELATIONAL ANALYSIS

2.1 Data Preprocessing

In Grey relational analysis, experimental data i.e., measured features of quality characteristics are first normalized ranging from zero to one. This process is known as Grey relational generation. Next, based on normalized experimental data, Grey relational coefficient is calculated to represent the correlation between the desired and actual experimental data. Then overall Grey relational grade is determined by averaging the Grey relational coefficient corresponding to selected responses [1]. The overall performance characteristic of the multiple response process depends on the calculated Grey relational grade. This approach converts a multiple response process optimization problem into a single response optimization situation with the objective function is overall Grey relational grade. The optimal parametric combination is then evaluated which would result highest Grey relational grade. The optimal factor setting for maximizing overall Grey relational grade can be performed by Taguchi method [1].

In Grey relational generation, the normalized HAZ, BW and BH corresponding to the smaller-the-better (SB) criterion which can be expressed as:

$$x_i(k) = \frac{\max y_i(k) - y_i(k)}{\max y_i(k) - \min y_i(k)} \tag{1}$$

TL, P and AP should follow the larger-the-better (LB) criterion, which can be expressed as:

$$x_i(k) = \frac{y_i(k) - \min y_i(k)}{\max y_i(k) - \min y_i(k)} \tag{2}$$

where $x_i(k)$ is the value after the Grey relational generation, min $y_i(k)$ is the smallest value of $y_i(k)$ for the k^{th} response, and max $y_i(k)$ is the largest value of $y_i(k)$ for the k^{th} response. An ideal sequence is $x_0(k)$ (k = 1, 2, 3, ..., 16) for the responses. The definition of Grey relational grade in the course of Grey relational analysis is to reveal the degree of relation between the 16 sequences [$x_0(k)$ and $x_i(k)$, i = 1, 2, 3, ...,16]. The Grey relational coefficient $\xi_i(k)$ can be calculated as:

$$\xi_i(k) = \frac{\Delta_{\min} - \psi\Delta_{\max}}{\Delta_{0i}(k) + \psi\Delta_{\max}} \quad (3)$$

where $\Delta_{0i} = ||x_0(k) - x_i(k)||$ difference of the absolute value $x_0(k)$ and $x_i(k)$; ψ is the distinguishing coefficient $0 \le \psi \le 1$; $\Delta_{\min} = \forall j^{\min} \in i \forall k^{\min} ||x_0(k) - x_i(k)||$ = the smallest value of Δ_{0i}; and $\Delta_{\max} = \forall j^{\max} \in i \forall k^{\max} ||x_0(k) - x_i(k)||$ = largest value of Δ_{0i}. After averaging the Grey relational coefficients, the Grey relational grade γ_i can be computed as:

$$\gamma_i = \frac{1}{n}\sum_{k=1}^{n} \xi_i(k) \quad (4)$$

where n is the number of process responses. The higher value of Grey relational grade corresponds to intense relational degree between the reference sequence $x_0(k)$ and the given sequence $x_i(k)$. The reference sequence $x_0(k)$ represents the best process sequence; therefore, higher Grey relational grade means that the corresponding parameter combination is closer to the optimal. The mean response for the Grey relational grade with its grand mean and the main effect plot of Grey relational grade are very important because optimal process condition can be evaluated from this plot [1].

3 EXPERIMENTAL PROCEDURE AND TEST RESULTS

3.1 Experimental Details

The experiments were conducted according to the design matrix at random order to avoid systematic errors infiltrating the system. Weld beads were laid on the joint to join 1.2 mm AISI 304 thin stainless steel plate with the dimensions of (25 × 240) mm. The chemical composition of the workpiece material is given in **Table 1**.

Table 1: Composition (%) of AISI 304 steel workpiece
Tabela 1: Sestava (%) vzorca jekla AISI 304

C	Mn	P	S	Si	Cr	Mo	Ni	Cu
0.08	2.00	0.04	0.030	1.00	19	0.20	10.5	0.02

Fronius Variostar WTU 305 type arc welding machine was used in the experiments. The specimens were joined using a single pass butt welding with AWS A 5.12-80 EW Th-2 thoriated tungsten electrode and pure argon (99.99 %) as shielding gas.

The experimental set up was designed and constructed to control the linear movement of the torch along the weld pad center line. The welded joints were sectioned to produce specimens for examining the quality parameters (BW, BH, P and AP) of weld bead shape in the welded specimens. These specimens were prepared by the usual metallurgical polishing methods and etched with Marble's etching reagent ($CuSO_4$ + HCl + H_2SO_4). Macrographs were then taken for each cross section using stereo microscope with 50X lens. In macro examinations of the specimens, Motic stereo microscope with image capture device mounted on top of the lens section of the microscope was used.

The weld bead profile was outlined by using Image-pro Plus 4.5 and NIH ImageJ software. The spatial calibrations were made on the macrographs before the measurement. The line drawings of the bead profiles were then used to take measurements on UW, UH, P, AP and HAZ.

Tensile load values were recorded from tensile testing of the specimens prepared in accordance with the EN 895 Standard. Tensile test specimens were taken from the weld bead according to the transverse tensile test method. Tensile test specimens were prepared in such a way that the weld zones were centered in the gage length. At the same time, heat affected zone was placed in the gage length perpendicular to the weld.

3.2 Process Parameters and Test Results

In full factorial design, the number of experimental runs exponentially increases as the number of factors as well as their level increases. This results huge experimentation cost and considerable time [1]. So, in order to compromise these two adverse factors and to search the optimal process condition through a limited number of experimental runs Taguchi's $L_{16}(4^4)$ orthogonal array consisting of 16 sets of data has been selected to optimize the multiple performance characteristics of TIG welding bead geometry.

Experiments have been conducted with the process parameters given in **Table 2**, to obtain butt welding on AISI 304 1.2 mm thickness stainless steel plate with 25 mm × 240 mm dimensions by TIG welding process.

Table 2: Process parameters and their limits
Tabela 2: Parametri procesov in njihove limite

Parameters	Notation	Unit	Levels of factors			
			1	2	3	4
Travel speed	*V*	mm/s	1.06*	1.99	2.31	3.55
Current	*I*	A	40*	55	70	85
Gas flow rate	*F*	L/min	8*	10	12	14
Gap distance	*G*	mm	1.5*	2	2.5	3

*Initial factor settings

Table 3 shows the selected design matrix based on Taguchi $L_{16}(4^4)$ orthogonal array consisting of 16 sets of coded conditions and the experimental results for the responses of TL, HAZ, BW, BH, P and AP. All these data have been utilized for analysis and evaluation of optimal parameter combination required to achieve desired quality weld in terms of bead geometry within the experimental domain.

Table 3: Orthogonal array $L_{16}(4^4)$ of the experimental runs and results
Tabela 3: Ortogonalna porazdelitev L_{16} (4^4) eksperimentalnih varkov in rezultatov

Run no	Process parameters				Experimental results					
	V	*I*	*F*	*G*	TL (N)	HAZ (mm)	BW (mm)	BH (mm)	P (mm)	AP (mm^2)
1	1	1	1	1	11429	5.255	7.383	0.185	1.098	7.809
2	1	2	2	2	11870	6.204	8.391	0.230	1.190	8.899
3	1	3	3	3	12047	7.077	9.253	0.265	1.258	9.848
4	1	4	4	4	11772	7.874	9.972	0.291	1.302	10.654
5	2	1	2	3	11576	3.985	6.840	0.114	1.060	6.948
6	2	2	1	4	12066	4.895	7.835	0.118	1.130	7.704
7	2	3	4	1	12213	5.344	7.840	0.162	1.213	8.078
8	2	4	3	2	12606	6.172	9.017	0.183	1.265	9.072
9	3	1	3	4	11282	3.649	6.432	0.112	1.006	6.453
10	3	2	4	3	11625	4.343	6.880	0.125	1.107	7.022
11	3	3	1	2	12508	5.157	8.115	0.126	1.195	7.970
12	3	4	2	1	12753	5.714	8.670	0.159	1.245	8.514
13	4	1	4	2	9270	2.931	4.459	0.096	0.887	4.695
14	4	2	3	1	10006	3.573	5.304	0.097	1.017	5.429
15	4	3	2	4	10281	4.405	6.201	0.107	1.039	6.033
16	4	4	1	3	10448	4.955	6.670	0.099	1.133	6.481

4 PARAMETRIC OPTIMIZATION OF TIG WELDING PROCESS

4.1 Evaluation of Optimal Process Condition

First, by using Eqs. (1) and (2), experimental data have been normalized to obtain Grey relational generation. The normalized data and Δ_{0i} for each of the responses of bead geometry as well as TL and HAZ have been furnished in **Table 4** and **Table 5** respectively. For TL, P and AP larger-the-better (LB) and for HAZ, BW, BH smaller-the-better (SB) criterion has been selected.

Table 4: Grey relational generation of each performance characteristics
Tabela 4: Generiranje Greyjeve odvisnosti za vsako značilno perfomanco

Run no	TL	P	AP	HAZ	BW	BH
	Larger-the-better			*Smaller-the-better*		
Ideal sequence	1	1	1	1	1	1
1	0.620	0.509	0.523	0.530	0.470	0.544
2	0.746	0.730	0.706	0.338	0.287	0.312
3	0.797	0.593	0.300	0.161	0.130	0.131
4	0.718	1.000	1.000	0.000	0.000	0.000
5	0.662	0.417	0.378	0.787	0.568	0.908
6	0.803	0.586	0.505	0.603	0.388	0.886
7	0.846	0.785	0.568	0.512	0.387	0.663
8	0.958	0.911	0.735	0.344	0.173	0.552
9	0.577	0.286	0.295	0.855	0.642	0.918
10	0.676	0.529	0.391	0.714	0.561	0.852
11	0.930	0.741	0.550	0.550	0.337	0.848
12	1.000	0.862	0.641	0.437	0.236	0.679
13	0.000	0.000	0.000	1.000	1.000	1.000
14	0.211	0.314	0.123	0.870	0.847	0.997
15	0.291	0.365	0.225	0.702	0.684	0.947
16	0.338	0.593	0.300	0.590	0.599	0.986

Table 5: Evaluation of Δ_{0i} for each of the responses
Tabela 5: Ocena Δ_{0i} za vsak odgovor

Run no	TL	P	AP	HAZ	BW	BH
Ideal sequence	1	1	1	1	1	1
1	0.380	0.491	0.477	0.470	0.530	0.456
2	0.254	0.270	0.294	0.662	0.713	0.688
3	0.203	0.407	0.700	0.839	0.870	0.869
4	0.282	0.000	0.000	1.000	1.000	1.000
5	0.338	0.583	0.622	0.213	0.432	0.092
6	0.197	0.414	0.495	0.397	0.612	0.114
7	0.154	0.215	0.432	0.488	0.613	0.337
8	0.042	0.089	0.265	0.656	0.827	0.448
9	0.423	0.714	0.705	0.145	0.358	0.082
10	0.324	0.471	0.609	0.286	0.439	0.148
11	0.070	0.259	0.450	0.450	0.663	0.152
12	0.000	0.138	0.359	0.563	0.764	0.321
13	1.000	1.000	1.000	0.000	0.000	0.000
14	0.789	0.686	0.877	0.130	0.153	0.003
15	0.709	0.635	0.775	0.298	0.316	0.053
16	0.662	0.407	0.700	0.410	0.401	0.014

Table 6 shows the calculated Grey relational coefficients (with ψ = 0 of each performance characteristic using Eq. (3).

Table 6: Grey relational coefficient of each performance characteristics ($\psi = 0$)
Tabela 6: Koeficient Greyjeve relacije za karakteristike vsake performance($\psi = 0$)

Run no	TL	P	AP	HAZ	BW	BH
Ideal sequence	1	1	1	1	1	1
1	0.568	0.504	0.512	0.515	0.485	0.523
2	0.664	0.649	0.629	0.430	0.412	0.421
3	0.711	0.551	0.417	0.373	0.365	0.365
4	0.640	1.000	1.000	0.333	0.333	0.333
5	0.597	0.462	0.446	0.701	0.537	0.845
6	0.717	0.547	0.503	0.557	0.449	0.815
7	0.765	0.699	0.536	0.506	0.449	0.597
8	0.922	0.848	0.653	0.433	0.377	0.528
9	0.542	0.412	0.415	0.775	0.583	0.859
10	0.607	0.515	0.451	0.636	0.532	0.772
11	0.877	0.659	0.526	0.526	0.430	0.767
12	1.000	0.784	0.582	0.470	0.396	0.609
13	0.333	0.333	0.333	1.000	1.000	1.000
14	0.388	0.422	0.363	0.794	0.765	0.993
15	0.413	0.441	0.392	0.626	0.613	0.904
16	0.430	0.551	0.417	0.550	0.555	0.974

The Grey relational coefficients, given in **Table 7**, for each response have been accumulated by using Eq. (4) to evaluate Grey relational grade, which is the overall representative of all the features of weld quality. Thus, the multi-criteria optimization problem has been transformed into a single equivalent objective function optimization problem using the combination of Taguchi approach and Grey relational analyses. Higher is the value of Grey relational grade, the corresponding factor combination is said to be close to the optimal [1].

Table 7: Grey relational grade
Tabela 7: Razred Greyjeve relacije

Run no	Grey relational grade	Rank
1	0.5180	15
2	0.5342	14
3	0.4637	16
4	0.6066	6
5	0.5977	8
6	0.5980	7
7	0.5922	10
8	0.6268	4
9	0.5975	9
10	0.5855	11
11	0.6307	3
12	0.6402	2
13	0.6667	1
14	0.6208	5
15	0.5650	13
16	0.5794	12

Table 8 shows the S/N ratio based on the larger-the-better criterion for overall Grey relational grade calculated by using Eq. (5).

$$S/N = -10\lg\left[\frac{1}{n}\sum_{i=1}^{n}\frac{1}{y_i^2}\right] \quad (5)$$

where n is the number of measurements, and y_i is the measured characteristic value.

Table 8: S/N ratio for overall Grey relational grade
Tabela 8: Razmerje S/N za splošno Grayjevo odvisnost

Run no	S/N
1	–5.71
2	–5.45
3	–6.68
4	–4.34
5	–4.47
6	–4.47
7	–4.55
8	–4.06
9	–4.47
10	–4.65
11	–4.00
12	–3.87
13	–3.52
14	–4.14
15	–4.96
16	–4.75

Table 9: Response table for the mean Grey relational grade
Tabela 9: Tabela odgovorov za povprečje odvisnosti Greyjevega razreda

Factors	Grey relational grade				
	Level 1	Level 2	Level 3	Level 4	Max-Min
V	0.53	0.60	0.61	0.61	0.08
I	0.59	0.58	0.56	0.61	0.05
F	0.58	0.58	0.58	0.61	0.03
G	0.59	0.61	0.56	0.59	0.05

Total mean Grey relational grade is 0.59.

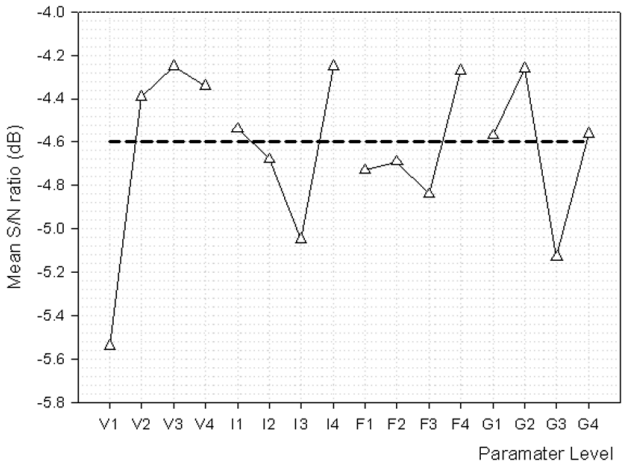

Figure 2: S/N ratio plot for the overall Grey relational grade
Slika 2: S/N odvisnost za splošno Greyjevo relacijo

Graphical representation of S/N ratio for overall Grey relational grade is shown in **Figure 2**. The dashed line is the value of the total mean of the S/N ratio.

As indicated in **Figure 2**, the optimal condition for 1.2 mm AISI 304 stainless steel becomes $V_3I_4F_4G_2$. **Table 9** shows the mean Grey relational grade ratio for each level of the process parameters.

4.2 Analysis of Variance (ANOVA)

The purpose of the analysis of variance (ANOVA) is to investigate which welding parameters significantly affect the performance characteristic. This is accomplished by separating the total variability of the grey relational grades, which is measured by the sum of the squared deviations from the total mean of the grey relational grade, into contributions by each welding parameters and the error. Thus;

$$SS_T = SS_F + SS_e \quad (6)$$

where

$$SS_T = \sum_{j=1}^{p} (\gamma_j - \gamma_m)^2 \quad (7)$$

and

SS_T Total sum of squared deviations about the mean
γ_j Mean response for j^{th} experiment
γ_m Grand mean of the response
p Number of experiments in the orthogonal array
SS_F Sum of squared deviations due to each factor
SS_e Sum of squared deviations due to error

In addition, the F test was used to determine which welding parameters have a significant effect on the performance characteristic. Usually, the change of the welding parameter has a significant effect on the performance characteristic when the F value is large. ANOVA for overall Grey relational grade is shown in **Table 10**.

Table 10: ANOVA results
Tabela 10: ANOVA-rezultati

Parameter	Degree of Freedom	Sum of Square	Mean Square	F	Contribution (%)
V	3	0.0180	0.006109	4.42	52.41
I	3	0.00529	0.001765	1.28	15.40
F	3	0.00312	0.001042	0.75	9.09
G	3	0.00691	0.002305	1.67	20.12
Error	3	0.00102	0.000346	-	2.97
Total	15	0.03434			100

Result of the ANOVA indicates that the welding speed (52.41 % contribution) is the most effective parameter on the responses under the multi criteria optimization (higher tensile load, penetration, area of penetration and lower heat affected zone, bead width, bead height). The percent contributions of other parameters are gap distance (20.12 %), current (15.40 %) and shielding gas flow rate (9.09 %).

4.3 Confirmation Test

After evaluating the optimal parameter settings, the next step is to predict and verify the enhancement of quality characteristics using the optimal parametric combination. The estimated Grey relational grade $\hat{\gamma}$ using the optimal level of the design parameters can be calculated as:

$$\hat{\gamma} = \gamma_m + \sum_{i=1}^{o} (\bar{\gamma}_i - \gamma_m) \quad (8)$$

where γ_m is the total mean Grey relational grade, $\bar{\gamma}_i$ is the mean Grey relational grade at the optimal level, and o is the number of the main design parameters that affect the quality characteristics. **Table 11** shows the comparison of the predicted bead geometry parameters as well as TL and HAZ with that of actual by using the optimal TIG welding conditions; good agreement between the actual and predicted results have been observed (improvement in overall Grey relational grade).

Table 11: Results of confirmation test
Tabela 11: Rezultati potrditvenega poskusa

	Initial factor settings	Optimal process condition	
		Prediction	Experiment
Factor levels	$V_1I_1F_1G_1$	$V_3I_4F_4G_2$	$V_3I_4F_4G_2$
TL	1165		1285
P	1.098		1.226
AP	7.809		8.518
HAZ	5.255		5.747
BW	7.383		8.569
BH	0.185		0.152
S/N ratio of overall Grey relational grade	−5.71	−3.14	−1.60
Overall Grey relational grade	0.52	0.69	0.83
Improvement in Grey relational grade is 0.31			

In Taguchi method, the only performance feature is the overall Grey relational grade; and the aim should be to search a parameter setting that can achieve highest overall Grey relational grade. The Grey relational grade is the representative of all individual performance characteristics. In this study, objective functions have been selected in relation to parameters of bead geometry as well as TL and HAZ; and all the responses have been given equal weight age. The results showed that using optimal parameter setting ($V_3I_4F_4G_2$) caused higher P, AP and TL.

5 CONCLUSION

Taguchi method is a very effective tool for process optimization under limited number of experimental runs. Essential requirements for all types of welding are deeper penetration with higher tensile load and lower heat affected zone, bead height and bead width for reducing weld metal consumption. This study has

concentrated on the application of Taguchi method coupled with Grey relation analysis for solving multi criteria optimization problem in the field of tungsten inert gas welding process. Experimental results have shown that the tensile load, heat affected zone and penetration, area of penetration, heat affected zone, bead width and bead height of the weld bead in the TIG welding of stainless steel are greatly improved by using Grey relation analysis in combination with Taguchi method.

6 REFERENCES

[1] S. Datta, A. Bandyopadhyay, P. K. Pal, Int J Adv Manuf Technol., 39 (**2008**), 1136–1143

[2] C. E. Jackson, A. E. Shrubsall, Weld J., 32 (**1953**), 172–178

[3] Y. M. Xie et al., Journal of Zhejiang University Science A, 8 (**2007**), 805–811

[4] J. L. Lin, C. L. Lin, J Mater Process Technol., 160 (**2005**), 9–14

[5] N. Murugan, R. S. Paramar, S. K. Sud, J Mater Process Technol., 37 (**1993**), 767–780

[6] V. Gunaraj, N. Murugan, Weld J., (**2000**), 286–294

[7] W. H. Yang, Y. S. Tarng, J Mater Process Technol., 84 (**1998**), 122–129

[8] H. Rowlands, J. Antony, G. Knowles, The TQM Magazine, 12 (**2000**), 78–83

[9] S-H. Lim, C-M. Lee, W.J. Chung, International Journal of Precision Engineering and Manufacturing, 7 (**2006**), 18–23

[10] D. C. Chen, C. F. Chen, J. Mater Process Technol., 190 (**2007**), 130–137

[11] C. P. Fung, P.C. Kang, J. Mater. Process Technol., 170 (**2005**), 602–610

[12] S. H. Tang, V. J. Tan, S.M. Sapuan, S. Sulaiman, N. Ismail, R. Samin, J Mater Process Technol., 182 (**2007**), 418–426

[13] P. Vijian, V.P. Arunachalam, J Mater Process Technol., 180 (**2006**), 161–166

[14] L. J. Yang, J Mater Process Technol., 185 (**2007**), 113–119

[15] J. Z. Zhang, J. C. Chen, E. D. Kirby, J Mater Process Technol., 184 (**2007**), 233–239

UDK 006.91:543.5
Original scientific article/Izvirni znanstveni članek

ISSN 1580-2949
MTAEC9, 43(3)151(2009)

PRIMARY ETALONNAGE OF NEGATIVE GAUGE PRESSURES USING PRESSURE BALANCES AT THE CZECH METROLOGY INSTITUTE

PRIMARNE KALIBRACIJSKE METODE ZA NEGATIVNI RELATIVNI TLAK S TLAČNIMI TEHTNICAMI NA ČEŠKEM INŠTITUTU ZA METROLOGIJO

Jiří Tesař, Zdeněk Krajíček, Dominik Pražák, František Stanček

Czech Metrology Institute, Okružní 31, 638 00 Brno, Czech Republic
dprazak@cmi.cz

Prejem rokopisa – received: 2008-04-14; sprejem za objavo – accepted for publication: 2008-08-23

This paper summarizes the methods of using the piston pressure balance principle for the etalonnage of negative gauge pressures, i.e., the classical piston pressure balance with an inversed piston cylinder or working under an evacuated bell jar, digital non-rotating piston pressure balances and an absolute pressure divider. It describes the principles of their use (focusing on their utilization at the Czech Metrology Institute), the methods of traceability and analyzes their achievable uncertainties.

Keywords: negative gauge pressure, pressure balance, traceability

V članku so predstavljene različne metode z batnimi tlačnimi tehtnicami za umerjanje merilnikov negativnega tlaka, tj. klasične batne tlačne tehtnice z obrnjenim sklopom bat-valj ali z evakuirano zvonasto posodo, digitalne batne tlačne tehtnice z nevrtečim se batom in z delilnikom absolutnega tlaka. Opisan je princip dela s poudarkom na njihovi rabi na Češkem inštitutu za metrologijo, načini sledljivosti in analiza dosegljivih merilnih negotovosti.

Ključne besede: merilnik negativnega pritiska, tlačna tehtnica, sledljivost

1 INTRODUCTION

The etalonnage of negative gauge pressures is a very much neglected branch of primary metrology (although very important in practice). This peripheral position is documented by the fact that no Key Comparison has ever been performed in this range. The only such comparisons known to the authors were organized at the national level, e.g. [1,2]. Simultaneously, the use of piston pressure balances as the primary standards of negative gauge pressure leads to very interesting constructions. The Laboratory of Pressure Metrology of the Czech Metrology Institute intends to ensure this pressure range via piston pressure balances.

In this paper the values of the negative gauge pressure P_{ng} will be positive and all the uncertainties will be unexpanded ($k = 1$).

2 CLASSICAL PRESSURE BALANCES

Pressure balances can also be utilized for the primary etalonnage of negative low pressures [3]. There are three basic set-ups enabling this. Firstly, an **inverse piston-cylinder** design; secondly, the utilization of an **evacuated bell jar**; and thirdly, an **absolute pressure balance with a reference pressure monitor,** enabling the calculation of the negative gauge pressure from their pressure difference (not discussed further in this article).

The first solution is based on a piston cylinder that is vertically reversed (**Figure 1**). It is held in its floating position by the atmospheric pressure P_a acting upwards, balancing the residual pressure P acting downwards on the piston together with the force F that is the sum of the gravitational forces acting on the piston and the loaded masses. So, the generated negative gauge pressure is given by the following equation:

$$P_{ng} = P_a - P = \frac{M\left(1 - \frac{\rho_a}{\rho_M}\right)g}{A_{ef}(p, T)} \quad (1)$$

where:

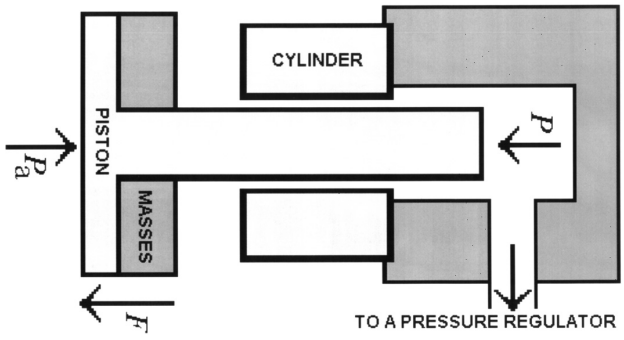

Figure 1: The inverse piston-cylinder design
Slika 1: Prikaz delovanja obrnjenega sklopa bat-valj

A_{ef} (p,T) is the effective area of the piston cylinder that is generally dependent on the acting pressure p and its temperature T,

M is the total mass of the piston and the masses loaded on it,

ρ_M is the average density of the piston and the masses,

ρ_a is the density of the ambient air,

g is the local acceleration due to gravity.

In practice, the piston cylinder is mounted on tubing, enabling it to be calibrated in the gauge mode in the normal position and then turned down and utilized for negative gauge pressures. This solution, however, brings about certain restrictions. For the range up to 100 kPa generated by a piston cylinder with a nominal effective area of 10 cm^2 (widely used in this range of gauge pressures) a total mass of 10 kg is needed, which introduces design complications. This is solved by inverse piston cylinders with a nominal effective area of 1 cm^2, which, on the other hand, reduce the sensitivity.

The second solution is based on a classical piston-cylinder design working under a bell jar (**Figure 2**). This is normally used for working in the absolute mode when the space under the bell jar is evacuated (and the residual pressure is measured with a suitable vacuum meter). In this case, however, the ambient atmospheric pressure is applied under the piston, while under the bell jar such an absolute pressure is set in order to balance (together with the pressure defined by the piston cylinder) the atmospheric pressure. So the generated negative gauge pressure is given as:

$$P_{ng} = P_a - P = \frac{M\left(1-\frac{\rho_g}{\rho_M}\right)g}{A_{ef}(p,T)} \qquad (2)$$

where ρ_g is the density of the gas pressure medium under the bell.

The second solution is very useful because it is possible to utilize a piston manometer in a reversed set-up of its absolute mode, only with the possibility to employ piston cylinders with large effective areas. However, there are also certain disadvantages. The space beneath the vacuum bell jar has a large volume that requires a very skilled operator. Another task is to accurately determine the density of the gas under the bell jar. Furthermore, for measuring the low negative gauge pressures, it is necessary to evacuate the bell jar first in order to reach an efficient sealing level, and only then is it possible to return to low negative gauge pressures.

The laboratory utilizes the classical DHI PG7601 piston gauge [4,5] with a piston cylinder 10 cm^2 in the mode described above. It is also equipped with an automated mass-handling system and automated pressure regulators. This system was developed for work in the absolute mode, but the laboratory also utilizes it in the negative gauge mode with very satisfactory results.

The simple free-deformation piston cylinders are utilized in this mode. Dadson and Sutton's model of an effective area of a piston cylinder also depends on the pressure distribution along the gap and the viscosity and density of the pressure medium used as functions of the pressure. It would therefore be necessary to evaluate the effective area not only for various working modes (absolute, gauge, negative gauge) but also for various generated pressure points. Numerical and experimental studies have proven that these changes never exceed 0.0002 %, which is negligible.

The calculation of the uncertainty of the negative gauge pressure generated by the above-mentioned piston cylinder is based on equation (2). The effective area value and its uncertainty $u_{A_{ef}}$ were obtained from geometrical measurements using Dadson and Sutton's model [3] and were confirmed by the hydrostatic cross-floating method, both in absolute and gauge modes. The

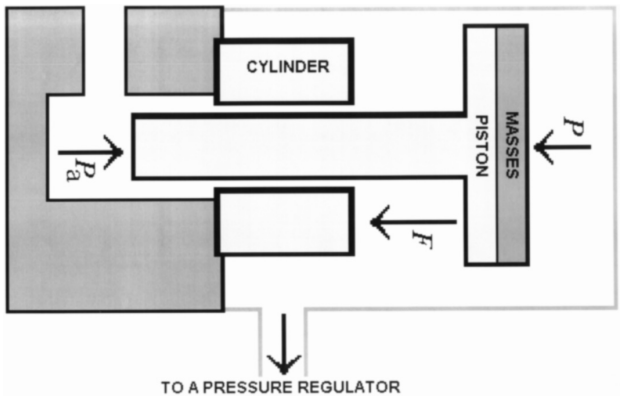

Figure 2: Principle of utilizing a bell to measure negative gauge pressures

Slika 2: Prikaz rabe zvonaste posode za merjenje negativnega pritiska

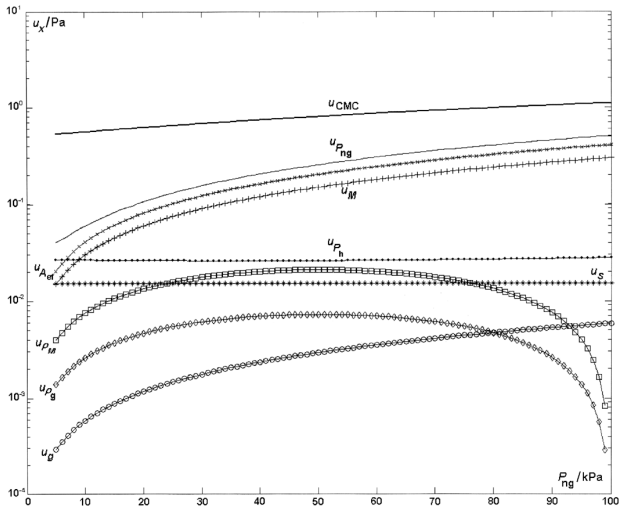

Figure 3: The influence of the uncertainties of all the input quantities on the total uncertainty of the negative gauge pressure generated by a classical pressure balance with an evacuated bell jar

Slika 3: Vpliv negotovosti vseh vstopnih veličin na skupno merilno negotovost negativnega pritiska, ki ga generiramo s klasično batno tlačno tehtnico z evakuirano zvonasto posodo

pressure-deformation coefficient of the piston cylinder can be omitted in this pressure range, but the influence of its thermal expansion must be taken into account. The second most important contribution to the total uncertainty is the uncertainty of the mass u_M. The influence of the uncertainty of the density of the gas under the vacuum bell jar $u_{\rho g}$ has been a source of relatively high uncertainty and so pure nitrogen has been introduced as the pressure medium. Its density values are tabulated in [6] with a precision 0.01 %. The influence of the head-pressure uncertainty u_{Ph} depends on the difference between the reference levels, which is usually very small, but an exaggerated value of 25 cm was used here. The correlations between $u_{\rho g}$ and the uncertainty of the acceleration due to gravity u_g that also appear in the calculation of u_{Ph} were neglected. The remaining sources of uncertainty are the uncertainties of the mass density $u_{\rho M}$ and the sensitivity u_s. The graph in **Figure 3** shows the influence of the uncertainties of all the input quantities on the total uncertainty of the generated negative gauge pressure u_{Png} and compares it with the internationally accepted measurement capability of the Czech Republic u_{CMC} = 0.5 Pa + 0.0006 % of the measured value in the range from 5 kPa to 100 kPa [7].

3 DIGITAL PRESSURE BALANCES

The measurement of small pressure differences and low absolute pressures using a classical piston manometer with a rotating piston has two basic limitations. First, it is only possible to measure pressures that are high enough to balance the mass of the piston (a few kilopascals). Second, the periodic pressure fluctuations caused by rotation of the piston that have amplitudes of the order of tenths of a pascal are an important source of uncertainty in low-pressure measurements. A solution based on the connection of a non-rotating piston to an electronic dynamometer can measure even very small changes of the state of equilibrium of the piston. It also

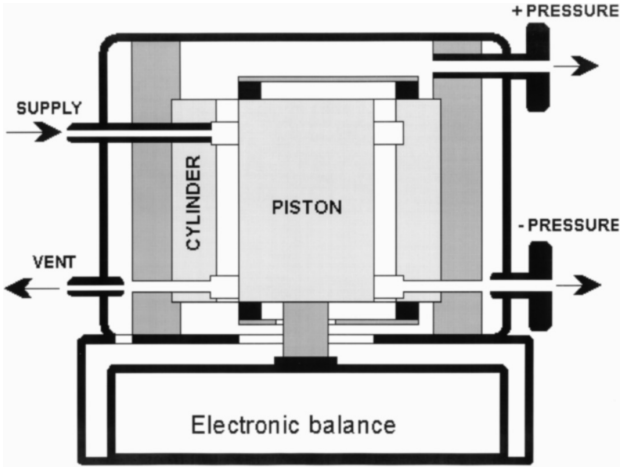

Figure 4: Digital non-rotating piston manometer FRS 4 HR
Slika 4: Digitalni nerotirajoči batni manometer FRS 4 HR

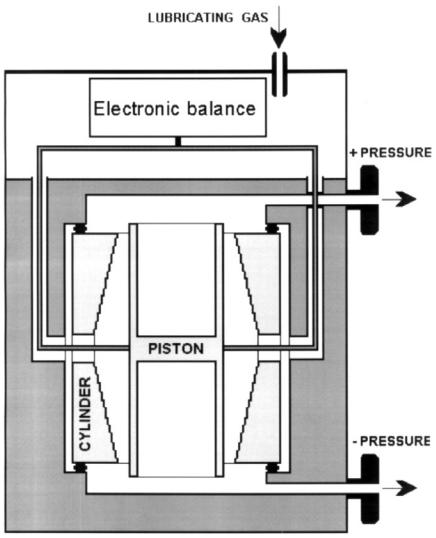

Figure 5: Digital non-rotating piston manometer DHI FPG 8601
Slika 5: Digitalni nerotirajoči batni manometer DHI FPG 8601

offers the possibility to use a larger effective area of the piston cylinder.

The laboratory uses an improved, commercially available Furness Controls FRS 4 HR standard able to work in differential, gauge and (reversing the outputs) also negative gauge modes [8]. The nominal area of the piston is 100 cm^2, and the width of the gap is approximately 30 μm. The electronic balance can be calibrated using an external mass before every measurement. The friction between the piston and the cylinder is prevented by a lever mechanism (**Figure 4**), allowing axial movement of the piston without any contact with the surface of the cylinder.

The flow of dry air enters the upper part of the cylinder during the measurement. This air then flows through the gap and exits through the outputs in the base. The system was highly sensitive to small instabilities of atmospheric pressure. It was therefore decided to use mass-flow controllers in the input and output instead of the flow-controlling unit in order to insulate the instrument's ports from the ambient and to stabilize and control the gas flow (i.e., the pressure difference).

This instrument has made it possible to ensure the etalonnage of the negative gauge pressure in the range from 1 Pa to 3.2 kPa. The internationally accepted measurement capability of the Czech Republic u_{CMC} = 0.01 Pa + 0.004 % of the measured value [7].

Figure 5 introduces the DHI FPG 8601 manometer [9–12]. It is based on a non-rotating tungsten-carbide piston 10 cm^2 placed in a tungsten-carbide cylinder, where the gap has a 1-to-6 μm conical profile. The piston is centred by means of a lubricating gas with a pressure that is about 40 kPa higher than the reference pressure and is balanced by a mass comparator (electronic balance). The pressure and the gas flow are regulated by a control unit equipped with two flowmeters (for coarse and fine adjustments), and also a PC. The attainable uncertainty

in the negative gauge mode in the range from 1 Pa to 15 kPa is $u_{P_{ng}}$ = 0.01 Pa + 0.0014 % of the measured value.

This instrument was evaluated using primary methods and compared with a classical pressure balance, both in gauge (evaluating number E_n up to 0.4) and in absolute (E_n up to 0.3) modes. Both the digital non-rotating piston pressure balances were also compared mutually in the gauge mode (E_n up to 0.6).

4 ABSOLUTE PRESSURE DIVIDER

The principle of this standard is the same as in the classical pressure divider [13]. It is based on three concentric pistons (A, B and C). The effective area of the piston B is 101-times larger than that of the pistons A and C (**Figure 6**). The pressure generated by an oil-piston manometer is connected to the base of piston C. Due to the ratio of the effective areas of the piston cylinders of the divider, the increase in the pressure above piston B is nominally 100-times lower than the increase in the hydraulic pressure under piston C. There is a vacuum pump connected via an insulating valve to the lower chamber beneath piston B. The device under test is also connected to the lower chamber.

The DH-Budenberg 1600 absolute pressure divider can be used to generate absolute, gauge, negative gauge and differential (at line pressures other than atmospheric) pressures. The work in the negative gauge mode is as follows. First, the spaces under and over the central piston B are opened to the atmosphere. Such masses must be put on the oil-piston manometer in order to generate an appropriate pressure with a magnitude of approximately 1 MPa, acting on the base of piston C and compensating for the gravity of the rotating piston system. After reaching an equilibrium state of the oil-piston standard and the divider, the valve connecting the lower chamber to the atmosphere can be closed. Now, an additional mass must be placed onto the oil-piston manometer to generate an increase in the hydraulic pressure 100-times higher than is the demanded negative gauge pressure value. This will increase the pressure upwards acting on the base of piston C, i.e., on the piston system of the divider, and raise this system in the upper stroke. Then the lower chamber is evacuated until the demanded negative gauge pressure is reached. Consequently, the vacuum pump is disconnected by the valve and the hydraulic pressure is trimmed in order to ensure the middle floating position of the piston system of the divider.

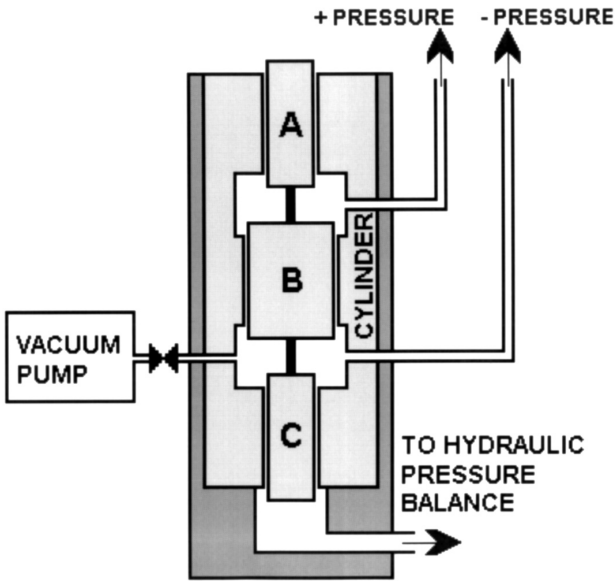

Figure 6: Principle of the absolute pressure divider
Slika 6: Prikaz delovanja absolutnega delilnika tlaka

Since the effective area of piston B is nominally 101-times larger than that of pistons A and C, the ratio of the hydraulic and the differential pressure (dividing ratio) is nominally:

$$R_D = \frac{\Delta p_o}{p_{ng}} = \frac{A_B - A_C}{A_C} = \frac{101-1}{1} = 100 \qquad (3)$$

where:
Δp_o is the change in hydraulic pressure
A_C is the effective area of piston C
A_B is the effective area of piston B

The hydraulic pressure at the time of the initial equilibrium is defined as:

$$p_o = \frac{m\left(1-\frac{\rho_{a0}}{\rho_m}\right)+\sigma c}{A_o(p_o, T_{o0})} + h\rho_o g \qquad (4)$$

where:
m is the total applied mass by initial equilibrium
ρ_m is the mean density of the piston and loaded masses
A_o is the effective area of the hydraulic pressure piston cylinder
T_{o0} is the temperature of the hydraulic pressure piston cylinder during initial equilibrium
ρ_{a0} is the density of ambient atmosphere during initial equilibrium
c is the piston circumference at its exit from the oil
σ is the surface-tension coefficient of the oil
ρ_o is the density of the oil
h is the height of the piston base above the reference level

The change in the hydraulic pressure (caused by the additional mass m_p) can be written as:

$$\Delta p_o = \frac{(m_p + m)\left(1-\frac{\rho_a}{\rho_m}\right)g+\sigma c}{A_o(p_o, T_{o0}+\Delta p_o)} - \frac{m\left(1-\frac{\rho_{a0}}{\rho_m}\right)g+\sigma c}{A_o(p_o, T_{o0})} \qquad (5)$$

where ρ_a is the density of the ambient atmosphere and T_o is the temperature upon generating the differential pressure.

The generated negative gauge pressure is:

$$p_{\mathrm{ng}} = \frac{1}{R_{\mathrm{D}}}\left[\frac{(m_p + m)\left(1 - \frac{\rho_{\mathrm{a}}}{\rho_m}\right)g + \sigma c}{A_{\mathrm{o}}(p_{\mathrm{o}}, T_{\mathrm{o}0} + \Delta p_{\mathrm{o}})} - \frac{m\left(1 - \frac{\rho_{\mathrm{a}0}}{\rho_m}\right)g + \sigma c}{A_{\mathrm{o}}(p_{\mathrm{o}}, T_{\mathrm{o}0})}\right] \quad (6)$$

The following notation that simplifies the previous equation is used for the purpose of analysing the uncertainty:

$$P_{\mathrm{ng}} = \frac{1}{R_{\mathrm{D}}}\left[P_{\mathrm{o}} - C\right] \quad (7)$$

The graph in **Figure 7** shows the influence of the uncertainties of all the input quantities on the total uncertainty of the generated negative gauge pressure $u_{P\mathrm{ng}}$. The major influences come from the uncertainty of the dividing ratio $u_{R\mathrm{D}}$ and the component $u_{R\mathrm{o}}$, followed by the sensitivity u_{s} and the component u_{C}. The influence of the head-pressure uncertainty $u_{P\mathrm{h}}$ depends on the difference between the reference levels (again, an exaggerated value of 25 cm was used). The correlations between $u_{P\mathrm{o}}$, u_{C} and $u_{P\mathrm{h}}$ were neglected. The resultant uncertainty (for negative gauge pressures higher than 1 kPa) can be approximated by $u_{P\mathrm{ng}}$ = 0.15 Pa + 0.0027 % of the measured value.

5 TRACEABILITY OF THE ABSOLUTE PRESSURE DIVIDER

The traceability of the pressure divider is composed of two items. First, it is the traceability of the hydraulic pressure balance, which is trivial. Second, it is the traceability of the dividing ratio that was performed with the national standard in the gauge pressure (up to 450 kPa, see **Figure 8**). The dividing ratio is, in general, dependent on the pressure, but this can be neglected in the negative gauge mode. The obtained value R_{D} = (99.997 ± 0.005) is in agreement with the value obtained three years before R_{D} = (99.998 ± 0.005).

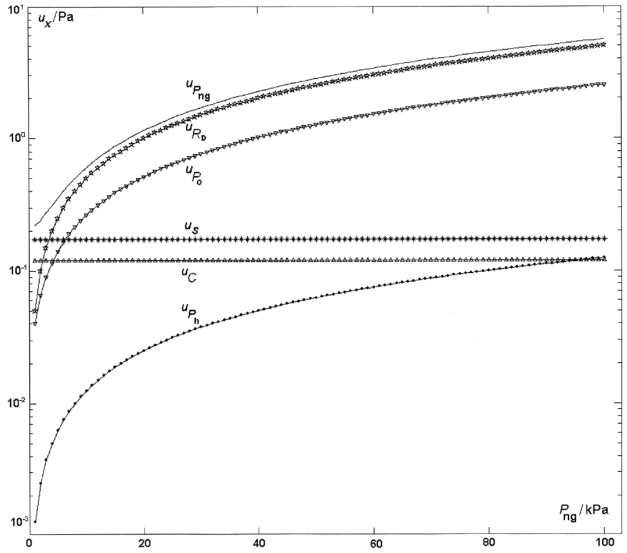

Figure 7: Influence of the uncertainties of all the input quantities on the total uncertainty of the negative gauge pressure generated by the absolute pressure divider
Slika 7: Vpliv negotovosti vseh vstopnih veličin na skupno merilno negotovost negativnega pritiska, ki ga generiramo z absolutnim delilnikom tlaka

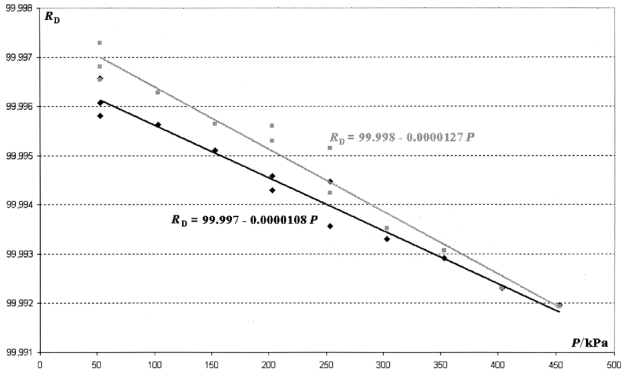

Figure 8: Results of the traceability of the dividing ratio in the gauge mode for the years 2007 (diamonds) and 2004 (squares)
Slika 8: Rezultati sledljivosti razmerja delitve za relativni tlak v letu 2007 (rombi) in 2004 (kvadrati)

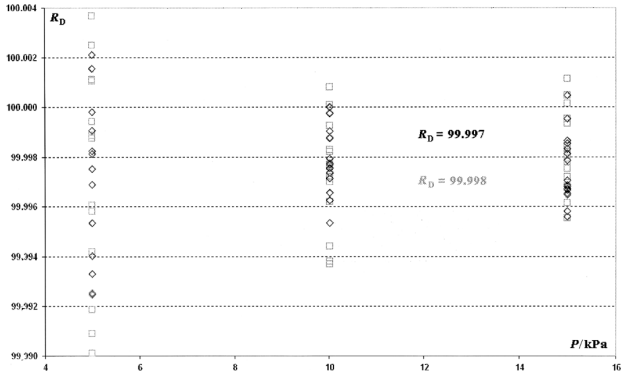

Figure 9: Results of the traceability of the dividing ratio in the absolute mode for the years 2007 (diamonds) and 2004 (squares)
Slika 9: Rezultati sledljivosti razmerja delitve za absolutni tlak v letu 2007 (rombi) in 2004 (kvadrati)

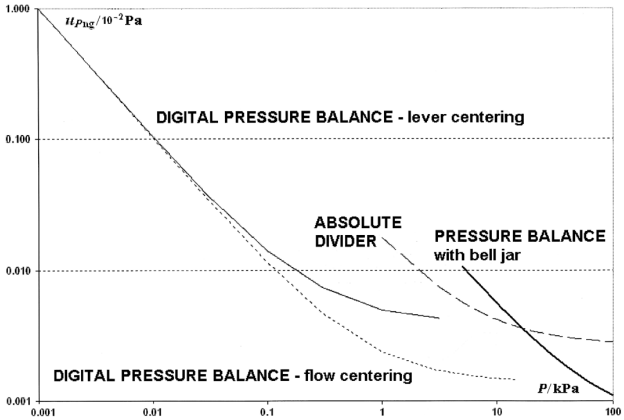

Figure 10: Uncertainties attainable via different methods
Slika 10: Primerjava merilne negotovosti različnih metod

In order to be sure that the dividing ratio is not influenced by the working mode its traceability in the absolute mode was also performed. The above-mentioned DHI FPG8601 digital non-rotating piston manometer served as a standard for this (**Figure 9**). The measured pressure points were (5, 10 and 15) kPa. In this case the result was R_D = (99.997 ± 0.007), and three years before it was also R_D = (99.998 ± 0.007).

Furthermore, the comparison in the negative gauge mode between the absolute divider and the classical piston manometer, the digital non-rotating piston manometer with flow centring and the digital non-rotating piston manometer with lever centring was performed. The instruments were separated by a zero indicator (MKS 1 torr Baratron). The comparisons with the digital non-rotating piston-pressure balances gave worse results at the lower ends of their ranges, where the noise is higher. The comparison with the classical piston-pressure balances also gave worse results at the lower end of its range (problems with the free rotation time of the piston), but also at the higher end (problems with the regulation of the pressure). However, the evaluation number was lower than one in each case.

6 CONCLUSION

Utilization of the classical piston gauge operating under a bell jar for the etalonnage of negative gauge pressures is a useful and cost-effective solution. **Figure 10** shows a comparison of the attainable uncertainties of all of the mentioned instruments. The Czech Metrology Institute seems to be the only case in the CMC tables covering the negative gauge pressure range using such a principle. The problems it brings have been solved to a satisfactory degree. On the other hand, the use of the absolute divider for this range is much faster, and with only an insignificant (for typical calibrations) decrease in the uncertainty. Moreover, it enables a comparison of classical and digital pressure balances in the negative gauge range.

7 REFERENCES

[1] M. Rantanen, S. Semenoja, Intercomparison in gauge pressure range from –95 kPa to +100 kPa, MIKES Publication J1/2006, Mittatekniikan keskus, Espoo 2006, ISBN 952-5610-11-X, ISSN 1235–2704

[2] S. Zuñiga-Gonzalez, P. Olvera-Arana, J.C. Torres-Guzman, F.J. Flores-Martinez, Pneumatic gauge pressure proficiency test in the range from –70 kPa to 0 kPa for Mexican accredited laboratories, in: Abstracts of IMEKO TC3 & TC16 & TC22 International Conference, Merida, Mexico 2007, 154–155

[3] R.S. Dadson, S.L. Lewis, G.N. Peggs, The pressure balance – theory and practice, Her Majesty's Stationery Office, London 1982

[4] M.H. Orhan, Y. Calkin, J. Tesar, Z., Krajicek, Pneumatic gauge pressure comparison measurements between the UME (Turkey) and the CMI (Czech Republic) – EUROMET project No. 537, Metrologia 38 (**2001**), 173–179

[5] J. Tesar, J. Jaeger, Z. Krajicek, W. Schultz, Pressure comparison measurement between CMI and PTB in the range 0.07 MPa to 0.4 MPa, Metrologia 36 (**1999**), 647-650

[6] IUPAC – International thermodynamic tables of the fluid state – Vol. 6. – Nitrogen. Pergamon Press, Oxford 1979

[7] Available from World Wide Web: www.bipm.org

[8] C. G. Rendle, A large area piston gauge for differential and gauge pressure from zero to 3,2 kPa, Metrologia 30 (**1994**), 611–614

[9] A. Ooiwa, Novel Nonrotational Piston Gauge with Weight Balance Mechanism for the Measurement of Small Differential Pressures, Metrologia 30 (**1994**), 607–610

[10] J. Tesar, D. Prazak, The limitations for using the vacuum standards based on piston-cylinder technique, Vacuum 67 (**2002**), 311–316

[11] J. Tesar, P. Repa, D. Prazak, Z. Krajicek, L. Peksa, The new method of traceability of a force balanced piston gauge used as primary vacuum standard, Vacuum 76 (**2004**), 491–499

[12] J. Tesař, D. Pražák, F. Staněk, P. Řepa, L. Peksa, Ensuring primary realization of pressure unit in the vacuum range without typically utilized static expansion system, Vacuum 81 (**2007**), 785–787

[13] J. Tesař, D. Pražák, The methods of CMI traceability for the standards of the differential pressure at high line pressures. in: Middle East measurement and instrumentation, Bahrain, 2004, 313–328

UDK 552.54:54:55
Original scientific article/Izvirni znanstveni članek

ISSN 1580-2949
MTAEC9, 43(3)157(2009)

THE GEOLOGICAL RECORD AS AN INDICATOR OF THE MUDSTONES THERMAL CHARACTERISTICS IN THE TEMPERATURE RANGE OF DECARBONATISATION

GEOLOŠKI ZAPIS KOT POKAZATELJ TERMIČNIH LASTNOSTI LAPOROVCEV V TEMPERATURNEM OBMOČJU DEKARBONATIZACIJE

Željko Pogačnik[1], Jernej Pavšič[2], Anton Meden[3]

[1]Salonit Anhovo, Building Materials, Joint-Stock Co., Vojkova 1, 5210 Deskle, Slovenia
[2]Chair of paleontology and strathigraphy, University of Ljubljana, Privoz 11, 1000 Ljubljana, Slovenia
[3]Faculty of Chemistry and Chemical Technology, University of Ljubljana, Aškerčeva cesta 5, 1000 Ljubljana, Slovenia
zeljko.pogacnik@salonit.si

Prejem rokopisa – received: 2008-10-03; sprejem za objavo – accepted for publication: 2008-12-06

The aim of this work is to find a connection between the marlstones geological record, i.e., its origin, and the thermal properties in the range of the decarbonatisation processes. As the geological record we took the recognized alteration or modification of the chemical and mineralogical difference, the amount of heavy metals and the fossilized nanoplankton material. For this research we collected and analyzed mudstones from four different lithological horizons of the subaquatic gravitational avalanche – turbidite, Paleocene flyschoidic rocks from the Anhovo area.

The remains of the nanoplankton fossilized skeletons are the main bearer of the amount of $CaCO_3$ in this kind of sedimentary rock, besides a small quantity of carbonate fragments, mostly from older sedimentary rocks. We used optical microscopy, XRF, XRD and TGA-DTA analytical methods and granulometric analysis. The clay mineralogy was obtained from the acid residual XRD and DTG-DTA (temperature range to 1000 °C) analyses.

The research results demonstrated that we can expose four different groups of mudstones with similar thermal characteristics in the temperature range of the decarbonatisation. The chemical alternation degrees – the *CIA* of the rocks showed a connection between the clay mineralogy and the temperature course of the thermal decomposition of the mudstone carbonate. The quantity of nanoplankton skeletons followed a similar trend. The fundamental digressions in the heavy metals were not recognized, but the Ba quantity showed a good correlation with the samples that had a larger number of skeletons. We related this behavioural particularity with the biological activity of the environment. Both the *CIA* factor and the correlation of the skeleton number with the Ba content demonstrated different sedimentary environments and subsequently the influence of the geological record on the thermal decomposition nature of the rock in the range of decarbonatisation.

Key words: chemistry and mineralogy, cocolithophycae, mudstone thermal properties

V prispevku želimo poudariti povezavo med zgodovino (geološkega zapisa) nastanka laporovca litotipa mudstone in njegovimi termičnimi lastnostmi pri procesu dekarbonatizacije. Kot geološki zapis pojmujemo prepoznavno spremembo v kamnini, ki se kaže v njeni kemijski in mineraloški sestavi, vsebnosti težkih kovin in številu fosilnih skeletov kalcitnega nanoplanktona. V ta namen so bili analizirani vzorci laporovcev iz štirih litostratigrafskih členov treh ciklotem (zaporedje kamnin, ki so nastale kot posledica delovanja podvodnih gravitacijskih plazov) paleocenske starosti na območju Anhovega.

Delež $CaCO_3$ v laporovcih so večinoma skeleti mikrofosilov–kokolitoficej in karbonatni drobir. Vzorci so bili analizirani z optično mikroskopijo, XRF, XRD, TGA-DTA in granulometrijsko analizo. Za določitev mineralov glin so bili vzorci izpostavljeni kislinskemu razklopu s klorovodikovo kislino. Netopni ostanek je bil ponovno analiziran z XRD- in DTG-DTA-metodo v temperaturnem območju do 1000 °C.

Na osnovi rezultatov lahko med analiziranimi vzorci poudarimo štiri skupine, ki imajo podobne termične lastnosti v območju dekarbonatizacije. Stopnja kemijsko spremenjene kamnine-*CIA* kaže, da so količina mineralov glin in njihove spremembe povezane s temperaturnim potekom termičnega razpada laporovca tipa mudstone. Podobno usmeritev je opaziti tudi pri številu ohranjenih skeletov kokolitoficej. Bistvenih odmikov med vzorci glede vsebnosti težkih kovin ni opaziti, razlikujejo pa se v vsebnosti Ba, ki posredno z ohranjenimi skeleti kokolitoficej kaže na biološko aktivnost sedimentacijskega okolja. Tako faktor *CIA* kot število kokolitoficej kažeta različno sedimentacijsko okolje kamnine litotipa mudstone oz. da ima geološki zapis vpliv na lastnosti kamnine v temperaturnem območju dekarbonatizacije.

Ključne besede: kemizem in mineralogija, kokolitoficeje, termične lastnosti laporovcev

1 INTRODUCTION

The mineral raw material used to produce portland cement clinker (OPC) in the Anhovo area is bound to subaquatic gravitational avalanches [1], which set off at unstable shores in the late Paleocen. The raw material consists of marly breccias, marly limestone and limestones, coarse-grained, medium-grained and fine-grained lime sandstones, marlaceous limestones and marls, and a combination of shales, carbonate and silicyclastic siltstones and slatestones. The mudstones are carbonate sedimentary rocks with a silty base and a weight proportion of grains (either of organic or inorganic origin) not exceeding 10 %. The grains are 30 μm to 2 mm in diameter. They are typical of a calm and deep-water environment. In the pelagic environment the producers of carbonate material are mainly plankton organisms.

When a marly grain is thermally decomposed, a sharp edge is produced between a new CaO and a yet unreacted carbon core, showing that the grain decarbonatisation process is created first on the inside and then it spreads outside. The marls carry SiO_2. Due to the genetic character of the rock, it is mostly equally spread and forms the basis as clay minerals in between carbonated particles. All the clay minerals lose bound water between the layers in the temperature range between 100 °C and 200 °C. First off, the minerals of the kaolonite groups fall apart between 450 °C (or 500 °C for the illite group) and 600 °C; they lose chemically bound OH in the process of complete decomposition. In the temperature range between 600 °C and 700 °C, the minerals of the montmorilite group lose the OH group and this corresponds to the process area of decarbonatisation.

This article aims to emphasize the influence of the geological record of mudstone creation on its thermal characteristics in the process area of decarbonatisation, which is in the temperature interval between 650 °C and 950 °C. This adheres to the recognized rock change in the geological record, reflecting a direct or indirect sedimentary environment in which the rock has been created. The changes occur in the mineralogy and the preserved number of fossil remnants, indirectly indicating the biological and physico-chemical activities of the sedimentary environment.

2 MATERIAL SELECTION AND ANALYTICAL METHODS

The sampled minerals belong to the group of marly olistolithes of basal breccias (cyclothems Rodež and Perunk) and the marl of the upper cyclothem part Podbrdo. Due to the specific genesis[3] and rock position[4] that involve the sites of mineral raw materials, significant differences between the individual eroded and pre-sedimented marls in flyschoidic cyclothems need to be determined (**Figure 1**).

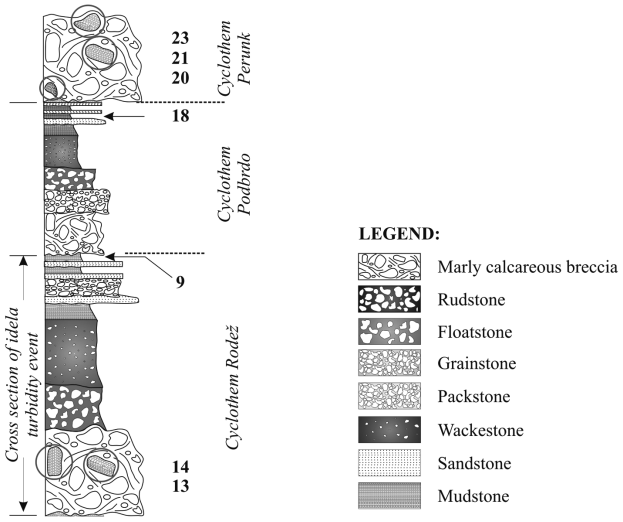

Figure 1: The classification of the analyzed samples in mega cyclothems
Slika 1: Razporeditev analiziranih vzorcev v megaciklotemah

The following samples have been analyzed: Sample 13 and Sample 14 (eroded marlstones from marly calcareous breccia of cyclothem Rodež), marlstone Sample 9 (from the upper part of cyclothem Rodež), Sample 18 (marlstone of Podbrdo cyclothem), Sample 20, Sample 21 and Sample 23 (eroded marlstones from marly calcareous breccia of cyclothem Perunk). To determine the significant differences between the marlstones, the XRF and XRD analyses were carried out, along with the thermal methods (TG-DTG-DTA), the analysis of strong acid digestion, granulometric analysis of the insoluble residue and the petrographic microscopic analyses.

Part of the samples was crushed in a laboratory mill, and the rest was used to carry out the micropaleonthological analysis. We used a scraping tool to obtain some pulverized parts from the undamaged sample of the rock. Those parts were dissipated in the water, dried up and covered in Canadian balm. That preparation was then evenly distributed on the microscopic glass and covered with a square coverslip, the a side of 22 mm. We used transmitted light by applying cross nicols and regularly transmitted light magnified 1000 times; with a microscopic analysis we evaluated (per unit of surface area) the quantity of nanoplankton skeletons.

To determine the main oxides (SiO_2, Al_2O_3, Fe_2O_3, CaO, MgO, K_2O, Na_2O, SO_3 and calculated $CaCO_3$, assuming that the whole CaO is bound to carbonates) and certain metals (V, Ba, Ni, Cr, Ti in Mn), we used XRF analyses. The voltage and current of the x-ray tube of the ARL 8480 instrument were 30 kV and 80 mA, whereas the recording time was set to 40 s. The samples were examined by applying XRD analyses and the TG-DTG-TGA methods (defining $CaCO_3$ from the emitted CO_2).

The samples for the XRD analysis were recorded on a PANalytical X'Pert PRO MPD diffractometer by applying the reflection technique and the $CuK_{\alpha 1}$ radiation in the 2θ range from 3° to 70° in steps of 0.034° 2θ, an integration time of 400 s, a 20-mm mask and a divergent and an antiscatter slit, set to 20 mm of the sample irradiation. Soller slits of 0.02 radians were used on both sides and the whole detector range was applied. The sample was rotated around the vertical axis. The Rietveld analysis of the diffraction pattern was performed with the TOPAS 3.0 programme and with the use of models containing 9 to 12 of the crystalline phases. In all cases a very good final match of the calculated and measured pattern with R_{wp} at around 6 % was obtained.

While analysing the samples with thermal methods, well-homogenized measured parts were heated in cylindrical pots (1 mm to 3 mm in height and 4 mm in diameter) made of inert materials (platinous and Al_2O_3

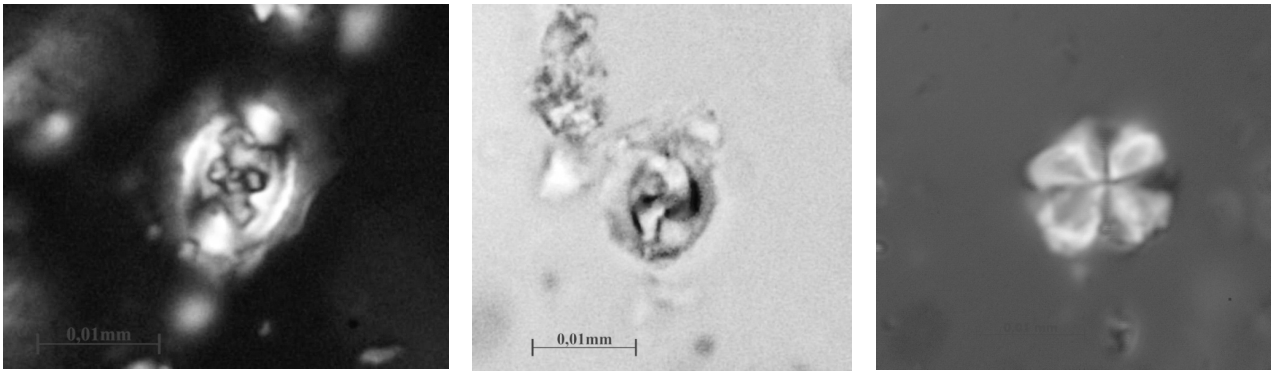

Figure 2: Calcite nanoplankton from the Sample 23: a) *Chiasmolithus bidens,* b) *Ellipsolithus macellus* in c) *Fasciculithus tympaniformis.* Pictures a) and c) are recorded under crossed nicols, b) is recorded by applying regular light.

Slika 2: Kalcitni nanoplankton iz vzorca 23: a) *Chiasmolithus bidens,* b) *Ellipsolithus macellus* in c) *Fasciculithus tympaniformis.* Sliki a) in c) sta posneti pod navzkrižnimi nikoli, b) pa pri navadni svetlobi.

pots) by applying a temperature scan of 10 °C/min at room temperature and up to 1400 °C. We used the STD 2960 *Simultaneus* DTA-TGA analyser to carry out this procedure. When the signal analysis was made, we elaborated on the temperature parameters, which are presented in **Table 1**, see below. The software tool *Universal Analysis for Windows 95/98/NT,* edition *2.5H*, was used to define the parameters.

Table 1: Temperature parameters[5,6,7]
Tabela 1: Temperaturni parametri [5,6,7]

Parameter	Explanation
T_2	The temperature at which the reaction ends, corresponds to T_{offset} (identified with 1. derivative of the TG-curve)
T_{onset}	The temperature which triggers the decomposition reaction – crystallization – is the lowest temperature which triggers the process ≠ T_1
T_{max}	The temperature at which the process triggered reached its peak

To divide the clay component basis in marlstones, we carried out an acid decomposition of the samples. In a container with 450 mL of distilled water there was a 100-gram sample, to which we gradually added diluted hydrochloric acid (37 % concentrated HCl acid, mixed with distilled water in a 1:1 ratio) with a total capacity of 200 mL. The insoluble residue was decanted with destilled water to reach pH ≈ 4. Then the material was dried in a drier at 37 °C for 18 h. The samples obtained were passed through a sieve of 45 μm and the residue was analysed by applying the XRD-method and thermal analyses. On the basis of the results obtained, we evaluated the mineralogy of the insoluble residue.

3 RESULTS OF THE ANALYSIS

The microscopic analysis showed that Sample 23 (followed by Sample 21 and Sample 14 – **Table 2**) contains the largest number of fossil skeletons of the nanoplankton organisms.

Table 2: The number of fossil units (the number on the diameter area of 22 mm^2) in the individual sample
Tabela 2: Število fosilnih enot (št. na površini premera 22 mm^2) v posameznem vzorcu

SAMPLE	Number of units
Sample 9	162
Sample 13	142
Sample 14	370
Sample 18	120
Sample 20	165
Sample 21	468
Sample 23	880

In Sample 23, besides many other types of calcite nanoplankton, we also detected the following types (**Figure 2**): *Chiasmolithus bidens* (Bramlette et Sullivan), *Ellipsolithus macellus* (Bramlette et Sullivan) ter *Fasciculithus tympaniformis* (Hay et Mohler).

According to the proportion of the calcium carbonate, determined on the basis of the emitted CO_2 at the decarbonatisation process (**Table 3**), we concluded that

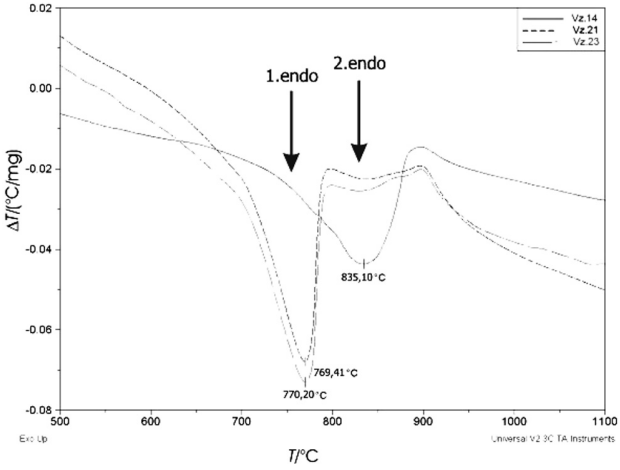

Figure 3: DTA curves of the Samples 21, Sample 23 and Sample 14
Slika 3: DTA krivulja vzorcev Vz. 21, Vz. 23 in Vz. 14

Table 3: The results of the XRF- and TG-DTG-DTA analyses of the primary sample
Tabela 3: Rezultati XRF- in TG-DTG-DTA analize osnovnega vzorca

SAMPLE	proportion CO_2	$CaCO_3^{TG}$	Ti	SiO_2	Al_2O_3	Fe_2O_3	CaO	MgO	K_2O	Na_2O	$CaCO_3$	V	Ba	Ni	Cr	Mn
	TG-DTG-DTA		XRF													
	(mass proportion, *w*/%)											*w*/(μg/g)				
Smp. 9	23.65	53.75	0.15	19.60	5.16	2.40	37.65	1.37	1.11	0.22	67.21	56	550	53	54	568
Smp. 13	25.29	57.48	0.14	18.96	4.73	2.28	38.18	1.49	1.02	0.21	68.16	49	454	52	53	499
Smp. 14	26.73	60.75	0.16	21.80	5.52	2.80	35.33	1.67	1.25	0.25	63.07	61	457	60	57	533
Smp. 18	25.75	58.52	0.15	20.74	4.83	2.25	37.48	1.40	1.00	0.26	66.90	54	324	50	57	381
Smp. 20	23.70	53.86	0.15	21.05	4.85	2.28	37.34	1.38	1.00	0.26	66.65	52	377	51	58	382
Smp. 21	19.14	43.50	0.20	26.14	6.71	3.09	32.39	1.42	1.32	0.18	57.81	66	199	65	66	463

Table 4: TG-DTG-DTA analysis of the original sample and the insoluble residue (the residue on a sieve of 45 μm) in the the temperature interval of decarbonatisation
Tabela 4: TG-DTG-DTA-analiza originalnega vzorca in netopnega ostanka (ostanek na situ 45 μm) v temperaturnem intervalu dekarbonatizacije

SAMPLE	Analysis of the original sample					
	T_{onset}	T_{max}	T_{max} -T_{onset}	T_2	CO_2	$CaCO_3$
	°C				*w*/%	
Smp. 9	717.13	778.62	61.49	812.60	23.65	53.75
Smp.13	715.62	779.58	63.96	812.70	25.29	57.48
Smp.14	757.94	835.10	77.16	911.00	26.73	60.75
Smp.18	716.18	786.78	70.60	825.30	25.75	58.52
Smp. 20	713.88	777.31	63.43	809.50	23.70	53.86
Smp. 21	709.51	769.41	59.90	798.40	19.14	43.50
Smp. 23	706.43	770.20	63.77	801.60	18.68	42.45
Analysis of the insoluble sample residue on the sieve of 45 μm						
Smp. 9	-	-		-	-	-
Smp.13	682.91	767.27	84.36	798.90	23.13	52.57
Smp.14	728.26	795.22	66.96	824.90	10.61	24.11
Smp.18	695.72	777.98	82.26	809.76	27.47	65.18
Smp. 20	682.91	767.27	84.36	798.90	23.13	62.43
Smp. 21	-	-		-	-	-
Smp. 23	636.58	751.11	114.53	837.60	10.52	23.91

Sample 14 contains the largest amount of carbonate, whereas Sample 21 and Sample 23 contain the smallest amount.

Figure 3 shows concave curves of the DTA samples 23, 21 and 14. The number of DTA signals shows at least two endothermic reactions in the range of the thermal decomposition of carbonate, whereas the curve of Sample 14 has an extremely low amplitude and a shifted T_{max}.

The TG-DTG-DTA analysis of the insoluble residue in the decarbonatisation range shows strong endotermic peaks; they show characteristic temperatures at the beginning of the reaction and maximum temperatures at the very end of the reaction of the thermal carbonate decomposition (see **Table 4**).

The results of the XRD analysis (**Table 5**) show the presence of carbonate in the insoluble residue.

In all the primary samples the calcite is dominant, and flexures of different clay minerals at low angles can be clearly seen. Besides calcite, the following were also defined in the primary sample: quartz (SiO_2), muscovite ($KAl_2(AlSi_3O_{10})(OH)_2$, vermiculite ($Mg_4(AlSi_3O_{10})(OH)_2(H_2O)_4$, kaolinite ($Al_2(Si_2O_5)(OH)_4$, kronstedtite ($Fe_3(FeSi)O_5(OH)_4$, cristobalite ($SiO_2$), iIlite ($K(Al_4Si_2O_9(OH)_3)$), dolomite ($CaMg(CO_3)_2$, ankerite ($CaFe(CO_3)_2$, aragonite $CaCO_3$ and protoenstatite ($MgSiO_3$). In the insoluble residue the calcite was not identified in samples 9 and 21. The proportion of false analysis is 3 % absolute with calcite, 1 % with muscovite, kaolinite and illite and 0.5 % with other components. Total proportion of the unidentified crystalline

Table 5: XRD and TG-DTG-DTA determination of certain mass proportions of minerals (%) in the primary sample (BULK) and its insoluble residue (<45 μm)
Tabela 5: XRD-in TG-DTG-DTA-določitev nekaterih masnih deležev mineralov (%) v osnovnem vzorcu (BULK) in njegovem netopnem ostanku (<45 μm)

SAMPLE	Kaolinite $Al_2(Si_2O_5)(OH)_4$		Illite $K(Al_4Si_2O_9)(OH)_3$	Muscovite $KAl_2(AlSi_3O_{10})(OH)_2$	**Illite/ muscovite**	Albite $NaAlSi_3O_8$	**Calcite** $CaCO_3$	**Calcite** $CaCO_3$
	BULK	45 μm<	BULK	BULK	<45 μm	<45 μm	BULK	<45 μm
Smp. 9	3.30	9.32	3.81	9.26	35.38	8.84	75.53	-
Smp.13	2.97	2.87	3.94	9.04	13.63	7.25	73.13	57.84
Smp.14	3.04	5.72	4.91	9.46	36.31	7.96	72.73	14.46
Smp.18	2.52	1.03	3.58	9.06	8.78	4.49	74.60	74.75
Smp. 20	2.69	2.04	3.70	9.05	10.19	4.38	74.07	71.22
Smp. 21	2.81	7.13	5.47	11.23	45.67	8.02	69.71	-
Smp. 23	2.81	5.52	6.20	8.84	35.97	5.72	71.06	23.84

phases is evaluated to less than 5 %; the amorphous phase is probably less than 10 %.

4 DISCUSSION

The number of determined nanoplankton skeletons (**Table 1**) can be compared to the determined carbonate proportion in the individual sample (**Tables 2 and 3**). The difference can occur because of the group of carbonate minerals, parts of them, not bound to the then existing living environment of the nanoplankton organisms.

This is confirmed by the results of the diffraction and thermal analyses. The data show that the samples differentiate by the process type of decarbonatisation (double endothermic peaks; **Figure 3**), in the T_{onset} temperature and in the time to reach the maximum temperature of the carbonate decomposition (T_{max}, **Table 4**). In the sifted residue of the acid-treated sample (the size of grains below 45 μm) there is an unreacted carbonate (TG-DTG and XRD analyses), showing the presence of relatively older carbonate rocks that were eroded off from the older beds in the sedimentation process (of subaquatic avalanche) or brought in from the different sedimentary environment (most likely diagenetically already altered – alumosilicate cement).

The interdependence of the mudstone rock samples from the Paleocenic flyschoidic beds on the level of the temperature parameters (T_{onset}, T_{max} in T_{max}–T_{onset}), the geological record indicating when the marlstones were created (*CIA*[*,8], K_2O/Al_2O_3, K_2O+Na_2O, K_2O, $CaCO_3$, Cr/Ni, Cr/V, Mn, Ti/Al, K/(Fe+Mg), Ba and the number of skeletons) and the ratio *F*[**] are summarized in the **Table 6**.

Through a statistical overview of the results it can be concluded that the *CIA* factor and the number of preserved cocolithophycae skeletons have a great influence on the start-up reaction temperature T_{onset} and the maximum temperature of the reaction process T_{max}. From the geological record it can also be concluded that K-alumosilicates and clay minerals are prevalent in the samples (as shown by the results of the diffraction analysis – **Table 5**). The influence is shown in the T_{max}–T_{onset} temperature interval. Diagenesis runs were made to disintegrate the acid feldspars (orthoclase) into K-feldspars and further into clay minerals. In our case, the diffraction analysis did not identify the orthoclase; the albite, however, was identified. It appears together like the mineral joint with orthoclase in medium and acid magmatic rocks.

Table 6: Correlation table of the temperature parameters, the geological record of the marlstones and the F ratio
Tabela 6: Korelacijska tabela temperaturnih parametrov, geološkega zapisa laporovcev in razmerja F

	F	T_{onset}	T_{max}	T_{max}–T_{onset}	*CIA*	$w(K_2O)/w(Al_2O_3)$	$w(K_2O + Na_2O)$	$w(CaCO_3)$	št. skeletov	*w*(Ba)	$w(K_2O)$	*w*(Cr)/*w*(V)	*w*(Cr)/*w*(Ni)	*w*(K)/*w*(Fe + Mg)	*w*(Ti)/*w*(Al)	$w(SiO_2)/w(Al_2O_3)$
F	1															
T_{onset}	0.892	1														
T_{max}	0.932	0.990	1													
T_{max}–T_{onset}	0.946	0.853	0.917	1												
CIA	0.770	0.871	0.898	0.876	1											
$w(K_2O)/w(Al_2O_3)$	0.836	0.828	0.803	0.644	0.507	1										
$w(K_2O + Na_2O)$	0.617	0.433	0.509	0.669	0.336	0.317	1									
$w(CaCO_3)$	0.859	0.648	0.676	0.682	0.341	0.867	0.616	1								
The No.of skeletons	0.765	0.919	0.879	0.665	0.731	0.895	0.149	0.592	1							
w(Ba)	0.479	0.461	0.416	0.238	0.054	0.846	0.131	0.710	0.675	1						
$w(K_2O)$	-0.289	0.009	-0.011	-0.066	0.377	-0.402	-0.469	-0.719	0.042	-0.518	1					
w(Cr)/*w*(V)	-0.385	-0.653	-0.596	-0.367	-0.570	-0.505	-0.029	-0.178	-0.718	-0.331	-0.315	1				
w(Cr)/*w*(Ni)	-0.075	-0.366	-0.312	-0.122	-0.524	-0.188	0.584	0.271	-0.553	-0.060	-0.763	0.558	1			
w(K)/*w*(Fe + Mg)	-0.582	-0.266	-0.317	-0.429	-0.056	-0.471	-0.514	-0.780	-0.117	-0.310	0.795	-0.400	-0.546	1		
w(Ti)/*w*(Al)	0.073	-0.192	-0.143	0.014	-0.349	-0.095	0.623	0.352	-0.444	-0.123	-0.748	0.449	0.948	-0.646	1	
$w(SiO_2)/w(Al_2O_3)$	0.269	-0.029	0.041	0.238	-0.157	0.029	0.735	0.474	-0.303	-0.054	-0.729	0.550	0.885	-0.791	0.925	1

[*] $CIA = \frac{w(Al_2O_3)}{w(Al_2O_3) + w(CaO) + w(Na_2O) + w(K_2O)} \cdot 100$; proportion of CaO^* is a calculated proportion of CaO on the basis of the CaO difference, set by XRF-analysis and CaO, defined with the decarbonatisation process applying DTG-DTA-analysis.

[**] $F = \frac{w(CaO_t)}{w(CaO_f)}$, CaO_f is a calcium oxide, which is created through decarbonatisation process and the proportion of CaO_t is bound to an absolute quantity of Ca-oxide, defined in the sample on the basis of XRF-analysis.

The proportion of heavy metals in the samples (**Table 3**) is shown by the influence of the disintegrated ultramaphic complex [9] (correlation between Cr/Ni and Cr/V with SiO_2/Al_2O_3 proportion, **Table 6**) and the terigen insertion of individual minerals in the source of the clay component in the marlstones. Titanium is an extremely conservative trace element [10] and as such it is resistent to diagenetic factors, while the Al proportion has a dominant role in indicating the clay minerals. The correlation between Ti/Al and SiO_2/Al_2O_3 (**Table 6**) shows that Ti entered the sedimentary environment through the river input or through earlier, eroded sedimentary rocks.

The hypothesis about the vulcanoclastic source of sediments is not acceptable, as this theory is disproved by a negative correlation [10] between the Ti/Al and the K/(Fe+Mg). The proportion of Mn[11] in the samples also shows the terigen import of the sediment or presedimentation. The negative correlation between the Ba and K_2O shows that Ba is not bound to the clay component [12], although Ba^{2+} and K^{2+} can interchange in the crystal structure. So the source of Ba is to be ascribed to a general carbonate cycle, which corresponds to the ratio of $CaCO_3$ proportion and the number of nanoplankton skeletons in individual samples (**Table 2**).

5 CONCLUSION

The thermal analysis results show that marlstones of the mudstone lythotype react differently during the decarbonatization process (**Figure 4**) in the temperature range between 650 °C and 950 °C. Four groups can be distinguished among the curves. The two pairs of curves of the Sample 23 and Sample 21 are prominent among them, having two endothermic peaks. Sample 18 and Sample 13 are also worth mentioning, with the second endothermic peak being less emphasized.

The oldest marlstones – olistholites (Sample 13 and Sample 14) – taken from a marly calcareous breccia comper with Sample 9, from the upper part of the Rodež cyclothem, have the highest *F* ratio among all the samples, considering their litostratigraphic sequence. They differ from one another in the number of nanoplankton skeletons and in the proportion of chemical change *CIA* factor. We can therefore conclude that the rocks were formed in two different sedimentary environments.

The marlstones of the Podbrdo cyclothem (Sample 18) differ from the previously mentioned samples in the quantity of the biogenic carbonate (number of skeletons) and Ba proportion, therefore confirming the biological activity of the environment. They also differ in the *CIA* factor, which is lower in the sample richer in fossils. In Sample 18 carbonate was identified in the insoluble residue; we therefore assume that in the sedimentation period different sources of carbonate material were present.

The marlstone samples (Sample 21, Sample 23 and Sample 20), taken in the youngest horizon of the marly calcareous breccia of Perunk cyclothem, differ from one another by the *F* ratio. Among the marlstones of this lythological horizon the F value is larger in the samples which hold a higher proportion of Ba. The number of skeletons and the content of Ba show that there are at least two different sedimentary environments to be distinguished in this marlstone group.

The *CIA* proportion (**Figure 5**) confirms that the number of feldspars and clay minerals, and the accordingly bound diagenetic changes, are related to the temperature process of the thermal decomposition of the carbonate rock. This is also evident from the correlation factor between the *CIA* and the start-up reaction temperature T_{onset}, as well as the maximum decarbonatization temperature T_{max}. A similar trend can be seen in the number of preserved cocolithophycae skeletons. Despite

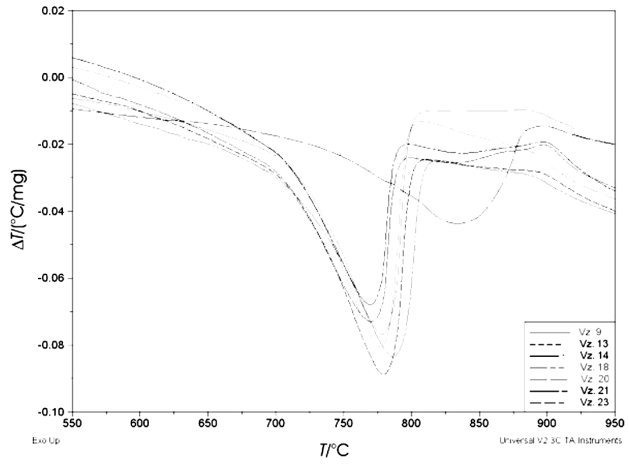

Figure 4: Comparison of marlstone DTA curves of mudstone type
Slika 4: Primerjava DTA-krivulj laporovcev tipa mudstone

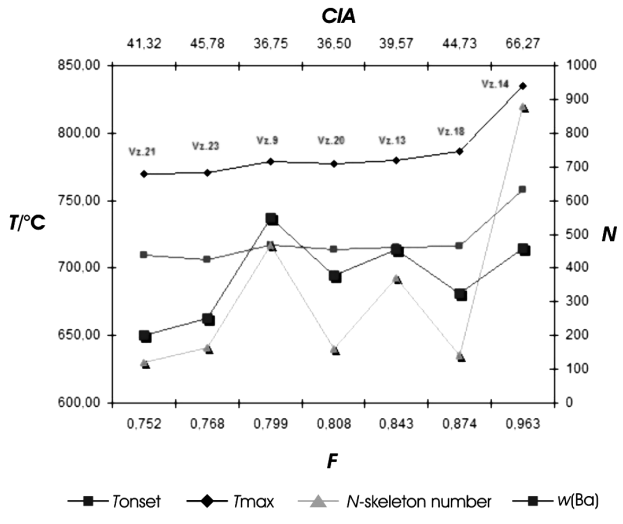

Figure 5: The ratio between the number of skeletons, Ba proportion (μg/g), start-up reaction temperature T_{onset} (°C) and the *F* factor
Slika 5: Razmerje med številom skeletov, deležem Ba (μg/g), temperaturo začetka reakcije T_{onset} (°C) in faktorjem *F*

the approximately even number of skeletons the curves of Sample 23 and Sample 13 are shaped differently. The difference can be seen in the *CIA* ratio, as the latter is 13 % higher in Sample 23 than in Sample 13.

The proportion of heavy metals indicates the source of fine-grained material[13] (most likely the area of today's Carnic Alps), whereas the number of preserved skeletons and the Ba content indicate the change of the sedimentary environment in which the rock was created. The proportion of carbonate in the insoluble residue still remains unknown at this stage, although it does allow for the hypothesis of the material in the sample being of secondary origin (either presedimented or eroded from older cyclothems).

The highest CaO proportion, bound in carbonate, and the largest amount of cocolithophycae can be found in Sample 14. This is followed by Sample 18, having the largest carbonate proportion in the insoluble residue; here the ratio between Ba and the number of skeletons allows for the hypothesis of the larger carbonate proportion being bound to fossil pelagic organisms, i.e. it is of biogenic origin.

The marlstone reflects the chemical and mineralogic features influencing the temperature reaction process in the carbonate decomposition range. The results of the analysis show that a sole definition of the rock lythotype does not clearly establish the temperature characteristic of the sedimentary rock [2] in the decarbonatisation area. Consequently, the geological record has an important influence on the temperature range of the decarbonatisation of the mudstone rock in the Paleocenic sedimentary environment in the close-by area of Anhovo.

6 REFERENCES

[1] Skaberne, D. Sedimentological investigation of flysch from the Anhovo area. Diploma degree (in Slovene), Katedra za geologijo in paleontologijo, NTF, Ljubljana, 1973, 285

[2] Dunham, R. J. Classifications of carbonate rocks according to depositional texture. V: Clasification of Carbonate Rocks, a Simposium. Edited by Ham, E.W. Tulsa, (**1962**), 108–122

[3] Skaberne, D. Observation Point N° II/9, The Paleocene megaturbidites – Anhovo. V Evolution of the karstic carbonate platform – Excursions Guidebook, 5. June – 6. June. Trieste : Universitá degli studi di Trieste, Instituto di geologia e paleontologia, 1987, 37–45

[4] Pogačnik, Ž., Car, M. Prostorska umestitev fliša v okolici Rodeža-integrirani raziskovalni pristop. In: Horvat, Aleksander (ur.). 18. posvetovanje slovenskih geologov, (Geološki zbornik, 19). Ljubljana: Univerza v Ljubljani, Naravoslovnotehniška fakulteta, Oddelek za geologijo, 2007, 92–96

[5] Mackenzie, R. C. The differential thermal investigation of clays. London: Mineralogical society (clay minerals group), 1957, 456 str.

[6] Ramachandran, V. S., Phil, D. Applications of differential thermal analysis in cement chemistry. Chemical pulishing company, 1969, 308

[7] Yen, F. S., Lo, H. S., Wen, H. L., Yang, R. J. θ – to α – phase transformation subsystem induced by α – Al_2O_3 – seeding in boehmite – derived nano – sized alumina powders. Journal of Crystal Growth, (**2003**), 249, 283–293

[8] Nesbitt, H. W., Young, G. M. Early Proterozoic climates and plate motions inferred from major element chemistry of lutites. Nature, (**1982**) 299, 715–717

[9] Barbara B., Mclennan, S. M., Hanson, G. N. Geochemistry and provenance of the Middle Ordovician Austin Glen Member (Normanskill Formation) and the Taconian Orogeny in New England. Sedimentology 45 (**1998**), 635–655

[10] Meyers, S. R., Sageman, B. B., Hinnov, L. A. Integrated quantitative stratigraphy of the Cenomanian–Tturonian Bridge Creek limestone member using evolutive harmonic analysis and stratigraphic modeling. Journal of Sedimentary Research, 71 (**2001**), 4, 628–644

[11] Veizer, J., Demovič, R. Environmental and climatic controlled fractionation of elements in the mesozoic carbonate sequences of the western Carpathians. 1. Journal of Sedimentary Research, 43 (**1973**) 1, 258–271

[12] Dinelli, E, Lucchini, F., Mordenti, A., Paganelli, L. Geochemistry of Oligocene-Miocene sandstones of the northen Apennines (Italy) and evolution of chemical features in relations to provenance changes. Sedimentary Geology, 127 (**1999**), 193–207

[13] Venturini, S., Tunis, G. La composizione dei conglomerati cenozoici del Friuli: dati prliminari. In: Studi Geologici Camereti, Studi preliminari all' acqusizione dati del profilo CROP 1-1A La Spezia-Alpi orientali, 1992, 285–295

UDK 54:666
Strokovni članek/Professional article

ISSN 1580-2949
MTAEC9, 43(4)165(2009)

KERAMIČNI KOMPOZITI NA OSNOVI SILICIJEVEGA NITRIDA

CERAMIC COMPOSITES BASED ON SILICON NITRIDE

Aljoša Maglica, Kristoffer Krnel, Milan Ambrožič

Odsek za inženirsko keramiko, Institut "Jožef Stefan", Jamova 39, Ljubljana
aljosa.maglica@ijs.si

Prejem rokopisa – received: 2008-10-07; sprejem za objavo – accepted for publication: 2009-04-08

Keramika na osnovi silicijevega nitrida (Si_3N_4) ima odlične mehanske lastnosti in korozijsko obstojnost, zato se uporablja za različne namene, tudi pri visokih temperaturah, kjer so drugi materiali manj primerni. V tem prispevku je opisana uporaba nekaterih kompozitov Si_3N_4. Z dvema takšnima kompozitoma (sialoni in silicijev nitrid s prevodno manjšinsko keramično komponento) smo se ukvarjali tudi v naši raziskovalni skupini.

Ključne besede: Si_3N_4, SiAlON, keramični kompoziti

Ceramics based on silicon nitride (Si_3N_4) have excellent mechanical properties and corrosion resistance, thus, they are used for various applications, even at high temperatures where other materials are less appropriate. In this paper the use of some Si_3N_4 composites is presented. Two of such composites (sialons and silicon nitride with conducting minor ceramic component) were studied in our research group.

Key words: Si_3N_4, SiAlON, ceramic composites

1 UVOD

Silicijev nitrid (Si_3N_4) spada med strukturne keramične materiale z najboljšimi mehanskimi lastnostmi, kot čista snov ali kot sestavina kompozitov. V naravni obliki so ga našli le v obliki minerala nierit v meteoritih, sicer pa ga izdelujejo z direktno reakcijo med silicijem in dušikom pri visoki temperaturi.[1] Čisti Si_3N_4 uporabljajo zaradi njegove trdote, obstojnosti pri visokih temperaturah in dobre obrabne obstojnosti za trde prevleke na orodjih, posebno za obdelavo sive litine, medtem ko je za obdelavo jekel primernejši titanov nitrid. Silicijev nitrid v trdih prevlekah orodij, kjer so potrebne velike obdelovalne hitrosti, tekmuje z drugimi keramičnimi materiali: korundom (Al_2O_3), kompozitom Al_2O_3/TiC, polikristalnim diamantom in kubičnim borovim nitridom (c-BN). Keramične trde prevleke se na orodja nanašajo največkrat z naparevanjem, čeprav so pomembni tudi drugi načini, npr. laserski difuzijski postopki. Si_3N_4 je primeren tudi za kroglične ležaje, saj je v primerjavi s kovinami trši in bolj tog. Zato se manj deformira, tako da manjša trenje med ležaji in njihovim nosilcem ter obrabo pri velikih hitrostih. Takšne ležaje najdemo v vozilih, turbinah in celo mlinih na veter. V mikroelektroniki se Si_3N_4 uporablja za električnoizolacijske plasti.[2]

Obstajajo tri kristalografske modifikacije silicijevega nitrida: α, β in γ.[1] Medtem ko sta prvi dve običajni, lahko sintetiziramo γ-strukturo Si_3N_4 le pri visokih temperaturah in tlakih; ta struktura ima zelo visoko trdoto 35 GPa (za primerjavo: značilne trdote aluminijevega oksida Al_2O_3, ki velja za zelo trd material, so okrog 15 GPa). α- in β-Si_3N_4 imata heksagonalno kristalno strukturo, γ-Si_3N_4 pa je kubičen. Kristalna mreža α- in β-Si_3N_4 je iz tetraedrov SiN_4, tako da je Si v težišču vsakega tetraedra, 4 dušikovi atomi pa v ogliščih.[3] V enem oglišču se stikajo trije tetraedri, zato imamo nazadnje pravo razmerje števila silicijevih in dušikovih atomov, 3 : 4 (**slika 1**).

Razlika med strukturama je v simetriji porazdelitve tetraedrov: manj simetrična α-modifikacija ima približno dvakrat večjo osnovno celico (osnovna celica je pravilna 3-strana prizma). Robovi prizme so: $a = b = 0{,}7765$ nm, $c = 0{,}5675$ nm za α-Si_3N_4; $a = b = 0{,}7709$ nm, $c = 0{,}2908$ nm za β-Si_3N_4 (nm = 10^{-9} m). Gostota Si_3N_4 je 3,44 g/cm^3, Youngov modul okrog 300 GPa, upogibna trdnost vsaj 500 MPa, tališče pa 1900 °C. Silicijev nitrid dobimo kot siv prah brez vonja (proizvajalci: UBE Industries Ltd., Japonska; Merck, Nemčija itd.), in sicer v α- in β-modifikaciji (**slika 2**).

Sintranje silicijevega nitrida do visokih gostot je mogoče le ob upoštevanju naslednjih pogojev, kot so: uporaba zunanjega pritiska, povišanje temperature sin-

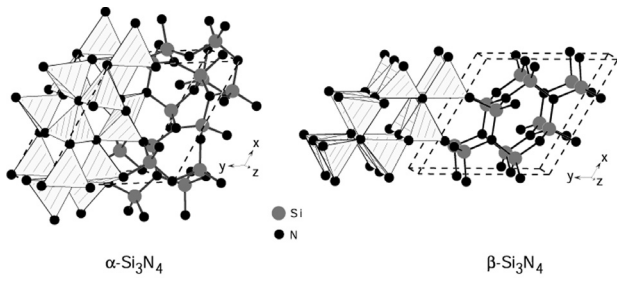

Slika 1: Kristalna struktura α- in β-Si_3N_4[1]
Figure 1: Crystal structure of α- and β-Si_3N_4[1]

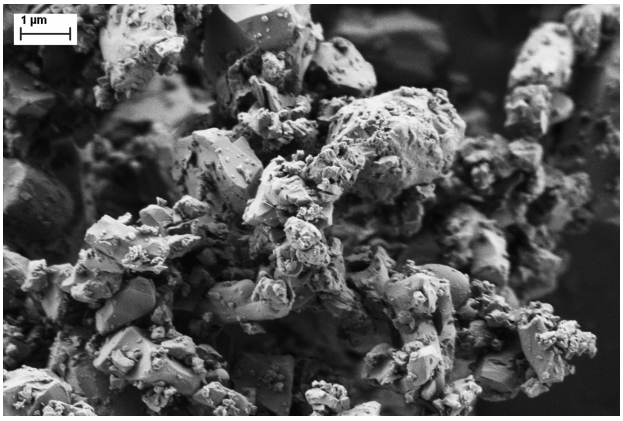

Slika 2: Prah β-Si_3N_4 na grafitnem lepilnem traku; vrstični elektronski mikroskop na poljsko jakost (FEG-SEM), povečava 30 000-kratno, Kemijski inštitut

Figure 2: β-Si_3N_4 powder on graphite sticking tape, field emission scanning electron microscope (FEG-SEM), magnification 30000. National Institute of Chemistry.

tranja in tlaka dušika, uporaba dodatkov za sintranje. Treba je tudi zagotoviti ravnotežne parne tlake vseh komponent z uporabo zasipa iz prahu Si_3N_4. Navadno ob upoštevanju omenjenih pogojev ne dobimo dobrih rezultatov oz. je priprava tovrstne keramike predraga, zato je treba Si_3N_4 dodati ustrezne snovi, ki pri sintranju tvorijo tekočo fazo. Če tekoča faza dobro omaka Si_3N_4 in je ta v njej dobro topen, lahko zgoščevanje opišemo s klasično teorijo sintranja, kot jo je predlagal Kingery: prerazporeditev, raztapljanje-difuzija-precipitacija in koalescenca.

Mehanske in druge lastnosti silicijevega nitrida lahko izboljšamo tudi z drugimi dodatki, npr. z ogljikovimi vlakni, nanodelci SiC (silicijev karbid) itd. Si_3N_4 pa dodajajo tudi kot manjšinsko komponento drugim keramičnim materialom, npr. Al_2O_3 ali ZrO_2, da bi izboljšali njihove lastnosti, kot je obrabna obstojnost. Z dodatki pa lahko spremenimo tudi funkcionalne lastnosti Si_3N_4. **Slika 3** prikazuje kompozite silicijevega nitrida s cirkonijevim nitridom Si_3N_4/ZrN kot enega od različnih prevodnih keramičnih materialov. Prevodno komponento smo za preskus dodajali tudi sialonom. Zgleda za to sta 1) ZrN, ki nastane med reakcijskim sintranjem zaradi dodanega cirkonijevega oksida ZrO_2 v začetno mešanico prahov, in 2) titanov nitrid TiN, ki nastane z reakcijo med silicijevim nitridom in dodanim titanovim oksidom TiO_2.

SEM-posnetka polirane površine sintranih kompozitnih materialov na osnovi Si_3N_4 z dispergiranimi delci ZrN ali TiN sta prikazani na **sliki 4**. S slike je razvidno, da imata oba kompozita homogeno mikrostrukturo z visoko relativno gostoto (> 96 %), ki daje dobre mehanske lastnosti. Mikrostrukturi obeh materialov kažeta podolgovata zrna β-Si_3N_4, med katerimi so razporejena svetla zrna ZrN (**slika 4 a**) ali TiN (**slika 4 b**).

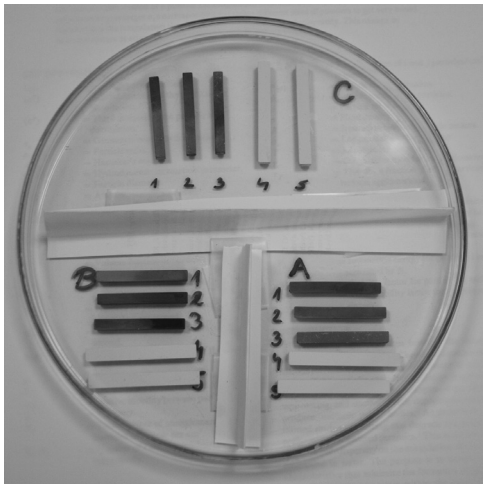

Slika 3: Vzorčne palčke za preskuse trdnosti: svetle palčke so surovci Si_3N_4 z dodanim prahom ZrO_2, temne palčke pa so sintrani vzorci; čisti Si_3N_4 je svetlo siv, ti vzorci pa so temnejši zaradi prisotnosti ZrN, ki je nastal pri kemijski reakciji med sintranjem; izdelano na IJS.

Figure 3: Test bars for measuring flexural strength: bright bars are Si_3N_4 green-bodies with dispersed ZrO_2 powder while the dark ones are sintered samples; pure Si_3N_4 is bright grey, but these samples are darker due to the presence of ZrN which was formed during sintering; fabricated at the JSI.

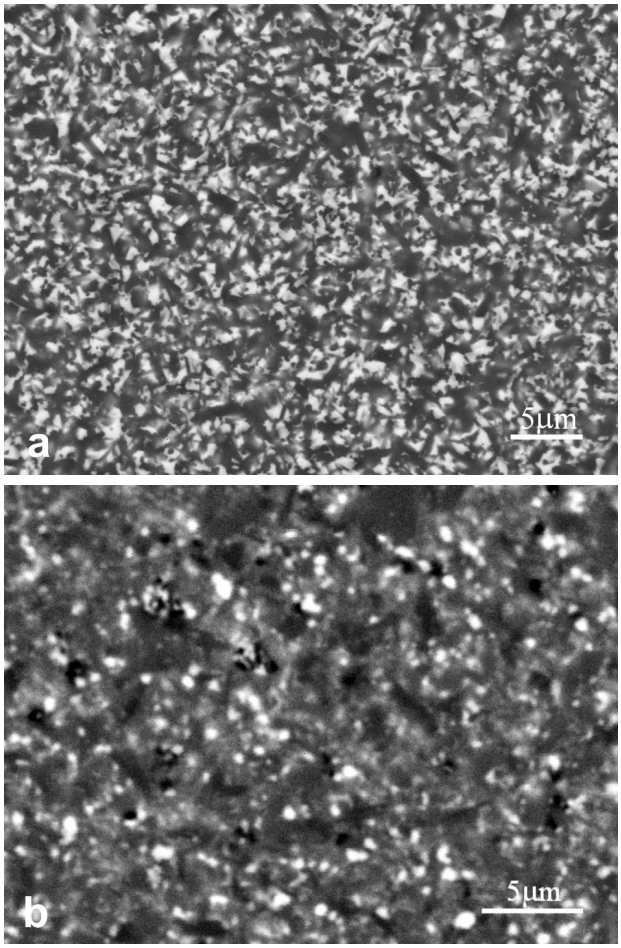

Slika 4: SEM-posnetek polirane površine sintranega kompozita: a) Si_3N_4/ZrN in b) Si_3N_4/TIN, povečava 3000-kratna. IJS

Figure 4: SEM picture of polished surface of sintered composite: a) Si_3N_4/ZrN in b) Si_3N_4/TIN, magnification 3000. IJS

Si_3N_4 je tudi surovina za kompozitno SiAlON (sialonsko) keramiko. Le-ta je trdna raztopina Si_3N_4 in Al_2O_3 z raznimi dodatki za sintranje, kot je itrijev oksid Y_2O_3. Sialoni nastanejo z delno zamenjavo silicija in dušika v kristalni mreži Si_3N_4 z aluminijem in kisikom (odtod njihovo ime: Si = silicij, Al = aluminij, O = kisik, N = dušik).[4] Pomembni modifikaciji sialona sta α in β, osnovani na α- in β-Si_3N_4, zato je morfologija kristalnih zrn sialona α in β podobna morfologiji zrn Si_3N_4. Okvirne vrednosti najpomembnejših lastnosti sialonov so prikazane v **tabeli 1**. α-sialon ima v primerjavi z β-sialonom odlično trdoto, vendar slabšo trdnost, žilavost, toplotno prevodnost in oksidacijsko odpornost, medtem ko ima β-oblika podolgovata zrna z dobro lomno žilavostjo in toplotno prevodnostjo. S primerno kombinacijo obeh faz je možno doseči optimalne mehanske lastnosti.[5]

Tabela 1: Fizikalne lastnosti sialonov[2]
Table 1: Physical properties of sialons[2]

Mehanske lastnosti pri sobni temperaturi	
Upogibna trdnost, MPa	800
Youngov modul, GPa	290
Gostota, g/cm^3	3,3
Trdota, GPa	17
Lomna žilavost, MN m$^{-3/2}$	6,2
Termične in električne lastnosti	
Specifična toplota, J/(kg K)	710
Električna upornost, Ω cm	10^{12}
Koeficient termičnega raztezka, 10^{-6} K^{-1}	3,3
Toplotna prevodnost, W/(m K)	18

β-SiAlON-e opišemo s formulo $Si_{6-x}Al_xO_xN_{8-x}$ ($0 = x = 4,2$).[6] Keramika z nizko vrednostjo x ima dobro trdnost pri visoki temperaturi in je odporna proti lezenju in oksidaciji, keramika z visoko vrednostjo x pa ima dobre lastnosti pri nižjih temperaturah, visoko trdnost, žilavost in abrazijsko obstojnost. α-SiAlON opišemo s formulo $Me_xSi_{12-(m+n)}Al_{(m+n)}O_nN_{16-n}$.[7,8] Me označuje dodatno kovino (Me = metal, npr. Li, Mg, Ca itd.), njen delež x pa je pri znanih parametrih m in n določen z valenco kovine Me. Iz formul za oba sialona je razvidno, da je osnovna celica modifikacije α približno dvakrat večja kot za modifikacijo β, tako kot pri silicijevem nitridu.

Sialonska keramika je v zadnjem času dobila velik pomen in se uvrstila med komercialne materiale visokotehnoloških keramičnih produktov. Zaradi dobrih visokotemperaturnih mehanskih in termičnih lastnosti je v zadnjem desetletju doživela nagel razvoj in vse večje povpraševanje. Pomembna prednost te keramike je predvsem v enostavnejši pripravi in doseganju boljših mehanskih lastnosti v primerjavi s čistim Si_3N_4. V metalurgiji izrabljamo obstojnost sialonov v stiku s staljenim bakrom, aluminijem in njunimi zlitinami. V strojništvu izrabljamo njene dobre tribološke lastnosti (lastnosti pri agresivnem trenju z drugimi materiali) in odpornost proti abraziji. Iz sialonov se izdelujejo orodja za vlečenje cevi in žic, krogelni in drsni ležaji, rezalna orodja za obdelavo super zlitin in sive litine pri visokih hitrostih rezanja, hkrati pa je zaradi visoke žilavosti rezalno orodje iz sialonov možno uporabljati tudi za rezkanje.[9]

2 EKSPERIMENTALNO DELO

Na Odseku za inženirsko keramiko K6 IJS smo raziskovali pripravo materiala za prototipno keramično čepno žarilno svečko iz Si_3N_4 z dispergiranimi prevodnimi delci. Z ta namen lahko uporabimo tudi sialonsko matrico, sialoni pa so zaradi dobrih mehanskih lastnosti zanimivi tudi kot strukturni materiali.

2.1 Prototipna keramična čepna žarilna svečka

Kot zanimiv primer združitve odličnih mehanskih lastnosti Si_3N_4 in pravih električnih lastnosti dodatkov za dosego primerne funkcionalnosti omenimo izdelavo keramične čepne žarilne svečke za dizelske motorje. Ti motorji nimajo klasičnih vžignih svečk, vseeno pa ta vozila potrebujejo žarilno svečko, ki omogoča zagon in boljše delovanje hladnega motorja. V preteklosti so se v ta namen uporabljale kovinske žarilne svečke, njihovi slabosti pa sta dolg odzivni čas in omejena trajnost uporabe. Zaradi višjih ekoloških zahtev naj bi nove žarilne svečke hitreje dosegale temperaturo, potrebno za vžig goriva. Doba trajanja take svečke naj bi bila primerljiva s trajnostno dobo dizelskega motorja. Zato so različna podjetja po svetu pred okoli 20 leti začela razvijati keramično čepno žarilno svečko (KČŽS).[10] Takšna svečka naj bi izpolnjevala naslednje zahteve: temperaturo 1000 °C naj bi dosegla v manj kot dveh sekundah z začetnim tokom manjšim od 20 A, delovna temperatura svečke naj bi bila okrog 1300 °C, kar bi zagotavljala tok manjši od 8 A in napetost okrog 8 V. Silicijev nitrid (Si_3N_4) je med najprimernejšimi materiali za električno neprevodno keramično komponento, kot prevodno komponento pa najpogosteje uporabljajo volframov karbid (WC) in molibdenov disilicid ($MoSi_2$).[11] Na svetu je več tisoč patentov v zvezi z žarilno svečko in od tega več sto, ki se nanašajo na keramično žarilno svečko. Po številu prijavljenih patentov prednjačita japonski NGK in podjetje Bosch, ki je prve patente s tega področja prijavilo že pred petnajstimi leti. Tudi na IJS poskušamo sodelavci na keramiki zaradi podpore domači industriji razviti prototip keramične svečke na osnovi silicijevega nitrida in molibdenovega disilicida.

Si_3N_4/$MoSi_2$-kompoziti so bili pripravljeni iz naslednjih kupljenih prahov: Si_3N_4, $MoSi_2$, Al_2O_3 in Y_2O_3. **Tabela 2** prikazuje njihove masne deleže. Dodatka Y_2O_3 in Al_2O_3 izboljšata sintranje Si_3N_4 zaradi nastanka prehodne tekoče faze med sintranjem.

Pravilna izbira vrste in količine oksidnih dodatkov ter pogojev sintranja, to je temperature, tlaka in atmosfere, močno vpliva na končno mikrostrukturo, lastnosti in

obstojnost produkta. Čeprav ima keramični prah Si_3N_4 strukturo α, prevladuje po sintranju β-Si_3N_4, ki ima ustreznejše lastnosti kot modifikacija α (posebno bistveno drugačno toplotno prevodnost). V **tabeli 3** sta navedena upogibna trdnost in električna prevodnost kompozitov.

Tabela 2: Sestava kompozita $Si_3N_4/MoSi_2$, izdelanega na IJS: masni deleži sestavin so podani v odstotkih
Table 2: Chemical composition of $Si_3N_4/MoSi_2$ composite, fabricated at the JSI: weight portions are given in percentages

Oznaka	Si_3N_4	$MoSi_2$	Y_2O_3	Al_2O_3
1	61,2	32,0	3,9	2,9
2	49,9	44,6	3,1	2,4
3	44,7	50,3	2,8	2,2

Tabela 3: Primerjava upogibne trdnosti σ_{up} in električne prevodnosti σ_{el} sintranih kompozitov glede na vsebnost $MoSi_2$
Table 3: Comparison of the bend strength σ_b and electrical conductivity σ_{el} of sintered composites in dependence on a portion of $MoSi_2$

Oznaka	σ_{up}/MPa	σ_{el}/(S/m)
1	480	$8{,}5 \times 10^{-9}$
2	350	7,15
3	270	306

Po pričakovanju je specifična električna prevodnost vzorcev močno odvisna od količine prevodne komponente $MoSi_2$, saj je sam Si_3N_4 električni izolator. Sestave nekako med tistima z oznakama 2 in 3 imajo primerno električno prevodnost, ki naj bi se pri keramičnih grelcih in čepnih svečkah gibala v območju 1–100 S/m. Vendar pa upogibna trdnost materiala hitro pada z vsebnostjo $MoSi_2$, svečke pa morajo imeti zelo visoko trdnost, da vzdržijo termični šok med delovanjem. Vrednosti trdnosti, podane v tabeli 3, so prenizke. Zato je treba iskati rešitve, npr. spreminjati še druge parametre poleg deleža $MoSi_2$. Ena od možnosti bi bila naslednja. Podatki za izmerjeno električno prevodnost v **tabeli 3** so za določeno povprečno velikost delcev $MoSi_2$ v prahu ($\approx$2 μm). Z manjšo velikostjo delcev $MoSi_2$, ki bi jo dosegli s temeljitim mletjem, se da pri enakih masnih deležih $MoSi_2$ povečati prevodnost, ne da bi s tem poslabšali upogibno trdnost kompozita. Kljub omenjenim težavam nam je na Odseku za inženirsko keramiko uspelo izdelati prototipno čepno svečko (**slika 5**).

Slika 5: Delovanje prototipne keramične žarilne svečke, izdelane na našem odseku
Figure 5: Functioning of the prototype ceramic glow plug fabricated in our department

Bralec lahko najde nekaj informacij o komercialnih čepnih svečkah, izdelanih v svetu, na spletnih straneh.[12]

2.2 Priprava SiAlON-ov

Priprava sialonske keramike je v primerjavi s silicijevim nitridom v splošnem enostavnejša zaradi raznovrstne mešanice prahov, kot so Si_3N_4, AlN, Al_2O_3 in Y_2O_3, ki olajšajo sintranje. Le-to je omejeno s temperaturo kemijskega razpada silicijevega nitrida, 1900 °C. Na IJS smo izdelali sialonsko keramiko s sintranjem pri temperaturi 1800 °C za 2 uri v pretoku dušika in pri navadnem tlaku, in sicer v zasipu iz mešanice prahov Si_3N_4 in BN v masnem razmerju 1 : 1. Glede na doseženo gostoto (97 % teoretične gostote) in nastalo mikrostrukturo se je najbolje zgostila tista sialonska keramika, pri kateri smo dosegli zadovoljive vrednosti upogibne trdnosti (750 MPa).

Zanimiva možnost je tudi priprava mnogoplastnih kompozitov, kjer imajo posamezne plasti različne deleže α- in β-sialona. Z ulivanjem α- in β-suspenzij sialona (prostorninski delež suhe snovi 40 %) v mavčne modele smo pripravili valjaste in ravne kompozite. Ulite vzorce smo nato sintrali pri 1800 °C 2 h v dušikovi atmosferi. Tako smo pripravili relativno goste mnogoplastne kompozite. Za dosego njihovih ustreznih mehanskih lastnosti je treba upoštevati več faktorjev, na primer reološke lastnosti suspenzij prahov, optimalne parametre sintranja, različne temperaturne razteznostne koeficiente posameznih plasti v odvisnosti od njihove sestave itd. Na primer, zaradi različnega temperaturnega raztezanja posameznih plasti pri ohlajanju do sobne temperature po sintranju lahko pride do velikih termičnih preostalih napetosti v materialu, ki povzročijo nastanek razpok in celo razplastitev. Podobna težava se lahko pojavi tudi pri sušenju suspenzij v kalupu zaradi različnih hitrosti sušenja posameznih plasti. Ravne mnogoplastne kompozite smo ulivali v pravokoten model plast za plastjo, pri čemer smo pred ulivanjem nove plasti nekoliko počakali, da se je vrhnja plast delno posušila. Izmerili smo upogibne trdnosti teh kompozitov, ki jih želimo optimizirati.

3 RAZPRAVA

Izkazalo se je, da se pri sintranju tako Si_3N_4 kot sialon zgostita do relativno visoke gostote. Pomembni sta predvsem vrsta in količina dodatkov za sintranje, pa tudi tehnika sintranja. Sialonska keramika se v primerjavi s Si_3N_4 pri sicer enakih pogojih sintranja bolj zgosti zaradi dodanega AlN (npr. 2,2 %).

Pri delčnih kompozitih na osnovi Si_3N_4 z dispergiranimi prevodnimi delci so mehanske in električne lastnosti odvisne od dodanega deleža prevodne komponente, predvsem od tega, ali ta delež preseže perkolacijski prag prevodnosti. V splošnem velja, da z večjim deležem prevodne komponente povečamo električno prevodnost končnega materiala, vendar pa s tem poslabšamo mehanske lastnosti, zato moramo najti kompromis med temi lastnostmi. Pregled znanstvenih publikacij s področja električno prevodnih keramičnih kompozitov na osnovi silicijevega nitrida je pokazal, da lahko ustrezno električno prevodnost materiala dosežemo z majhnim dodatkom prevodne komponente v začetno mešanico prahu, vendar pa morajo ti delci tvoriti električno prevodno mrežo okrog večjih zrn Si_3N_4[13]. Izdelava takšnih kompozitov zahteva uporabo granularnega prahu Si_3N_4, ki mora biti oblečen s prevodnimi nanodelci, in uporabo druge tehnike sintranja, ki dopušča sintranje pri nižjih temperaturah ob povišanem tlaku. Takšna izbira oz. priprava izhodnih surovin in tehnike sintranja omogoča, da je material električno prevoden že pri volumenskem deležu prevodne faze 5 %. S tem dosežemo ustrezne električne in mehanske lastnosti za izdelavo keramičnega grelca ali keramične čepne žarilne svečke za dizelske motorje.[14,15]

Iz raziskav mnogoplastnih sialonskih kompozitov je razvidno, da lahko z upoštevanjem ključnih parametrov pri pripravi suspenzij in optimizaciji pogojev sintranja dosežemo goste kompozite z dobrimi mehanskimi lastnostmi. V literaturi najdemo veliko eksperimentalnih in teoretičnih raziskav tudi na drugih mnogoplastnih kompozitih, npr. iz Al_2O_3 in ZrO_2. Bile so usmerjene tako v primerne metode za njihovo izdelavo kot v optimizacijo efektivne upogibne trdnosti in lomne žilavosti.[16–22] Optimizacijo upogibne trdnosti je mogoče doseči s sestavo, razporeditvijo in debelino posameznih plasti. Te raziskave so lahko vodilo tudi za optimizacijo mnogoplastnih sialonov. V prihodnosti utegnejo kompozitom na osnovi sialonske keramike zaradi dobrih mehanskih in fizikalnih lastnost nameniti večjo pozornost na področju inženirske keramike.

4 SKLEP

Na področju kompozitne keramike Si_3N_4 smo se ukvarjali predvsem s prevodno keramiko z dispergiranimi $MoSi_2$-delci in s sialoni. Obe vrsti materiala je treba še optimizirati: 1) pri keramiki $Si_3N_4/MoSi_2$ moramo izboljšati prevodnost, ne da bi bistveno poslabšali mehanske lastnosti; 2) pri mnogoplastnih kompozitih na osnovi α- in β-sialonov moramo odpraviti nekatere težave, kot je razplastitev. Dosedanje raziskave pa so spodbudne.

5 LITERATURA

[1] P. F. Becher, M. J. Hoffmann, Influence of additives on anisotropic grain growth in silicon nitride ceramics, Material Science and Engineering, A422 (**2006**), 85–91

[2] Spletni naslov: http://en.wikipedia.org/wiki/silicon_nitride

[3] Frank L. Riley, Silicon nitride and related materials, Journal of the American Ceramic Society, 83 (**2000**) 2, 245–65

[4] Calis N., Kara F., Mandal H., Functionally graded SiAlON ceramics, Journal of the European Ceramic Society, 24 (**2004**), 3387–3393

[5] Ekstrom T., Nygren A, SiAlON Ceramics, Journal of American Ceramic Society, 75 (**1992**) 2, 259–276

[6] L. K. L. Falk, Imaging and microanalysis of liquid phase sintered silicon-based ceramic microstructures, Journal of Materials Science, 39 (**2004**), 6655–6673

[7] Pernilla Pettersson, Zhijian Shen, Mats Johnsson, Thermal shock properties of β-sialon ceramics, Journal of the European Ceramic Society, 22 (**2002**), 1357–1365

[8] Izhevskiy V. A., Genova L. A., Aldinger F., Progress in SiAlON ceramics, Journal of the European Ceramic Society, 20 (**2000**), 2275-2295

[9] Erhan Ayas, Alpagut Kara, Hasan Mandal, Production of α-β SiAlON-TiN/TiCN composites by gas pressure sintering, Sil. Ind. Special Issue, 69, Turkey, 2005

[10] H Kawamura, Thermos construction made of Si_3N_4 in the heat isulated engine, Key engineering materials, 89 (**1994**), 713–718

[11] K. Yamada, N. Kamiya, High temperature mechanical properties of Si_3N_4-$MoSi_2$ and Si_3N_4-SiC composites with network structures of second phases, Mat. Sci. Eng. A-Struct. Mat., Properties, microstructure and Processing, 261 (**1999**), 270–277

[12] Spletni naslov: http://www.le-mark.cn/E-pages/product/glow%20plug.asp

[13] E. Ayas, A. Kara, F. Kara, A novel approach for preparing electrically conductive α/β SiAlON-TiN composites by spark plasma sintering, J. Ceram. Soc. Jap., 116 (**2008**) 7, 812–814

[14] S. Kawano, J. Takahashi, S. Shimada, Highly electroconductive TiN/Si_3N_4 composite ceramics fabricated by spark plasma sintering of Si_3N_4 particles with a nano-sized TiN coating, J. Mater. Chem., 12 (**2002**), 361–365

[15] L. Gao, J. Li, T. Kusunose, K. Niihara, Preparation and properties of TiN-Si_3N_4 composites, J. Eu. Ceram. Soc., 24 (**2004**), 381–386

[16] J. Requena, R. Moreno, J. S. Moya, Alumina and alumina/ zirconia multilayer composites obtained by slip casting, J. Am. Ceram. Soc., 72 (**1989**) 8, 1511–13

[17] P. Sarkar, X. Huang, P. S. Nicholson, Structural ceramic microlaminates by electrophoretic deposition, J. Am. Ceram. Soc., 75 (**1992**) 12, 2907–09

[18] C. J. Russo, M. P. Harmer, H. M. Chan, G. A. Miller, Design of a laminated ceramic composite for improved strength and toughness, J. Am. Ceram. Soc., 75 (**1992**) 12, 3396–400

[19] D. D. Barnett-Ritcey, P. S. Nicholson, Failure prediction maps for a model Al_2O_3 | c-ZrO_2/Al_2O_3 | Al_2O_3 brittle polycrystalline trilayer composite, J. Am. Ceram. Soc., 86 (**2003**) 1, 121–28

[20] C.-H. Hsueh, Modeling of elastic deformation of multilayers due to residual stresses and external bending, J. Appl. Phys., 91 (**2002**) 12, 9652–56

[21] Ambrožič M., Kosmač T., Optimization of the bend strength of flat-layered alumina-zirconia composites, J. Amer. Ceram. Soc. 90 (**2007**) 5, 1545–1550

[22] Beranič Klopčič S., Ambrožič M., Kosmač T., Novak S., Tunneling cracks in Al_2O_3/Al_2O_3-ZrO_2 layered composites, J. Eur. Ceram. Soc. 27 (**2007**), 1333–1337

UDK 669.15:669.14.018.298
Professional article/Strokovni članek

ISSN 1580-2949
MTAEC9, 43(3)171(2009)

INVESTIGATIONS OF MICRO-ALLOYED CAST STEELS

RAZISKAVE MIKROLEGIRANIH JEKLENIH LITIN

Bommannan Chokkalingam, S. S. Mohamed Nazirudeen

Department of Metallurgical Engineering, PSG College of Technology, Peelamedu, Coimbatore-641 004. India
bchokkalingam@gmail.com

Prejem rokopisa – received: 2008-11-06; sprejem za objavo – accepted for publication: 2009-03-23

This paper presents a review of the effect of micro-alloying with vanadium, niobium, titanium and zirconium in carbon and low-alloy cast steels of different compositions. The elements were added in different percentages and combinations to the base cast steels. Also, the effect of heat treatment on the experimental steels is presented. The micro-alloying improved the mechanical properties of the as-cast and heat-treated base steels significantly.

Key words: cast steel, chemical composition, micro-alloying, mechanical properties, heat treatment

Predstavljeni so rezultati raziskav o vplivu mikrolegiranja z vanadijem, niobijem, titanom in cirkonijem na mehanske lastnosti in trdoto ogljikove in malolegirane jeklene litine z različno sestavo. Mikrolegirni elementi so bili dodani osnovnemu jeklu individualno in v različnih kombinacijah. Mikrolegiranje je močno vplivalo na lastnosti tega jekla v litem stanju in po toplotni obdelavi.

Ključne besede: jeklene litine, kemična sestava, mikrolegiranje, toplotna obdelava, mehanske lastnosti

1 INTRODUCTION

Micro-alloyed steels are low, medium carbon steels or low-alloy steels with the addition of elements such as niobium, titanium, vanadium and zirconium. These additions increase the strength of the steel, individually, and also in different combinations. Initially, micro-alloyed wrought steels were produced with micro-alloying and with thermo-mechanical processing (heat treatment) for higher strength as well as toughness and good weldability. Similar improvements are required for steels in the as-cast condition, especially carbon and low-alloy steels that are used for many applications. Moreover, these castings are frequently used in extreme conditions of tensile and fatigue stressing, impact loading, creep, abrasion and corrosion. Generally, cast steels have the major advantage of wider ranges of composition, higher casting temperatures and fewer impurities over wrought steels. To meet the present critical applications of components, cast steels with higher strengths and toughnesses are used. In this paper, the effect of the micro-alloying elements on the properties of the cast steels is investigated.

2 TYPES OF ALLOY STEELS

Steels containing one or more alloying elements, other than carbon, are designed to enhance one or more of the steels' properties. Specifically, alloy steels are superior to plain carbon steels due to the effect of the alloying elements. All alloy steels can be classed into three groups with respect to the total content of alloying elements: low-alloy steels[1,2] with up to 5 %, medium-alloy steels[1] with 5 % to 10 % and high-alloy steels with more than 10 %.

In micro-alloy steel, minor amounts of vanadium, niobium and/or titanium, etc., are added[2,3]. The addition of these individual elements is generally less than 0.10 % and the total micro-alloying is less than 0.20 %.

3 BASE STEEL AND MICRO-ALLOYING

The chemical compositions of the base steels used for the micro-alloying experiments are presented in **Table 1**. The micro-alloying was achieved with the addition of vanadium, niobium, titanium and zirconium to the base steels. The contents of the micro-alloying elements are given in **Table 2**.

4 MECHANICAL PROPERTIES

The maximum yield and the ultimate tensile strengths[3–7] of the experimental steels, the base (UMA) and the micro-alloyed (MA), are shown in **Figure 1** and **Figure 2**. After micro-alloying (MA), the yield and tensile strengths[3] were increased by 110 % and 100 %, respectively, when compared to the un-micro-alloyed steels. The experimental steels[3] were quenched and tempered at various temperatures. A low carbon content was maintained in all the experimental steels to achieve sufficient ductility. The minimum yield strength and the ultimate tensile strength were obtained for 0.003 V and 0.001 Ti after tempering at 700 °C. In this steel the highest yield strength and the ultimate tensile strength were obtained with combined tempering at temperatures of 700 °C and 400 °C.

Table 1: Summary of chemical compositions of the base cast steels
Tabela 1: Pregled kemične sestave osnovnih in mikrolegiranih jekel

Ref No.	Experimental Steel	Elements in wt %								
		C	Si	Mn	P	S	Cr	Mo	Ni	Al
3	Steel 1 (UMA)	0.23	0.36	0.88	0.04	0.04	0.39	0.10	–	0.004
	Steel 1 (MA)	0.23	0.36	0.88	0.04	0.04	0.39	0.10	–	0.004
	Steel 2 (MA)	0.18	0.30	0.85	0.03	0.03	0.40	0.10	–	0.012
	Steel 3 (MA)	0.16	0.32	0.83	0.02	0.03	0.40	0.10	–	0.015
	Steel 4 (MA)	0.15	0.34	0.82	0.04	0.03	0.40	0.10	–	0.056
4	Steel 5 (UMA)	0.21	0.39	1.13	–	–	0.11	0.18	0.91	0.035
	Steel 5 (MA)	0.21	0.39	1.13	–	–	0.11	0.18	0.91	0.035
	Steel 6(MA)	0.20	0.52	1.24	–	–	0.41	0.29	0.76	0.007
5,6	Steel 7(UMA)	0.14	0.35	1.56	0.010	0.015	–	–	–	0.03
	Steel 8(MA)	0.15	0.31	1.41	0.010	0.015	–	–	–	0.02
	Steel 9(UMA)	0.14	0.30	1.54	0.009	0.02	–	–	–	0.03
	Steel 9(MA)	0.14	0.30	1.54	0.009	0.02	–	–	–	0.03
	Steel 10(MA)	0.14	0.32	1.55	0.009	0.016	–	–	–	0.02
7	Steel 11(UMA)	0.06	0.14	1.60	0.03	0.07	–	–	–	0.05
	Steel 12(MA)	0.06	0.14	1.80	0.03	0.08	–	–	–	0.05
	Steel 13(UMA)	0.06	0.09	1.85	0.01	0.10	–	–	–	0.01
	Steel 13(MA)	0.06	0.09	1.85	0.01	0.10	–	–	–	0.01
	Steel 14(MA)	0.07	0.09	1.85	0.03	0.07	–	–	–	0.04
	Steel 15(MA)	0.07	0.09	1.90	0.01	0.09	–	–	–	0.03

Table 2: Summary of the micro-alloying elements
Tabela 2: Pregled vsebnosti mikrolegiranih elementov

Reference	Experimental Steel	Elements in wt %			
		Vanadium	Niobium	Titanium	Zirconium
Ref. 3	Steel 1(UMA)	–	–	–	–
	Steel 1 (MA)	0.003	–	0.001	–
	Steel 2(MA)	0.11	–	0.01	–
	Steel 3(MA)	0.11	0.036	0.01	–
	Steel 4(MA)	0.11	0.036	0.04	–
Ref. 4	Steel 5 (UMA)	–	–	–	–
	Steel 5(MA)	0.09	–	–	–
	Steel 6(MA)	0.09	0.035	–	–
Ref. 5, 6	Steel 7(UMA)	–	–	–	–
	Steel 8(MA)	0.096	–	–	–
	Steel 9(UMA)	–	–	–	–
	Steel 9(MA)	0.092	0.047	–	–
	Steel 10(MA)	0.10	0.043	0.023	–
Ref. 7	Steel 11(UMA)	–	–	–	–
	Steel 12(MA)	–	–	–	0.005
	Steel 13(UMA)	–	–	–	–
	Steel 13(MA)	–	–	–	0.01
	Steel 14(MA)	–	–	–	0.02
	Steel 15(MA)	–	–	–	0.10

The mechanical properties for the micro-alloyed steel 5 and the corresponding base steel were tested after normalizing (920 °C), quenching (920 °C) and tempering (580 °C) as well as homogenization (1100 °C) treatments[4]. Due to the micro-alloying, the yield strength was increased by 118 % and the tensile strength by 65 %, respectively, when compared to the un-micro-alloyed steels. The minimum and maximum yield and tensile strengths[5] were obtained in steel 5 with the addition of 0.09 vanadium after the normalizing and homogenizing treatments.

The mechanical properties[5,6] were tested in the as-cast condition without any heat treatment. After the micro-alloying the yield and tensile strengths were increased by 55 % and 26 % with respect to the un-micro-alloyed steels. The minimum yield and the tensile strengths were obtained in the un-micro-alloyed steel 9 without any heat treatment. The addition of

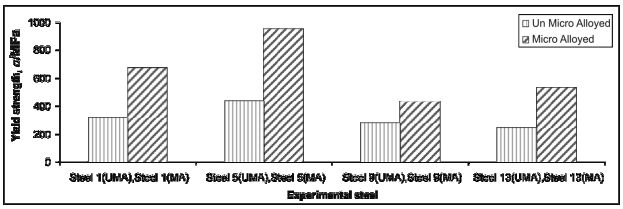

Figure 1: Yield strength
Slika 1: Meja plastičnosti

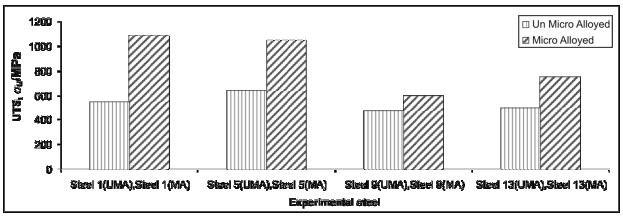

Figure 2: Ultimate tensile strength
Slika 2: Raztržna trdnost

vanadium individually increased both the yield strength and ultimate tensile strength up to 100 MPa. After micro-alloying, the steel 9, with 0.092 vanadium and 0.047 niobium, had its yield strength and ultimate tensile strength increased by 160 MPa and by 125 MPa.

Zirconium was also added as a micro-alloying element to the low-carbon base steel[7]. Four trials were made by varying the content of zirconium in the base steel and the mechanical properties were tested after quenching, tempering and homogenizing. After the addition of zirconium, the yield and tensile strengths were increased by 120 % and 50 % with respect to the un-micro-alloyed steel. The minimum values for the yield and tensile strengths were found for the micro-alloyed steel 13 after homogenization. The tempering treatment improved both the ultimate tensile strength and the yield strength in steel 13 with 0.01 zirconium more than the quenching and the homogenizing.

The elongation and reduction of area obtained for the experimental steels un-micro-alloyed and micro-alloyed are shown in **Figure 3** and **Figure 4**, respectively[3,4,7]. The elongation and the reduction of the area after micro-alloying[3] for the steel 11 are lower by 27 % and 28 %, respectively.

The minimum and maximum elongation and reduction of area[3] were found for the steel 1 after tempering at 400 °C and 700 °C, respectively.

For the steel 5, after micro-alloying the elongation and the reduction of area were decreased by 44 % and 45 %, respectively. The minimum elongation and reduction of area for the steel 5 were found after homogenization and normalization and the benefit of micro-alloying was achieved in steel 5 only after quenching and tempering at 580 °C.

After micro-alloying[5,6] in steel 9, the elongation was decreased by 36 %. The minimum elongation was found for the micro-alloyed steel 9 and maximum for the un-micro-alloyed steel 9.

The elongation and the reduction of area due to micro-alloying[7] in steel 13 were decreased by 40 % and 70 %, respectively, with respect to the un-micro-alloyed steel 11. The minimum elongation and reduction of area were found after quenching and the maximum after tempering at 450 °C.

The hardness[3,5,6,7] of the experimental steels is shown in **Figure 5**. After micro-alloying, the hardness was increased by 146 % in steel 1, 27 % in steel 9 and 130 % in steel 13, respectively.

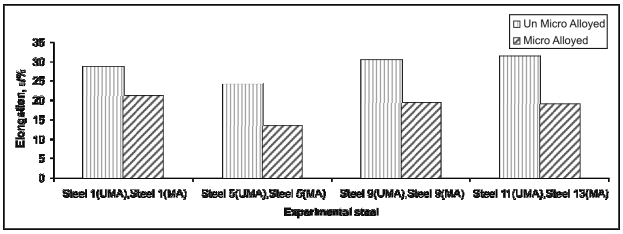

Figure 3: Percentage elongation
Slika 3: Raztezek v odstotkih

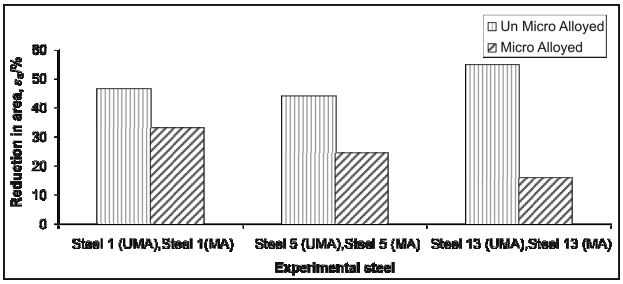

Figure 4: Percentage reduction in area
Slika 4: Skrček v odstotkih

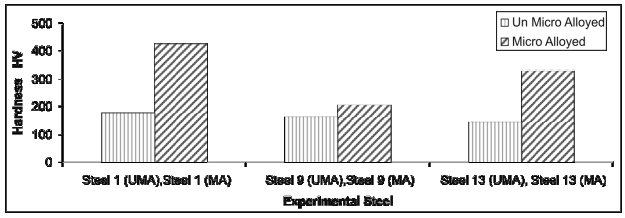

Figure 5: Hardness
Slika 5: Trdota

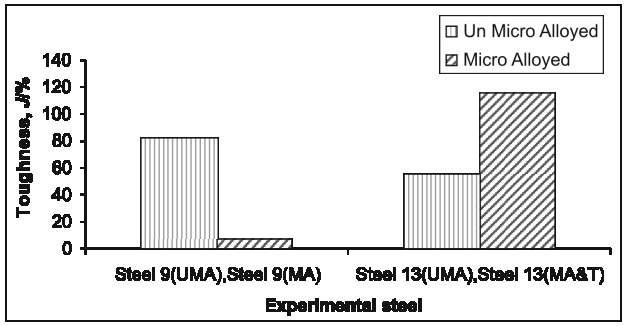

Figure 6: Impact toughness
Slika 6: Udarna žilavost

The minimum and maximum hardness[3] were obtained in steel 1 with 0.003 V and 0.001 Ti after hardening and tempering at 500 °C. The minimum hardness was found for the un-micro-alloyed steel 9 and the maximum for the micro-alloyed steel 9 without heat treatment[5,6]. The maximum hardness[7] was found for the micro-alloyed quenched steel 13 with 0.005 of zirconium and the minimum for the un-micro-alloyed steel 13.

Generally, the hardness was higher after quenching and tempering treatments than in the as-cast condition.

The toughness[5,6,7] obtained with the micro-alloyed and the un-micro-alloyed for the experimental steel 9 and steel 13 is shown in **Figure 6.** The toughness[5,6,7] due to micro alloying[7] was decreased by 90% in the micro-alloyed steel 9 without heat treatment and increased by 110% in the micro-alloyed tempered steel 13 with 0.01 zirconium.

5 MICRO-ALLOYING MECHANISMS

A fine grain size[3] was achieved in micro-alloyed steel 1 compared with that of the un-micro-alloyed steel 1. Generally, grain refinement was found in all the micro-alloyed steels. In micro-alloyed steels the titanium precipitates as TiN and the vanadium as VC/V(CN). Nb precipitates from the matrix as NbC/Nb (CN) independently, or on the existing TiN particles. The grain refinement and precipitation hardening induce the higher strength and hardness of the micro-alloyed steels.

In steel 5, micro-alloyed with vanadium,[4] the strengthening is achieved with a fine precipitation of VC in the ferrite matrix and also with the fine interlamellar spacing of pearlite. The vanadium addition in the as-cast condition affects the grain size of the ferrite also.

The increase in yield and ultimate tensile strengths and hardness[5,6] in the micro-alloyed steel 9 is due to the formation of a fine scale of carbonitride precipitates. The micro-alloy carbonitrides precipitate on the advancing alpha/gamma interface. The micro-alloying of the niobium precipitates in the matrix or at the austenite grain boundaries, whereas the vanadium precipitates as V(C,N) as an interphase or random precipitation.

Zirconium is a strong nitride-[7] and oxide-forming element. In the zirconium micro-alloyed steels the ZrC precipitates form at higher temperatures and the ZrN precipitates at lower temperatures. The precipitation of ZrN and the heat treatment improves the mechanical properties of the micro-alloyed steel 13 very much with respect to the addition of zirconium.

6 CONCLUSION

I In this article the effects of micro-alloying additions of vanadium, niobium, titanium and zirconium in low-carbon base steels of different compositions, as cast and after heat treatment are presented and discussed.

The chemical composition of the base steel used and the individual and combined additions of micro-alloying elements used for the experimental work are given.

The minimum and maximum values of the mechanical properties obtained in the micro-alloyed cast steels in the quoted references are summarized and discussed.

II Generally, the ultimate tensile strength, yield strength and hardness are greater with micro-alloyed cast steels, while the ductility, measured as elongation and the reduction of area, is smaller. Also, the notch toughness is lower after micro-alloying.

III In steels micro-alloyed with vanadium, niobium and titanium, the tensile strength was lower in the presence of titanium. The vanadium addition individually increased the yield strength and the tensile strength up to 100 MPa, whereas vanadium and niobium additions increased the yield strength and ultimate tensile strength by 128 MPa and 90 MPa, respectively.

IV The hardness was higher after micro-alloying the zirconium, especially after tempering. An increased hardness and toughness were obtained with 0.005–0.01 % of zirconium.

7 REFERENCES

[1] T. V. Rajan, C. P. Sharma, Ashok Sharma , Heat treatment principles and techniques, 1st ed., Prentice Hall of India private limited, New delhi (**2006**), ISBN-81-203-0716-X, 53

[2] V. Raghavan, Physical metallurgy principles and practice, 2nd ed., Prentice Hall of India private limited, New delhi 2006, 106, 193, ISBN-81-203-3012-9

[3] B. D. Jana, A. K. Chakrabarti., K. K. Ray, Study of cast micro-alloyed steels, Materials science and technology, (**1993**), January, 80–86

[4] Barbara Kalandyk, Hubert Matysiak, Jan Glownia, Microstructure strength relationship in microalloyed cast steels, Reviews on advanced material science, 1 (**2004**) 8, 44–48

[5] H. Najafi, J. Rassizadehghani, A. Halvaaee, Mechanical properties of as cast microalloyed steels containing V, Nb and Ti, Material science and technology, 23 (**2007**) 6, 699–705

[6] J. Rassizadehghani, H. Najafi, M. Emamy, Eslami Saeen, Mechanical properties of V, Nb and Ti bearing as cast micro alloyed steels, Journal of material science and technology, 23 (**2007**) 6, 779–784

[7] H. A. Akbarzadeh, M. Tamizifar, Mirdamadi Sh, A. Abdolhossini, Mechanical properties and micro structures of Zr – microalloyed cast steel, ISIJ international, 45 (**2005**), 1201–1204